Spring 2015

Transient Cardiovascular Hemodynamics In A Patient-Specific Arterial System

Jr Rodward Hewlin
North Carolina Agricultural and Technical State University

Transient Cardiovascular Hemodynamics in a Patient-Specific Arterial System

Rodward Lorenzo Hewlin, Jr

North Carolina A&T State University

A dissertation submitted to the graduate faculty

in partial fulfillment of the requirements for the degree of

DOCTOR OF PHILOSOPHY

Department: Mechanical Engineering

Major: Mechanical Engineering

Major Professor: Dr. John P. Kizito

Greensboro, North Carolina

2015

The Graduate School
North Carolina Agricultural and Technical State University

This is to certify that the Doctoral Dissertation of

Rodward Lorenzo Hewlin, Jr.

has met the dissertation requirements of
North Carolina Agricultural and Technical State University

Greensboro, North Carolina
2015

Approved by:

Dr. John P. Kizito Major Professor	Dr. Mannur Sunderesan Committee Member
Dr. Gary Tatterson Committee Member	Dr. Cynthia K. Waters Committee Member
Dr. Samuel Owusu-Ofori Department Chair	Dr. Roy Coomans Committee Member

Dr. Sanjiv Sarin
Dean, The Graduate School

Biographical Sketch

Rodward Lorenzo Hewlin, Jr. was born in Rocky Mount, North Carolina on July 17, 1986. He is the son of Arnetta L. Hewlin and Rodward Lorenzo Hewlin, Sr., former CEO and owner of Hewlin Bros. Lumber Co., formerly known as Joseph & Sons Hewlin Lumber Co. est. 1879. Rodward Lorenzo Hewlin, Jr. has served greatly in K-12 Education and Secondary Education. Rodward has served in Guildford County Public School systems as a part of the Bush Administration's Law "No Child left behind" Title I. K-6 tutor for L&U Contractors. Rodward has also taught undergraduate senior and junior level laboratory courses as part of the Mechanical Engineering curriculum at North Carolina Agricultural & Technical State University College of Engineering's Mechanical Engineering Program from 2008 to 2010.

As an undergraduate, Rodward Lorenzo Hewlin, Jr. enjoyed academic research. Rodward was an accomplice in the *Duke University's Summer Research Experience for Undergraduates (REU)* in the summer of 2006, where he studied magnetic nanoparticles using a magnetophoresis-based method to obtain particle magnetic susceptibility. Rodward has also served in Government an accomplice for *Quality Education for Minorities* (*QEM) Network* and *National Science Foundation (NSF) Directorate of Engineering and Division of Chemical Biochemical Environmental and Transport* (CBET) for reviewing grants and proposals and evaluating program performance. Rodward graduated with honors from North Carolina A&T State University with a Bachelors of Science and Masters of Science degree in Mechanical Engineering.

Dedication

I dedicate this dissertation to my loving family. To my loving wife Chase Hewlin, without your love and support none of this would be possible. To my parents, whose patience, nurturing and regard for education held me on a steady course throughout my academic studies, I love you dearly. To my sister Brittany Michelle Hewlin, I am very proud of you and wish you nothing but success. To my brother Cedric Alexander Hewlin, who taught me that life is very precious and that we should enjoy each fulfilling moment. Your presence in my life has taught me so many things: how to be patient, kind and thankful. You are a very intelligent individual who I commend for your hard work and efforts. Finally, to my grandfather, I miss you dearly. When I think of my grandfather, I think of what Shakespeare said in Romeo and Juliet: *"And when he shall die, take him and cut him into little stars, and he shall make the face of heaven look so fine, and may all the world be in love with night, and pay no worship to the garish sun."*

Acknowledgments

I would like to thank the following people for their assistance throughout my academic study. First, I would like to express thanks to my advisor Dr. John P. Kizito for all of his hard work and dedication to obtaining the laboratory space and funding for the present study, and for also providing me the opportunity to further my career and study, and for sharing comedic analogies of relating scientific theories to everyday life situations which not only lifted my spirits, but provided a unique and different outlook on life in a scientific way. I would like to thank him for all his guidance, help and insight which strongly contributed to the completion of this work. I would like to express thanks to Mr. Bruce Howe and his shop staff for all of their help in machining parts for my measuring instruments, test apparatus. The efforts and advice of my committee members: Dr. Cindy Waters, Dr. Gary Tatterson and Dr. Mannur Sundaresan whose advice and support does not go unrecognized. I would also like to thank my former advisor of undergraduate research and friend at Duke University Dr. Benjamin Yellen, for not only motivating me to pursue a graduate degree, but for helping me leave my mark in the knowledge database of Biomedical Engineering. This project was funded by Title III HGBI .

Table of Contents

List of Figures

List of Tables

Abstract

The ultimate goal of the present study is to aid in the development of tools to assist in the treatment of cardiovascular disease. Gaining an understanding of hemodynamic parameters for medical implants allow clinicians to have some patient-specific proposals for intervention planning. In the present study a full cardiovascular experimental phantom and digital phantom (CFD model) was fabricated to study: (1) the effects of local hemodynamics on global hemodynamics, (2) the effects of transition from bed-rest to upright position, and (3) transport of dye (drug delivery) in the arterial system. Computational three dimensional (3-D) models (designs A, B, and C) stents were also developed to study the effects of stent design on hemodynamic flow and the effects of drug deposition into the arterial wall. The experimental phantom used in the present study is the first system reported in literature to be used for hemodynamic assessment in static and orthostatic posture changes. Both the digital and experimental phantom proved to provide different magnitudes of wall shear and normal stresses in sections where previous studies have only analyzed single arteries.

The dye mass concentration study for the digital and experimental cardiovascular phantom proved to be useful as a surrogate for medical drug dispersion. The dye mass concentration provided information such as transition time and drug trajectory paths. For the stent design CFD studies, hemodynamic results (wall shear stress (WSS), normal stress, and vorticity) were assessed to determine if simplified stented geometries can be used as a surrogate for patient-specific geometries and the role of stent design on flow. Substantial differences in hemodynamic parameters were found to exist which confirms the need for patient-specific modeling. For drug eluting stent studies, the total deposition time for the drug into the arterial wall was approximately 3.5 months.

CHAPTER 1

Introduction

Cardiovascular disease (CVD) remains to be the prominent cause of morbidity and mortality across the world and improved methods for cardiovascular disease management are deeply needed (Ricotta, Pagan et al. 2008). In the year 2000, cardiovascular disease accounted for 39% of all deaths in America, and 32.4% in 2006, producing a health care cost of $430 billion per year (Daviglus 2005, Kung 2005, Murray 2006, Rosamond, Flegal et al. 2007). The most common form of cardiovascular disease is coronary heart disease (CHD), also referred to as atherosclerosis. Atherosclerosis is a disorder in which fatty deposits develop in an artery, obstruct the lumen, and cause deformation and deterioration of the arterial wall. Critical conditions arise when atherosclerosis occurs in the coronary arteries and threatens to reduce blood flow to the myocardium. The reduction of blood flow to the heart forces the heart to produce more work and undergo stress, which eventually leads to heart failure. The result of reduced blood flow and stress to the heart is angina pectoris (chest pain) or myocardial infarction (heart attack). Also, the reduction of oxygen-rich blood to the brain results in brain cell death (stroke).

The carotid bifurcation, where the common carotid artery (CCA) branches into the internal carotid artery (ICA) and external carotid artery (ECA) is a common site of atherosclerotic disease (Hewlin and Kizito 2011). Stenosis or narrowing of the ICA has long been known to be related to the incidence of ischemic stroke (Barnette et al. 200; Fisher 1951). In severe atherosclerosis, plaque buildup significantly reduces the internal dimensions of the artery (vessel lumen), restricting blood flow as shown in Figure 1.1. Plaque is heterogeneous in

nature, and is composed of fats, proteins, and regions of calcification separated by a thin layer called the "fibrous cap". The streaked appearance of the histology clearly highlights the heterogeneity of the plaque. This extreme heterogeneity coupled with the highly irregular shape of the lumen makes it difficult to predict the mechanical behavior of the plaque as a response to WSS and normal stresses (NS). In healthy arteries, there is evidence to suggest that the arterial system remodels to maintain wall shear stress (WSS) within a narrow range of 1-2 Pa.

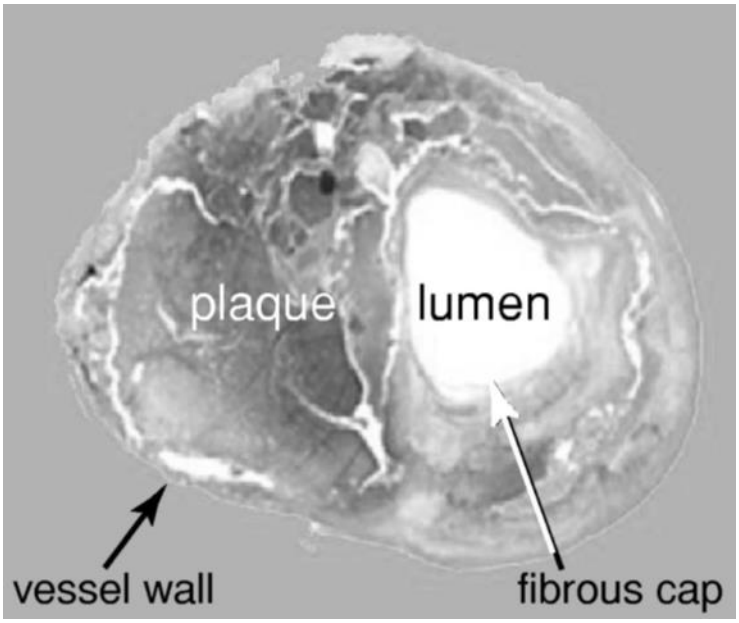

Figure 1.1. Cross-section through an atherosclerotic carotid artery. Obtained from (Bale-Glickman, Selby et al. 2003)**.**

Consequently, the use of modeling stenosis severity or degree of constriction has evolved as a surrogate to measure the risk of stroke. Mechanical properties of the arterial walls are significantly altered by atherosclerosis. The interaction between flowing blood and the artery wall is important in studying the development and progression of arterial disease and risk of stroke (Ku, Giddens et al. 1985, Ku 1997). Since the ICA supplies blood to the brain, plaque buildup in this branch of the CCA is generally considered to be more clinically relevant than that

in the ECA. A magnetic resonance angiogram of a healthy and stenosed carotid bifurcation artery is provided in Figure 1.2. The next section presents a discussion on the motivation of the present study.

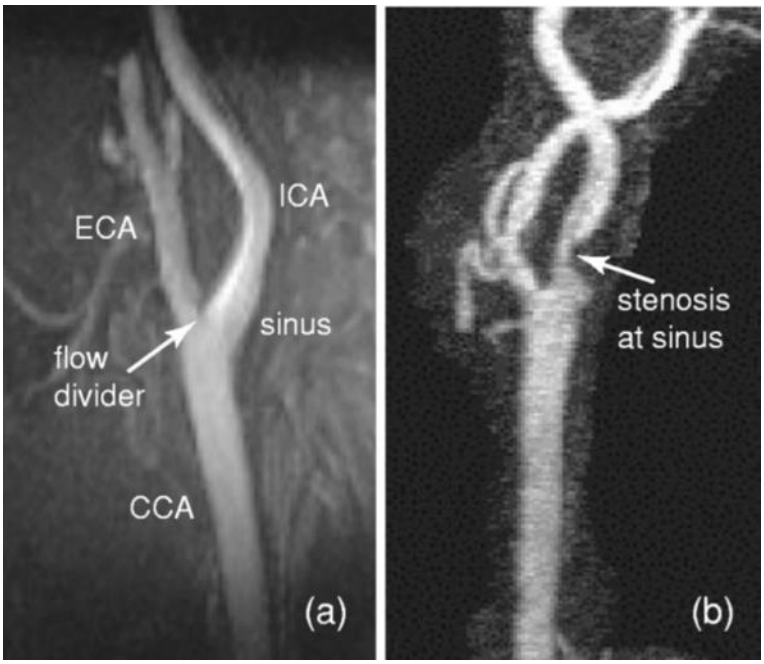

Figure 1.2. Magnetic resonance angiograms of (a) a healthy carotid bifurcation, (b) an atherosclerotic carotid bifurcation. CCA-common carotid artery; ECA-external carotid artery; ICA-internal carotid artery. Obtained from (Bale-Glickman, Selby et al. 2003).

1.1 Motivation of the Present Study

Although there has been more than thirty years of cardiovascular research, the fluid dynamics of arteries are still poorly misunderstood (Zhang, Agnoletti et al. 2014). Fluid dynamics is a subject of paramount importance due to the conventional relationship between the hemodynamics, endothelial cell response, and vascular pathology (McDonald 1974; Fung 1993). Physiological fluid flow is proclaimed to be laminar and organized. In contrast, diseased conditions are strongly coupled with transitional or turbulent flow, complex flow patterns, and

separating or stagnating flow. However, understanding and probing the fluid dynamics of physiological systems in vivo is exceptionally challenging. Simplifications and idealizations are necessary in order to study the flow phenomena under controlled in vitro experiments. Nonetheless, even under these conditions the challenges are massive.

Complex flow patterns and fluid-structure interactions (FSI) emerge within short, curved, branching, elastic tubes that undergo dynamic motions while interacting with propagating and reflecting pressure waves (Pedley 2000). The pressure driven flow is considered to be transient, transitional, anisotropic, and inhomogeneous, and is dependent on the frequency and phase of the driving pressure. Entrance effects, unsteady separation, and formation of secondary vortices are also prominent. Comprehensive investigations of such complex flows are hindered by limitations of current experimental and computational tools. Prediction of vascular disease or design of effective prosthetic devices cannot be done without a fundamental understanding of the physical phenomena that lead to pathological flow conditions.

A key example of fundamental deficiencies is the use of vascular stents, particularly in coronary arteries, where flow dynamics are further complicated due to a flow and pressure phase offset and dynamic curvature changes. Stents are a class of cardiovascular implants used to re-open arteries and re-new normalized blood flow. A stent is a cylindrical tube shaped medical tool used for invasive therapy to treat stenosis that has developed inside a blood vessel resulting from arteriosclerosis obliterans or other causes. The overall procedure is nominally invasive and clinical studies indicate superior long term patency versus other methods. As a result, stents have received widespread acceptance and emerged as the prevailing treatment for stenosed arteries.

Millions of stent implant procedures are performed each year. The use of stents has dramatically increased since their approval by the United States Food and Drug Administration in 1994, largely because of therapeutic and technological advances. In 1998 over 800,000 stents were implanted in more than 500,000 patients in the United States (Topol 1998). Recent advances in materials, fabrication procedures, and new drug coatings open possibilities for the use of stents beyond treatment of stenosed arteries. For example, stents can be employed for treatment of aneurysms or as vehicles for targeted drug delivery. However, despite their widespread use and numerous clinical studies, stents are implanted into arteries without *a-priori* understanding of the associated fluid dynamics. The positioning of stent struts in the bifurcation and the stresses generated in the stent and vessel wall are worthy of investigation for a better understanding of the mechanical behavior of artery wall.

Few experimental investigations into the hemodynamics of stented arteries exist, due to many reasons that made computational studies difficult (Duraiswamy, Schoephoerster et al. 2007; Lewis 2008; Charonko, Karri et al. 2010). Also, despite extensive previous work there is practically no research on the effect that compliance variation and discontinuities have on the hydrodynamics (Selvarasu, Tafti et al. 2011; Shuib, Hoskins et al. 2011). Moreover, although healthy physiological flow is primarily laminar and organized, in contrast, diseased conditions, namely inflammation, atherogenisis, or thrombus formation, are linked to complex and transitional flow that is attributed to localized changes of the geometry and the mechanical properties (McDonald 1974; Fung 1993; Batchelor 2002; Selvarasu, Tafti et al. 2011). One difficulty for experimental studies is matching the physical scaling of the small coronary vessels, as it is often difficult to create full dynamic similarity with a scaled-up model, and achieving

sufficient spatial resolution and accuracy at a 1:1 scale is challenging (Charonko, Karri et al. 2010).

Previous studies have overcome some difficulties in working with compliant models by using dye visualization in large-scale models (Berry, Santamarina et al. 2000), or performing quantitative measurements in idealized, scaled-up, rigid fixtures (Natarajan and Mokhtarzadeh-Dehghan 2000; Benard, Coisne et al. 2003). Many studies have used idealized velocity profiles, and none took into account the effect of phase angle between the pressure and flow, which occurs in the coronary arteries (Qiu and Tarbell 2000). Also, previous studies have been subjected to several assumptions, simplifications, and limitations. Some studies have neglected the effect of the stent deployment strategy and the post-stent injury causes to the artery that would contribute to restenosis (Selvarasu, Tafti et al. 2011). The effect of changes in mechanical stresses in the vessel wall might be important and affect vessel remodeling (Selvarasu, Tafti et al. 2011). Although, this effect is compounded by the combined hemodynamic changes, and literature suggesting that changes in hemodynamics would affect stenosis is extensive. Yet, if and how compliance mismatch affects the local hemodynamics is unresolved. The next section presents the ultimate goal and specific objectives of the present study.

1.2 Ultimate Goal and Specific Objectives

The challenges associated with resolving physiological flows include: understanding the fundamental physics of physiological flows; understanding the source of disease processes and their relation to fluid flow and transport processes; developing novel and improved disease diagnostics, treatment methods and implantable devices; and developing biologically-inspired systems and devices. As a result, the ultimate goal of the present study is to aid in the

development of tools to assist in the treatment of CVD and atherosclerosis. Gaining an understanding of hemodynamic parameters for medical implants allow clinicians to have some patient-specific proposals for intervention planning. By enhancing technical knowledge in this area of cardiovascular research, the present study incorporates experimental and computational models which include supplementary "non-idealized" features and parameters than previous studies have. The next section presents the specific objectives. The specific objectives are denoted "Obj" and sub-objectives "Sub-obj". The subtasks of each sub-objective are bulleted.

(Obj 1.) Develop an arterial cardiovascular experimental phantom to determine the effect of orthostatic hypotension on hemodynamic parameters.

(Sub-Obj 1.) Design and fabricate a cardiovascular experimental phantom that contains the aorta, major arteries, and the veins and capillaries mimicked with a resistor.

- Design a pulse duplicator that can duplicate physiological conditions (pressure, flow rate, frequency, and temperature).
- Instrument the cardiovascular experimental phantom with pressure and flow measuring devices.
- Determine a test protocol for evaluating the cardiovascular phantom in transient studies.
- Obtain physiological data (flow rate, pressure, normal stress, wall shear stress, and vorticity) during transition from bed-rest to upright position.
- Determine the effect of physiological Peclet numbers on mass transport in the phantom.

(Sub Obj 2.) Develop and design a digital cardiovascular phantom for transient studies.

- Obtain physiological data (flow rate, pressure, normal stress, wall shear stress, and vorticity) during transition from bed-rest to upright position.
- Determine the effect of physiological Peclet numbers on mass transport in the phantom.

(Obj. 2.) Develop methods to model patient-specific arterial geometries to predict hemodynamic forces on arterial grafts and implants.

- Develop a code to import patient-specific CTA scans and create numerical arterial core geometries.
- Use particle imaging velocimetry (PIV) to analyze the flow field.
- Determine the overall forces that act on implants.
- Determine the effect of stent design on hemodynamic forces.

Chapter 2 provides a review of literature on past and current work in the area of experimental and computational cardiovascular hemodynamics, stent technology, and drug eluting stent analyses. Chapter 2 characterizes the gaps in knowledge of the review of literature. Chapter 3 addresses the methods and materials of the present study. In Chapter 3, each of the measuring tools and devices used in addition to calibration methods and computational methodologies are addressed. Chapter 4 addresses the results of the present study. Chapter 5 provides a conclusion in addition to recommendations for future work.

CHAPTER 2

Literature Review

Chapter 2 provides a review of literature on past and present work in the area of cardiovascular disease and hemodynamics. Experimental and computational models that were developed and used by several research groups to simulate the functional behavior of arteries under normal and diseased conditions are discussed. The overall goal of experimental and computational modeling is to develop patient-specific predictive models which aim to assist in the improvement of: cardiovascular diagnosis, therapy planning and treatment of cardiovascular diseases (Menasche 2010; Siebes and Ventikos 2010). However, the achievement of this goal is underpinned by the characterization of the underlying physiological mechanisms derived from solid mechanics and fluid mechanics. The following sections outline the current state of knowledge in the area of hemodynamics, both computational and experimental, and categorize the questions left unanswered. The next section will provide an introduction of the pathogenesis of atherosclerosis.

2.1 Cause and Pathogenesis of Atherosclerosis

Atherosclerosis is defined as a vascular system disease that hardens and narrows the arteries. The disease typically does not become symptomatic until there has been significant disease progression. The set phase for atherosclerosis is when the endothelium of a blood vessel is damaged by hypertension, viral infection, diabetes mellitus, or other causes. Monocyctes adhere to the damaged endothelium which results in penetration of endothelium layers and transformation into macrophages. Macrophages and smooth muscle cells absorb cholesterol and neutral fats from the blood and procure a foamy appearance. These are termed foam cells and

are visible as a fatty streak on the blood vessel wall. Platelets also adhere to areas of the damaged endothelium sites, de-granulate, and release platelet-derived growth factor (PDGF). PDGF stimulates mitosis of smooth muscle which eventually leads to a mass of lipid, smooth muscle, and macrophages called atheroma (atherosclerotic plaque). The muscular and elastic tissue of the artery becomes increasingly replaced with scar tissue. When atheroma becomes calcified, it becomes very dense plaque. Such plaque formation results in arterial rigidity termed arteriosclerosis.

There are several surgical techniques that are used to treat atherosclerotic symptomatic patients. However, these treatments require precise knowledge of the severity of the plaque formation. Atherosclerotic plaque leads to secondary clinical events by any combination of the following three mechanisms: (i) thrornbolytic occlusion at the site of the stenotic plaque (ii) release of emboli that become lodged distally causing significant flow reduction, and (iii) chronic reduction of blood flow due to hemodynamic significant stenosis. Stroke is the third leading cause of death in North America (Gorelick 1995). Stroke is one conceivable secondary clinical event caused by atherosclerosis.

A number of studies have estimated that up to 80% of al1 strokes could be prevented through lifestyle changes (Gorelick 1995). An important step towards reducing stroke risk is to improve the identifying process of individuals who are at risk. Accurate diagnosis and assessments of carotid atherosclerotic disease is paramount so that low-risk plaques and high-risk plaques can be differentiated. Part of the vasculature that is of specific interest is the carotid bifurcation because it has been identified as a significant site for generation of cerebral emboli. While it is often difficult to determine the origin of an ischemic event retrospectively, it is estimated that between 20% and 30% of all strokes (ICA) has a structure that is unique to the

vasculature. It is now widely accepted that arterial geometry and hemodynamics influence the initiation and progression of disease (Glagov, Zarins et al. 1988).

Regions of slow and recirculating blood flow are particularly susceptible to deposition of atheroma (Oshinski, Ku et al. 1995). However, regions of high wall shear stress are associated with rupture of vulnerable plaque (Slager, Wentzel et al. 2005). A robust correlation has been revealed between the degree of lumen narrowing (due to plaque) of the ICA and risk of stroke. Degree of lumen narrowing also correlates with optimal patient management, where symptomatic patients with severe stenosis are best treated surgically while those with mild stenosis are best managed by drug therapy. These results have placed renewed emphasis on the development of clinical treatment techniques.

Estimates of stenosis severity can be made directly from measurements of lumen geometry (Desouza, King et al. 1991; Smith, Rutt et al. 1996) or indirectly from measurements of blood-flow within diseased arteries. Verifying the precision and accuracy of clinical techniques can be quite difficult since there is often no benchmark method in which comparisons can be made. Because of these issues, objective evaluations of clinical techniques often include *in vitro* experiments using vascular phantoms with realistic geometries. The next section presents a discussion on methods of treatment for atherosclerosis and arteriolosclerosis.

2.2 Survey of Treatment Methods for Atherosclerosis and Arteriolosclerosis

The first ground-breaking and still commonly used method of treating atherosclerosis is coronary artery bypass surgery. In this treatment method, fragments of the great saphenous vein of the leg or small arteries from the thoracic cavity are used to construct a diversion (bypass) from the aorta to a point on a coronary artery beyond the obstruction. Balloon angioplasty is a

treatment technique in which a thin, flexible catheter is threaded into a coronary artery to the point of obstruction. Afterward, a balloon tip is inflated to press the atheroma against the arterial wall which opens up the lumen. The practicality of balloon angioplasty is limited to well-localized atheroma.

An additional method is laser angioplasty, which consists of an illuminated catheter which enables the surgeon to view the diseased interior of an artery on a monitor. A laser is then used to vaporize atheromas and reopen the artery. These treatment methods are cheaper and less risky than bypass surgery. Conversely, there is particular concern that these methods of treatment may procure new injuries to the arterial walls. As mentioned in Chapter 1, stents are also used as a tool for arteriosclerosis treatment. Stents are implanted into the stenotic region of interest (ROI) on a balloon catheter, typically after angioplasty. The stent is then expanded until plastic deformation occurs, providing scaffolding-like features. The aim of the scaffolding feature is to prevent arterial recoil.

Stents of two types are generally available: bare metal stents (BMS) and drug eluting stents (DES). DES comprises of a pharmacologically active agent (medical treatment drug) that is delivered to the targeted stent deployment ROI site and is intended to reduce the stenosis. In several cases, the medical drug is integrated into and released from a polymeric coating (Parker, Dave et al. 2010) of sufficient capacity to accommodate the selected dose and to modulate its delivery to the ROI (Yang and Burt 2006; Wessely 2010). Provided that stents are extensively used for treatment of coronary artery disease, they often induce adverse biological responses. One response is reduction in lumen size as a result of formation of the neointima within the first year of stent implant surgery. This process is termed restenosis. Another response is formation of blood clots inside the vessel termed thrombosis (ST).

Thrombosis and restenosis are the major drawbacks of coronary stent replacements (Topol and Serruys 1998; Kastrati, Mehilli et al. 2001). Both restenosis and ST presents a major issue and limitation of BMS, yet has been the advent of DES. Although all types of coronary stents can be associated with ST, there has been recent specific concern in relation to the ongoing risk of ST beyond six months after stent implanted surgery. As opposed to BMS, DES prolongs the development of vessel repair including endothelialization, and can trigger a thromogenic response leading to late thrombosis. Both these responses, restenosis and ST have been proposed to be affected by altered hemodynamics inside the stented vessels. Percutaneous coronary intervention (PCI) of atherosclerotic disease located in coronary bifurcations has always been challenging, as a high restenosis rate persists even after implantation. Numerous experiments have been performed on developing arterial stents (many of which involving animals), not to mention the need for clinical trials before accreditation is finally granted.

The time period evolving from "a good stent design idea" to regulatory approval has led to the question of whether numerical modeling could be used to optimize stent designs. Undoubtedly, only those stents which show promising results in laboratory and clinical trials are retained and those that do not are discarded after considerable investment. In the early years the drug release mechanism was very poorly understood, but through mathematical modeling approaches, combined with experiments, researchers have helped identify the dominant mechanisms of release in a number of stents. While release experiments alone can give information regarding the release profile and the duration of release, the data generated is for one particular set of parameters (e.g. coating thickness, drug type and concentration) and the experiment needs to be repeated for each parameter measured. Once substantiated, numerical

models have the advantage of allowing several parameters to be varied and the release profiles compared without the need to repeat the experiments.

The ability of a numerical model to help identify the important parameters that govern the drug release is instrumental. Numerical modeling can also play an important role when an understanding of the drug distribution within arterial tissue is required. Cardiologists have often stressed that uniform drug concentrations across the wall are desired, and that these concentrations should be maintained within some minimum therapeutic and toxic levels. Obtaining this kind of information from experiments is extremely challenging, yet free and bound drug concentration profiles can readily be output from a mathematical model. However, experiments and numerical modeling must go hand in hand. The accuracy of the model results can only ever be as good as the quality of the inputs, especially when the model is sensitive to changes in one or more of the parameters.

The accurate determination of system parameters remains one of the biggest challenges in the field due to the natural variation between species and the complexity involved in making the required measurements, especially in the in vivo situation. However, some recent progress has been made by combining *in vitro/ex vivo* experiments with simple numerical models, and this approach may continue to yield useful results in the future. Conclusions which can be drawn from modeling have provided useful insights, some of which are counter-intuitive. Among the many other benefits of adopting a modeling approach include the potential to indicate at an early stage the designs that are doomed to failure, to design stents that are optimized and to result in a reduction in the number of experiments required. The next section provides a comprehensive review of the modeling of drug-release from arterial stents and the subsequent arterial drug redistribution.

2.3 Numerical Modeling of Drug Release from Arterial Stents

A vital aspect in the performance of any DES is the drug concentration/release profile. If too much drug is delivered then toxicity can arise, whereas if too little drug is delivered then it may have no effect at all. Of course, this ‘‘therapeutic window’’ varies between drugs and between patients and after implantation. Stent manufacturers routinely test the release of drug from their stents in an *in vitro* environment to gain an understanding of the shape of the release profile and to compare the release profile of different devices. This allows the manufacturers to determine the repeatability of the release profile. Whereas the *in vitro* release is unlikely to replicate the *in vivo* situation, it is nonetheless an important step in the development process. From the modeling perspective it makes sense to start with simple models, and in particular, it seems sensible to firstly consider modeling release in a controlled *in vitro* environment before embarking on the highly complex *in vivo* situation.

A number of authors have focused specifically on modeling the release of drugs from DESs, electing to put to one side the range of complexities that are observed in the in vivo situation (including flowing blood, pulsatile nature of flow, wound healing, proliferation, migration of cells and complex uptake/binding). This approach has proven to be useful in helping to address the question of which mechanisms are behind the release of drug from a number of stent systems and also in allowing estimates of parameter values (e.g. diffusion coefficients) to be made. However, modeling drug release is not an area of research exclusive to DESs. In fact, scientists have been devising models which describe the release of drug from tablet formulations and drug delivery devices for decades. It is therefore not a surprise that the early models of drug release from DESs incorporated well-established ideas from other applications.

Newer generation DESs which have focused on biodegradable polymers and polymer-free modified surface designs are likely to have more complicated mechanisms of release, and so it is of industrial relevance to consider these types of stents in their own right. In the case of stents with biodegradable polymeric coatings, the drug release may involve diffusion, erosion and possibly dissolution and/or swelling (Siepmann and Siepmann 2008) and (Fredenberg, Wahlgren et al. 2011). However, in the case of polymer-free stents, it is less clear how the sustained release is obtained and how this may be modeled. Because of the complexities involved in systems which degrade as they release drug, a model which is shown to be accurate for one system may be useless for another. Table 2.1 provides an overview of DES literature.

Newer generation DESs which have focused on biodegradable polymers and polymer-free modified surface designs are likely to have more complicated mechanisms of release, and so it is of industrial relevance to consider these types of stents in their own right. In the case of stents with biodegradable polymeric coatings, the release of the drug may involve diffusion, erosion and possibly dissolution and/or swelling. Some of the common processes which appear in these models include: hydration, degradation and erosion. Hydration is simply the process of combining with water. Degradation is a chain scission process which involves the breaking of polymeric chains by free radicals. On the other hand, erosion is material loss from a system and can be either surface erosion or bulk erosion. With surface erosion, water intrusion into the polymer is slow compared with the rate of degradation, thus the polymer is ‘eaten away’ from the outside to the inside. With bulk erosion, the rate of degradation is slow compared with the rate of water uptake and so the entire system is rapidly hydrated and degradation occurs throughout the whole material equally.

Table 2.1

Survey of Drug Eluting Stent Computational Studies.

Author	Study	Parameters	Conclusion	Recommendations
(X. Zhu 2014)	This work presents a model that describes the integrated process of drug release in PLGA coating and subsequent drug delivery in the arterial wall.	Bound, internalized, and free drug concentration and strut embedment	The developed model here provides the basis for evaluating and studying a PLGA coating for stent applications, with the ease of adaptation to more sophisticated scenarios (e.g., consideration of more pathological conditions).	Factors related to the pathological conditions; such as plaque, thrombus, and regions of tissue compression should be considered in future work.
(Zhu, Pack et al. 2014)	This paper mathematically models the integrated process of (1) the delivery of a hydrophobic drug from a drug-eluting stent with biodurable polymeric coating and (2) drug distribution in the arterial wall with reversible binding.	Free and bound drug	Drug release from an implanted drug-eluting stent is affected by the surrounding arterial wall via the vascular drug diffusivity and reversible binding reaction, which implies a potentially large difference from in vitro release behaviours of a hydrophobic drug.	Future studies should incorporate design optimization studies with reversible reacting mechanisms.
(M. Horner. 2010)	The main goal of this study was to combine a realistic geometry for the deployed stent and vessel wall with a newly proposed two-species computational model for drug transport.	Free and bound drug	The model was shown to exhibit the correct behavior when drug binding affinity, diffusivity, and wall plasma convection were varied. Therefore, the model is useful for studying the effect of drug physicochemical properties and local transport factors on drug distribution and retention in the vessel wall.	Future directions for this work include modeling the coating and finite drug reservoir, the presence of thrombus, or allowing for neighboring or overlapping stents. The latter might require the inclusion of luminal flow in the model to achieve the correct delivery patterns

Prabhu and Hossainy (2007) focused specifically on the degradation and release of everolimus from a polylactic (PLA) stent coating and validated their compartmentalized model

using *in vitro* data. The model considers two non-linear reactions: the hydrolysis (by water intrusion) of PLA to produce oligomers and lactic acid and the hydrolysis of oligomers to produce lactic acid. Five reaction diffusion equations are presented to describe the temporal and spatial evolution of the concentrations of water, PLA, oligomers, lactic acid and everolimus. The model equations were solved using an iterative finite difference approach which updates estimates of the various parameters via comparison with the experimental data. The authors indicate that autocatalysis (i.e. a reaction where the reaction product itself is the catalyst of the reaction) is important and cannot be ignored. While not directly focusing on DESs, (Siepmann and Gopferich 2001) provided a review of the mathematical modeling of bioerodible polymeric drug delivery devices. The authors considered only systems where the drugs are physically immobilized within a water insoluble polymeric matrix. The authors stressed that accurate physiochemical characterization of the investigated system is an absolute pre-requisite for the appropriate mathematical modeling of the device, and as such they detail techniques to experimentally characterize degradation and erosion. These can help identify whether the erosion is surface or bulk and assist in clarifying the time-dependence of the diffusion coefficients.

The model used in the study of (Lee 1980) lends itself to an approximate analytical solution for drug release from thin eroding films and the models of (Joshi and Himmelstein 1991) which accounts for acid producing species that accelerate matrix hydrolysis. The authors comment that modeling efforts should try to take into account the *in vivo* conditions since, for example, cellular tissue reactions can affect the degradation process. Again, not referring specifically to DESs, (Rothstein, Federspiel et al. 2009) present a unified model for the prediction of controlled release from surface and bulk eroding polymer matrices which also

accounts for the transition from surface eroding to bulk eroding behaviour during the course of degradation. The study of (Soares and Zunino 2010) introduced a mixture model for water uptake, degradation, erosion and drug release from polydisperse polymeric networks. Each constituent of the model represents chains of an average size. A multiscale description of degradation and erosion is proposed, combining the molecular description of scission with Fick's macroscopic laws of diffusion. The approach adopted here describes degradation by means of the time evolution of weight fractions of polymeric constituents of average degree of polymerization. The authors argue that the key advantage of their model is the fact that polymer degradation is described as an individual chemical reaction.

In the study of (Baran, Ogino et al. 1997), a bioresorbable DES model based on detailed constitutive equations and taking into account the main physical and chemical mechanisms involved in coating degradation, drug release and restenosis inhibition was used. Their results were verified against selected *in vitro* and *in vivo* data available in the literature. In the study of (Hill 1983), the authors considered a two dimensional dissolution–diffusion model which also included surface erosion. In the study of (Korakianitis and Shi 2006), the authors reported that the drug may exist in the coating in a form which needs to dissolve before it can diffuse. The authors considered the drug in polymer as two separate phases: a dissolved phase and a solid phase with concentrations $C_f C_f$ and $C_b C_b$, respectively. Only dissolved drug is allowed to diffuse. The authors included a source term in the diffusion equation to account for the solid phase dissolution. The next section presents a review of literature on modeling the drug transport in the arterial wall.

2.4 Survey of Numerical Drug Eluting Stent Studies

Modeling the release of drug from arterial stents is only a one part of the story. What happens to the drug after it is released *in vivo* is of more clinical interest and certainly more difficult to model. Clinicians advise that a uniform drug concentration should be attained across the arterial wall, and the concentration should be maintained within some therapeutic window. Thus an understanding of the structure and components of the arterial wall is crucial. The arterial wall is a porous heterogeneous structure, consisting of three distinct layers. Closest to the lumen is the intima, followed by the media and finally the adventitia (Panerai 1980).

The intima consists of the sub-endothelial space and the endothelial layer of cells, known as the endothelium. This layer is crucial to the control of the normal function of the artery, through its mediation of relaxation and contraction and via its control of smooth muscle cell proliferation within the underlying media layer. The internal elastic lamina forms the outermost part of the intima. The media region comprises smooth muscle cells, collagen and elastin. Finally, the outermost layer of the arterial wall is the adventitia. The adventitia tethers the artery to perivascular tissue, and contains cells known as fibroblasts as well as a network of small blood vessels, called vasa vasorum, which act as a blood supply to the adventitia and provide a clearance mechanism for drugs released into the artery wall.

2.5 Survey of Current Bifurcation Stent Implant Issues

The introduction of polymer-based anti-flammatory and anti-proliferative drugs released in a controlled manner from coronary stents has changed the treatment results of PCI considerably. However, patients with certain multifaceted lesions have consistently been excluded from most trials undoubtedly because of the combined distress of problems with obtaining a high procedural success rate and of the difficulties in interpreting the angiographic

and clinical results. Coronary bifurcations are periodically encountered and roughly 15-20% of percutaneous coronary interventions (PCI) are implemented to treat bifurcations (Latib, Colombo et al. 2009). PCI for bifurcation disease has been deliberated as a technically challenging procedure. PCI has also been associated with lower procedural success rates and inferior clinical outcomes than bifurcation lesions. Furthermore, there has also been enormous uncertainty and debate as to the most appropriate treatment strategy when dealing with bifurcations. However, in recent years noteworthy improvements have occurred in the overall understanding and treatment of bifurcation lesions.

Initially, the introduction of DES have meaningfully reduced restenosis and repeat revascularization rates demonstrated in both archive studies and a sub-analysis of the randomized SCANDSTENT trail (Steigen, Maeng et al. 2006; Thuesen, Kelbaek et al. 2006). SCANDSTENT was a randomized, controlled study that showed the beneficial effect of drug-eluting stents compared with bare-metal stents in a large series of entirely complex coronary artery lesions. The superiority of the sirolimus-eluting stent was evident in all subgroups of patients, and among patients who had received the drug-eluting stent, target lesion revascularization was only necessary in those with bifurcation lesions.

Early results using balloon angioplasty alone to treat bifurcation lesions demonstrated relatively low angiographic and clinical success rates and high restenosis (George 1986). Although the introduction of coronary stents resulted in more predictable results and higher success rates, angiographic restenosis rates remain high, despite the use of different approaches (Lefevre, Louvard et al. 2000; Sheiban, Albiero et al. 2000; Yamashita, Nishida et al. 2000; Karvouni, Di Mario et al. 2001). Additionally, a more selective usage of two stents as intention to treat has been implemented. Also, the acceptance of a suboptimal result in the side branch

(SB) due to the fact that many residual stenosis at the SB may not be physiologically significant. Fourthly, the better performance of two stent techniques associated with high pressure post dilatation, kissing inflation and possible intravascular ultrasound; and finally the publication of numerous trails specifically in bifurcations.

Consequently, these changes and outcomes after bifurcation PCI have improved considerably and in some studies approximate those of non-bifurcation PCI. There have recently been randomized trails and a large archive comparing provisional strategy of main branch (MB) stenting with 1 DES vs. a 2 DES strategy of stenting both branches. From these reports, it is evident that the percutaneous treatment of coronary bifurcation has progressed in a manner that one stent vs. two stent appears to have been resolved. The provisional approach of implanting one stent on the MB is now considered the default approach in most bifurcation lesions. This approach is mainly due to the fact that routine implantation of two stents does not give superior results compared to selective usage.

Despite the simplicity of the provisional approach, this technique frequently leaves the SB with a significant residual stenosis (most trials evaluating the provisional approach quote success as 30% residual on the MB and less than 50% residual on SB). The results follow implantation of two stents is sometimes suboptimal and therefore the follow up is inferior to expected. Operator experience, willingness to devote sufficient time and effort to optimize the result (especially on the SB) and usage of intravascular ultrasound elements frequently needed when implanting two stents. In the work of (Latib, Colombo et al. 2009), the authors experienced a stricter adherence to this approach and the results have contributed to the improvement seen over the last few years following implantation of two stents in bifurcation lesions. However, the introduction and perfection of dedicated bifurcation stents may simplify

this task and change the current proposed approach to bifurcation treatment. Presently routing stenting of both branches appears to offer no advantage over a provisional approach. A more detailed overview can be found in (Colombo, Moses et al. 2004). The next section presents a discussion on fluid-structure interaction of arteries.

2.6 Survey of Computation Arterial Hemodynamic Studies

In the efforts to analyze the cardiovascular system and effects of diseases on it different ways of analyzing hemodynamic parameters are practical such as lumped model, one, two or three dimensional modeling and experimental methods. In this section lumped, one, two and three dimensional models are discussed. Lumped models (zero dimensional) and one dimensional models are electrical circuitry models that provide only time dependent data for hemodynamic studies. Electrical components used in the electrical circuit are used as a surrogate for fluid parameters. A review of lumped and one dimensional studies are provided in Table 2.2.

The use of mathematical models in the simulation of cardiac dynamics plays a vital role in understanding cardiac physiology and pathology and possible treatment techniques. Early studies were performed to understand and simulate healthy cardiac dynamics at the physiological scale (Arai, Alpert et al. 1993) or to describe cardiac contraction (Aroney, Herrmann et al. 1989). For example, researchers have developed several time varying elastic models for modeling the ventricular at the organ level. Mathematical functions took over the role to initiate the simulation of the hemodynamics at the organ level (Arts, Bovendeerd et al. 1991; Beuckelmann, Nabauer et al. 1992; Beltrami, Finato et al. 1994; Atar, Gao et al. 1995). In these models, the activation function was defined using trigonometric, polynomial or exponential functions. In time varying elastic models, only blood pressure and volume can be simulated.

Table 2.2

Survey on One Dimensional Cardiovascular modeling techniques.

Application	Model Feature	Studies
Ventricular assist device support for heart failure	The native cardiovascular system was in heart failure condition, and a VAD model is coupled	1. Studies of cardiovascular response in the heart condition of VADs (Voitl 2009) 2. Studies of cardiovascular response in the heart failure condition support with intra aortic balloon pumps 3. Comparison of the assistance action of different types of VAD and VAD motion profiles. 4. Study of the effect of the inlet and outlet cannulation sites for connecting the VADs to the native cardiovascular system. (Shi, Korakianitis et al. 2007) 5. Study of the physiological control of pulsatility gradient in rotary blood pump (Bhattacharya-Ghosh, Bozkurt et al. 2014)
Study of cardiovascular response under neuro-regulation	The native cardiovascular system was coupled with the models for the nervous system	1. Simulate the cardiovascular responses under neuro-regulation in various conditions of isocapnic hypoxia hypercapnia and hypocapnic hypoxia (Ursino and Magosso 2000; Shi, Lawford et al. 2011) carotid occlusion (Aquino, Robinson et al. 2014) 2. Simulation of cardiopulmonary response in Valsalva manoeuvre (Lu, Clark et al. 2001; Aboamer, Azar et al. 2014) 3. Simulation of the cardiovascular response to orthostatic stress (Shaw, Loughin et al. 2014)
As boundary condition in multi-scales simulation of cardiovascular dynamics .	The 0-D circulation system model was coupled with the distributed parameter models (1D, 2D or 3D).	1. Multi-scale simulation of the cardiovascular dynamics (Formaggia L. Et al 1999; Pontrelli G. 2004)

However, in a failing heart a number of changes occur due to pathophysiologic mechanisms at different levels of biological organization.

Some models have attempted to understand the underlying mechanisms of contraction by increasing the level of complexity of mathematical models used to describe them, via the addition of relevant processes at different biological scales. For example in the study of (Hossainy and Prabhu 2008), the authors described the relationship between left ventricular pressure and volume, as well as systolic fiber stress and strain in the wall (Hossainy and Prabhu 2008) driven by an activation function to simulate the hemodynamics over a cardiac cycle. This model simulates the contraction of a single fiber at microstructural level, and extends this to a complete ellipsoid ventricle at microscopic level assuming homogeneous distribution and function of all muscle fibers, thus rendering ventricular hemodynamics. (Cox, Loerakker et al. 2009) used this model to describe the right ventricular hemodynamics in a healthy and pathological configuration by modifying the wall volume and zero pressure volume in the left ventricle (Cox, Loerakker et al. 2009). Diaz-Zuccarini and LeFevre (2007) modelled the contraction of a sarcomere and defined the ventricle as a cylinder. Also here, the ventricular dynamics were obtained with the assumption of a uniform sarcomere distribution in the ventricle.

Other models focus on cardiac cells and include the generation of the action potential. For example, the Luo–Rudy model (Luo and Rudy 1994) is widely used in electrophysiological literature to describe the ion fluxes and channel currents of a ventricular myocyte resulting in the transmembrane (action) potential. The numerical reconstruction of the ventricular action potential is based on a Hodgkin–Huxley type approach (Luo and Rudy 1994). An advanced model of the Luo–Rudy model is given by Livshitz and Rudy (Livshitz and Rudy 2009) accounting for the ion channel kinetics, calcium handling, and dynamic changes in the intracellular/extracellular milieu during the action potential. To consider the relevance of intracellular calcium dynamics during the excitation contraction coupling process (ECCP) of a

myocyte, the sliding filament model (SFM) (Rhodes, Ropella et al. 2003) describes its interaction and sensitivity with myofilaments within a sarcomere at the protein level.

The cardiac cell models mentioned above have been used to simulate physiological and clinical situations. However, these models do not take into account the connection between different biological scales, which is crucial for understanding cardiac physiology as a holistic process. Various approaches have been undertaken to understand the coupling between microscopic and macroscopic elements of the cardiac contraction and its physical mechanisms using mathematical models. Bhattacharya-Ghosh et al. presented a blueprint for a multi-scale model of the ventricle (Bhattacharya-Ghosh, Schievano et al. 2012). This model describes events in which relevant mechanisms are mathematically described and coupled at the protein, cellular and organ scales in order to provide a better understanding of the combined ECCP as a whole. However, this model does not incorporate the four heart compartments and circulatory loop.

A three-parametric model of heart muscle behaviors was introduced (Zacek 1996) and a modification of this model was presented later (Rideout 1991). It successfully predicted force development during a time period of heart, showing deactivation of the contractile element during isotonic shortening and the apparent dependence of series stiffness in time. The study of the series elasticity of cardiac muscle was presented (Rupnic 2002). Afterwards, the time-varying elastic model of the left ventricle was introduced and later the relationship between pressure-volume area and cardiac oxygen consumption was described (Helde 2002). Finite element methods are commonly used to simulate the left ventricular way of operation. The first computer models describing the arterial system were presented in the sixties. The authors constructed a multi-branched model of the systemic arterial tree in a form usable for digital

computer, which allowed simulation of different physiological and pathological conditions. This model was extended in detail later (Wang 2004). Also, blood flow through site of particular interest of the arterial tree such as anastomoses, stenoses and bifurcations can be described with finite element method simulation. The mathematical analysis of the whole human cardiovascular system remains as a complicated task and for that reason models are simplified with respect to particular parts of interest.

There is no single mechanism that can account for atherogenesis, other than being interpreted as the complex interaction of many processes (Van Wyk, Wittberg et al. 2014). Different slow acting biochemical and mechanical processes have been linked to the initiation or progression of the disease. The most recent sets of hypotheses relate low time-averaged and oscillatory wall shear stress (WSS) to regions prone to disease (Bharadvaj, Mabon et al. 1982; Bharadvaj, Mabon et al. 1982; Zarins, Giddens et al. 1983; Ku, Giddens et al. 1985; Gambillara, Montorzi et al. 2005). These fluid mechanical aspects are thought to increase residence times favorable to near wall biochemical processes and transport mechanisms of atherogenic materials towards these near wall sites (Bharadvaj, Mabon et al. 1982; Bao, Lu et al. 1999). Other studies suggest that high WSSGs lead to cell dis-orientation in the endothelial layer (DePaola, Davies et al. 1999; Nagel, Resnick et al. 1999; Farmakis, Soulis et al. 2004) or intimal hyperplasia that are regarded as possible initiators to atherogenesis (Depaola, Gimbrone et al. 1992; Haidekker, White et al. 2001; White, Haidekker et al. 2001). The analysis of each of these hypotheses is compounded by the pulsatile nature of blood flow and the consequentially large spatial flow variations in time. Table 2.3 presents a notable review of recent arterial hemodynamic computational studies.

Table 2.3

Review of Arterial Hemodynamic Computational Studies.

Authors	Study	Parameters	Conclusion	Recommendations
(Xiang, Siddiqui et al. 2014)	The objective of this study was to examine the sensitivity of widely used hemodynamic factors derived from CFD to different inlet waveforms under the same inflow rate.	This study specifically focus on WSS and OSI, the two independent parameters predictive of rupture in our multivariate logistic regression model	The authors stress that patient-specific flow boundary conditions are highly desired for image-based CFD simulations. However, only a few CFD studies have them	For studies of large cohorts aiming at finding statistical correlations between aneurysm rupture and hemodynamics, we may have to use non-patient-specific inlet boundary conditions in the current situation.
(Xiang, Tutino et al. 2014)	In Part 1 of this 2-part review, a hypothesis is proposed which includes: both high and low wall shear stress drive intracranial aneurysm growth and rupture through mural cell mediated and inflammatory cell mediated destructive remodeling pathways, respectively. Part 2, delineates different wall shear stress parameter definitions and survey recent computational fluid dynamics studies.	Wall shear stress	Computational fluid dynamics findings correlating both high and low wall shear stress with intracranial aneurysm growth and rupture puzzle researchers and clinicians alike. These conflicting findings may stem from inconsistent parameter definitions, small datasets, and intrinsic complexities in intracranial aneurysm growth and rupture.	Refinements are needed which will yield more accurate predictive models for intracranial aneurysm risk assessment from computational fluid dynamics
(Qiu, Fei et al. 2013)	This paper studies the influence of a High-Porosity Mesh (HPM) stent on the hemodynamic characteristics in the intracranial aneurysm based on the Computational Fluid Dynamics (CFD). An idealized basilar tip aneurysm model and a HPM stent model was built.	Wall shear stress	The following conclusions can be drawn: when applying the stent to treat the aneurysm, the wires of the stent impede the blood flow into the aneurysm sac, which would significantly reduce the magnitude of the impact force of the blood flow, the pressure and the WSS at the dome of the aneurysm wall.	Future results should not only provide a valuable reference for optimizing the stent design, but also help neurosurgeons to select suitable stents and to establish reasonable operation procedures.
(Hewlin and Kizito 2011)		Wall Shear stress, Normal Stress, and vorticity	dynamic behaviors of blood through the patient-specific carotid bifurcation arterial geometries based on numerical approaches showed differences when compared to a simplified model	Future studies should incorporate more realistic boundary conditions obtained from experimental data from flow phantoms or as an alternate blood flow rate obtained.

In order to study these hypotheses several experimental and numerical investigations implement various mean WSS based indicators to simplify the analysis of the temporal WSS variations in identifying atherosclerotic prone locations (Zarins, Giddens et al. 1983; Ku, Giddens et al. 1985; Pedersen, Oyre et al. 1999; Lei, Giddens et al. 2001; Soulis, Giannoglou et al. 2007). These indicators include the time averaged WSS (TAWSS), oscillatory shear index (OSI) and relative residence time (RRT). In the quoted studies indicators are usually shown to be well correlated with plaque affected regions, however also possibly in agreement with un-affected regions. The application and usefulness of these indicators in more complex arterial junctions is therefore not well understood.

2.7 Survey of Flow Phantoms and Measurement Techniques

Flow phantoms are a vital tool for studying hemodynamics of arteries using Doppler Ultrasound (DS) and Particle Image Velocimetry (PIV). In the production of realistic flow conditions, it is highly desirable to be able to produce arbitrary geometries, including branching stenosis, that closely mimic *in vivo* geometries. Usually, wall-less vessels have been employed to avoid mismatch problems in acoustic properties (Patterson and Foster 1983; Rickey, Picot et al. 1995; Guo and Fenster 1996), and to produce more complicated geometries by using a lost material casting technique (Poepping et al. 2002; Smith et al. 1999). Conversely, with employing wall-less vessels, the tissue-mimicking material (TMM) may be susceptible to changes due to exposure to air or water (Hoskins and Tamanarine 2000), incompatibilities with the blood-mimicking fluid (BMF) or breakage and leakage problems, as addressed by (Ramnarine, Anderson et al. 2001). Therefore, it is also desirable to have a completely sealed phantom, where the agar-based TMM is sealed from air or fluid exposure.

A number of flow phantoms are reported in the literature and have been reviewed by (Hoskins 1997). However, most of the flow phantoms previously developed have consisted of a simple geometry, such as straight tubes, or a stenosed geometry formed by shrinking tubes, inserting tapers or extracting rods. The development or more realistic phantom geometries has been primarily limited by the lack of versatile vessel-mimicking materials (VMMs). A major consideration for the development of a new VMM was the ability to fabricate a robust flow phantom, with vessels of anatomically accurate models, which can withstand physiological flow stresses. Key design considerations include robustness, stability, elasticity, wall thickness, speed of sound, acoustic attenuation, echogenicity and, finally, practical considerations for fabrication, such as versatility, variations in echogenicity and the incorporation of plaques or irregular surfaces.

Additionally, the main physiological features to be included are the wall thickness and elasticity. It is necessary to match the wall thickness for realistic imaging and to match the elasticity because of its contribution to the damping and propagation of the pulsatile waveform during flow. Studies have shown that the wall thickness of the carotid arteries is approximately 0.65 to 0.95 mm, depending on gender, race and duration of diabetes (Riley, Barnes et al. 1992; Folsom, Eckfeldt et al. 1994; BonithonKopp, Touboul et al. 1996; Wagenknecht, Dagostino et al. 1997). Also, arterial walls have been shown to have a nonlinear elastic behavior (Roach and Burton 1957), due to the different elasticities of the elastin and collagen components. The Young's elastic modulus of elastcity, 0.3 MPa is much lower than that for collagen, 300 to 2500 MPa (Dobrin 1978), and the resulting arterial elasticity is similar to elastin for normal physiological strains, and approaches that of collagen for much higher strains. The incremental Young's elastic modulus in the circumferential direction has been found, in normal human

abdominal aorta sections, to range from approximately 0.04 to 2 MPa for corresponding transmural pressures of 0 to 90 mmHg (0 to 12 kPa) (Drangova, Holdsworth et al. 1993) and, in the human iliac artery, to range from approximately 0.05 to 1.45 MPa for transmural pressures of 0 to 120 mmHg (0 to 16 kPa) (Ryan and Foster 1997).

The critical acoustic properties to be matched are the speed of sound (SoS) and the acoustic attenuation. Preferably, a VMM should be acoustically well matched to both the BMF and the TMM. A disparity in the speed of sound between the VMM and surrounding material (BMF or TMM) will produce reflection and refraction of the US beam, which can result in distortion of the Doppler spectrum (Thompson, Aldis et al. 1990). Few suitable materials have been found that match both the acoustic attenuation and the SoS of soft tissue (0.5 to 0.7 dB/cm MHz and 1540 m/s, respectively). Many materials have been investigated and described for use as the VMM in flow phantoms, as seen in the review by (Law, Johnston et al. 1989). C-flex (Cole-Parmer, Vernon Hills, NY) is one popular choice for a VMM, with a speed of sound (1553 m/s) similar to that of tissue, but with a much higher attenuation (28 dB/cm at 5 MHz) that varies with frequency to the power of 1.8 (Ramnarine, Anderson et al. 2001). Unfortunately, most of the materials suggested as a VMM are generally available only as ready-made tubing, such as C-flex and latex, and are, thus, limited to straight-tube or stenosed-tube geometries with a manufacturer- specified wall thickness and fixed echogenicity.

Silicone allows the opportunity to produce vessels with arbitrary wall thickness and lumen geometry, due to its availability in a liquid form that can be cast to form a flexible transparent elastomer. These elastomers are strong, yet compliant, chemically stable over time, and do not absorb a significant amount of water (unlike latex rubber). Silicone has been used previously to create tubes of various thicknesses for wave propagation experiments (Pythoud,

Stergiopulos et al. 1994), stenosed tubes for laser visualization and branched vessel models for flow visualization (Melbin, Gopalakrishnan et al. 1982), by painting layers of an elastomer (Sylgard 184) onto a rod or cast. A casting technique has also been used with this material to produce a branched carotid model for use with laser Doppler velocimetry and flow visualization (Cao and Rittgers 1998; Secomski, Nowicki et al. 2003). In what follows, the fabrication of a sealed, US compatible, flow test object that consists of a thin-walled silicone-elastomer vessel of arbitrary geometry embedded in a TMM is discussed.

Doppler methods are extensively used to quantify and visualize blood velocity in clinical practice. Typically the maximum velocity waveform is used to quantify the degree of lumen reduction in stenosed arteries, and indices based on the maximum velocity are used to quantify the shape of the waveform. Further quantification has been used in research, studies such as the measurement of velocity profile and volumetric flow (Picot and Embree 1994; Bohs, Friemel et al. 1995; Picot, Fruitman et al. 1995), wall shear rate (Brands, Hoeks et al. 1995; Forsberg, Morvay et al. 2000) and turbulence intensity (Poepping, Nikolov et al. 2002; Thorne, Poepping et al. 2008). The process of measurement of velocity and related quantities using ultrasound is complex and prone to error (Blake, Easson et al. 2009). Maximum velocity errors using spectral Doppler in clinical ultrasound systems have been reported in the range of 0-100% (Hoskins 1997). The maximum Doppler shift arises from one edge of the Doppler aperture, whereas angle correction is performed with respect to the center of the aperture (Hoskins and McDicken 1991)

Several CFD studies have examined flow through stenosed arteries. However, these studies normally depend on turbulence models that agree poorly with published experimental values. (Blake, Easson et al. 2009) reported that direct numeric simulation (DNS) of turbulence would appear to offer a solution, but studies are phenomenally computationally intensive, which

restricts their applications. While conventional CFD (i.e., non-DNS CFD) have been used to investigate flow in complex geometries, the geometry becomes more complex and the agreement between the CFD and experimental data is poorer. This discrepancy arises such that it is not understood whether it is the CFD or the experimental technique that is at fault or both. This situation outlines the need for validation methods based on experimentally measured data.

Previous experimental studies have used stenosis models to investigate the variation of measured velocity with degree of stenosis (Hoskins 1997; Poepping, Nikolov et al. 2002; Steel, Ramnarine et al. 2003). Generally, these studies contemplate the variation of estimated peak velocity with machine settings and with the degree of stenosis. (Bascom, Johnston et al. 1997) compared measured velocity using DUS with flow field visualization data measured using a photochromic technique. Both the ultrasound technique and the photochromic technique used either the same acrylic stenosis model or geometrically identical models. However, it is known that acrylic has a high speed of sound more than 2500 m/s (Hoskins 2008), which leads to distortion of the Doppler beam. In general, materials such as glass and Perspex, which are suitable for optically-based flow studies have very high values of the speed of sound and are unsuitable for use in ultrasound phantoms, which require materials whose speed of sound is closer to 1540 m/s.

(Blake, Meagher et al. 2008) developed a technique to estimate the wall shear rate in healthy arteries using a clinical ultrasound scanner. The method used a theory of fully developed oscillatory flow together with a spectral Doppler trace and an estimate of mean arterial diameter. A method using color of flow imaging was compared with the spectral Doppler method in vascular phantoms and was found to have errors that were on average 35% greater. Differences from the theoretic value for the time averaged wall shear rate using the spectral Doppler method

varied by artery: brachial 9%, carotid 7%, femoral 22%, and fetal aorta 17%. Test measurements obtained from one healthy volunteer demonstrated the feasibility of the techniques in vivo.

Blake, Meagher et al. 2008) used walled vascular phantoms with different lumen diameters to mimic the physiologic conditions for a range of arteries. The vascular phantoms were constructed from acoustically equivalent tissue-mimicking material (TMM) (Teirlinck, Bezemer et al. 1998) with a vessel-mimicking material made from c-flex tubing (Cole-Parmer, London, UK). Perspex boxes of dimension 30 x 10 x 10 cm (L x W x D) (Mike Bisset Plastics, Livingston, UK) were used to build the phantoms. Stainless steel rods of the appropriate diameter (RS Components, Corby, UK) were pushed through the tubing, which was subsequently pushed through the sides of the boxes and sealed with silicon. The liquid agar TMM was poured into the boxes. When the agar had set, the stainless steel rods were withdrawn, creating the arterial lumen inside the vessel mimic.

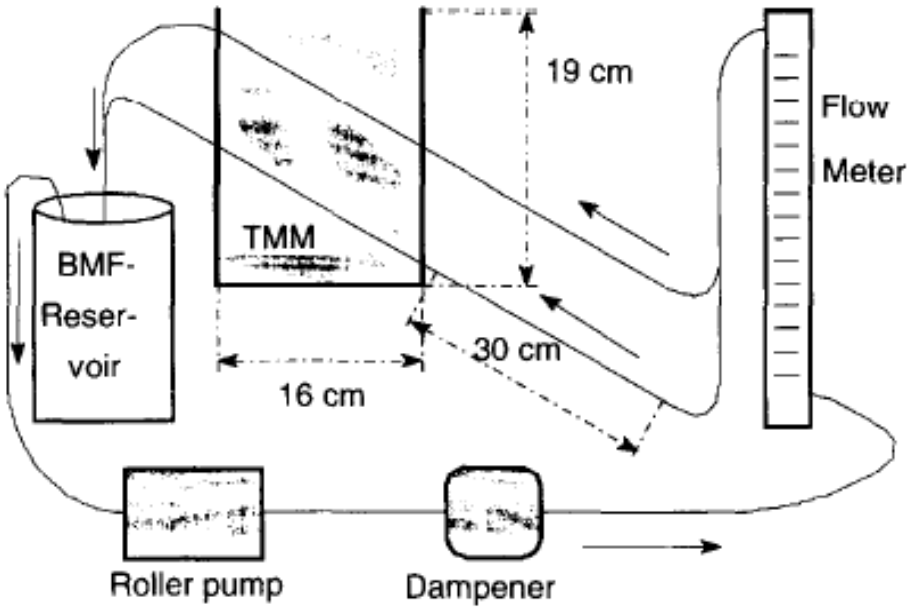

Figure 2.1. Schematic of the phantom flow system used in the study of (Blake, Meagher et al. 2008)

Each vascular phantom was connected into a flow driven by a gear pump (Micropump model 132, Micheal Smith Engineers Ltd., Surrey, UK) powered by an electric motor (M586TE, McLeannan Servo Supplies Ltd., Surrey, UK) and an external amplifier (4020-LS, Aerotech Ltd., Berkshier, UK). For the brachial and fetal aorta phantoms the working fluid was acoustically equivalent to human blood.

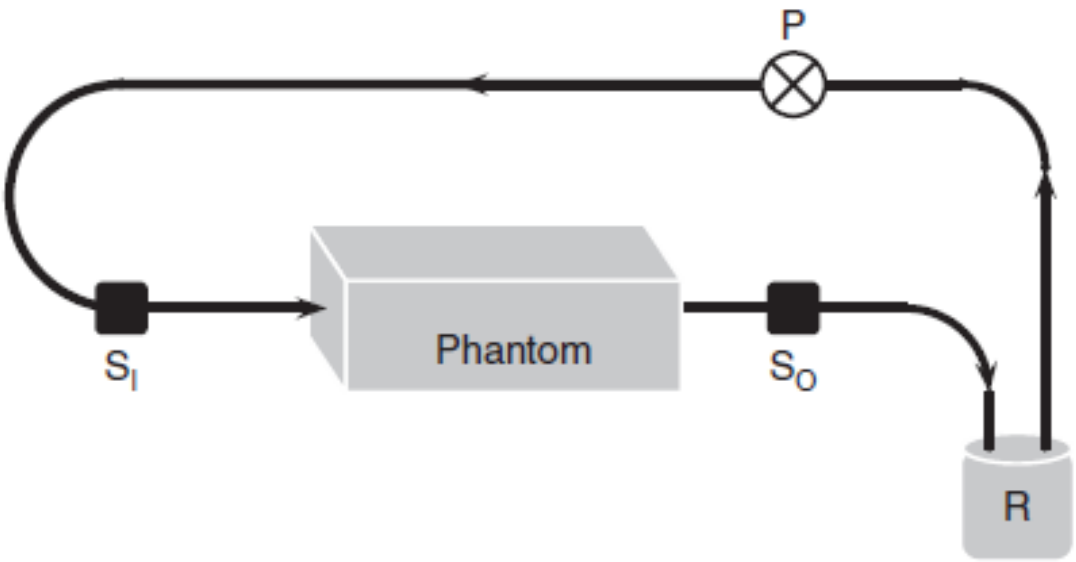

Figure 2.2. Schematic diagram of the flow circuit used in the study (Blake, Meagher et al. 2008).

There is a need to develop a method for validation of velocities measured in the region of a stenosis. This paper describes the development of a paired-phantom system for validation of velocity in the region of a stenosis, based on the use of particle image velocimetry. (Blake, Easson et al. 2009) developed a dual-phantom system for validation of velocity measurement in stenosis models. Pairs of phantoms with identical geometry and flow conditions were manufactured, one for ultrasound and one for particle image velocimetry (PIV). The PIV model is made from silicone rubber, and a new PIV fluid was made that matches the refractive index of

1.41 of silicone. Dynamic scaling was performed to correct for the increased viscosity of the PIV fluid compared with that of the ultrasound mimic. The degree of stenosis in the model pairs agrees to less than 1%. The velocities in the laminar flow region up to the peak velocity location agreed to within 15%, and the difference could be explained by errors in ultrasound velocity estimation. At low flow rates and in mild stenosis, good agreement was observed in the distal flow fields, excepting the maximum velocities. At high flow rates, there was considerable difference in velocities in the postenosis flow field (maximum centerline differences of 30%), which would seem to represent real differences in hydrodynamic behavior between the two models. Sources of error included: variation of viscosity because of temperature (random error, which could account for differences of up to 7%); ultrasound velocity estimation errors (systematic errors); and geometry effects in each model, particularly because of imperfect connectors and corners (systematic errors, potentially affecting the inlet length and flow stability)

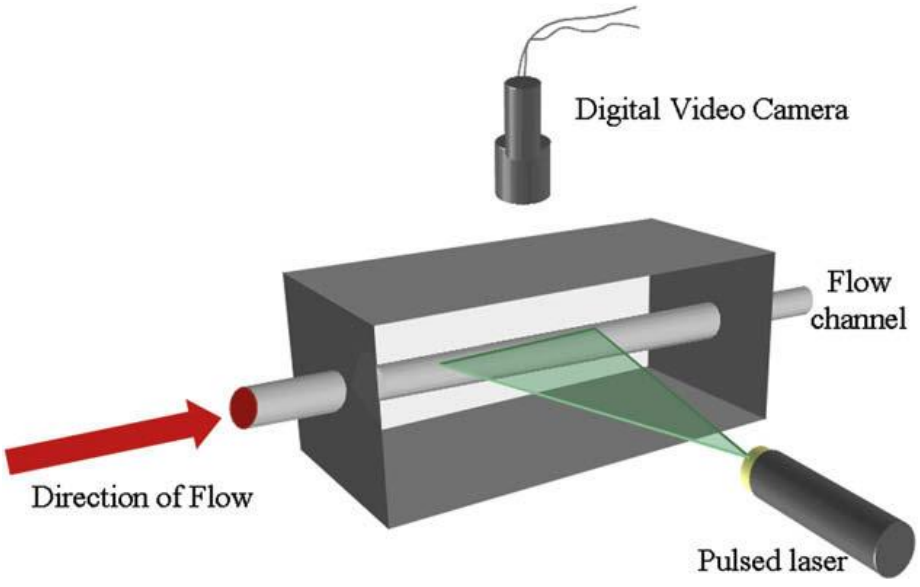

Figure 2.3. Components of the PIV system used in the study of (Blake, Easson et al. 2009).

Briefly, the flow circuit consisted of the vessel phantom described before connected to a gear pump at one side and a reservoir at the other side. The inlet was flush with the channel in the flow phantom and straight for a distance of one meter to ensure fully developed flow at the isonation site. The gear pump was computer controlled and able to provide steady or pulsatile flow. The blood mimic consisted of suspension of 5 micron nylon particles in a glycerol/dextran solution whose acoustic and viscous properties were blood equivalent. The flow rate through the circuit was measured with a graduated cylinder and a stopwatch.

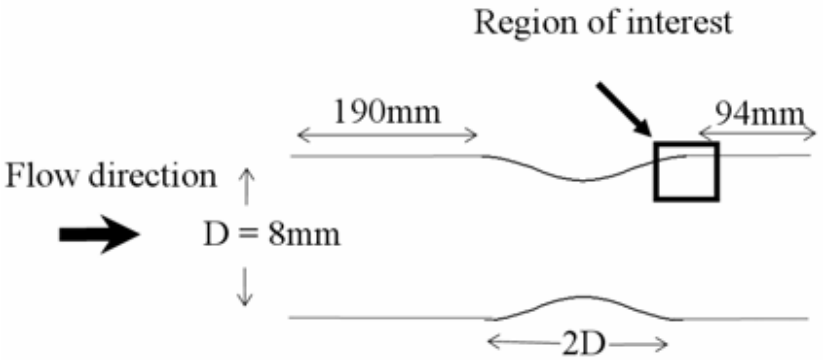

Figure 2.4. Schematic of the stenosis geometry with 30% diameter reduction (length not to scale). Obtained from the study of (Shuib, Hoskins et al. 2011).

Laser Doppler velocimetry (LDV) has been used to provide quantitative flow information, providing spatial velocity profiles and wall shear stresses (Bharadvaj, Mabon et al. 1982; Motomiya and Karino 1984; Ku and Giddens 1987; Rindt and vonSteenhoven 1996). In the study of (Motomiya and Karino 1984), detailed quantitative information on flow streamlines within the carotid bifurcation by photographing a suspension of polystyrene particles in wintergreen oil using a cine camera were obtained. Images were analyzed frame by frame to provide detailed maps of flow lines, including quantification of flow velocities, and of wall shear stresses. The studies demonstrated that there is a large flow recirculation region in the carotid

sinus where wall shear stresses are very low, whereas along the inner walls of the bifurcation the flow is parallel to the vessel walls and shear stresses are high. The regions of low wall shear stress correlated well with the known tendency of atherosclerotic lesions to form in the carotid sinus, with the inner walls of the bifurcation typically remaining disease-free (Samuel 1956; Solberg and Eggen 1971). This study represented a precursor to current particle image velocimetry (PIV) techniques, which use sophisticated computer algorithms to analyze the particle images.

Color Doppler ultrasound imaging (DUS) provides an additional means to visualize and quantify the flow in models of the carotid bifurcation. In vitro DUS studies of a carotid bifurcation model, (Polak, Oleary et al. 1990) showed regions of flow reversal in the carotid sinus. This corresponds to the region of flow reversal and recirculation observed by flow visualization techniques and LDV. Although most previous in vitro studies have been performed in models of healthy arteries, the flow through a carotid bifurcation model with a 25% stenosis in the sinus has also been investigated (Palmen, Vandevosse et al. 1994; Gijsen, Palmen et al. 1996). Hydrogen bubble visualization, LDV measurements, and corresponding computational flow dynamics CFD analyses showed that this minor stenosis had only a small effect on the flow fields.

The experimental techniques currently available for quantitative analysis in arterial flow models each have their unique strengths and weaknesses. Previous quantitative studies in the carotid bifurcation have mainly used LDV, which provides high spatial and temporal resolution ;10 mm, ;100 kHz!. However, LDV is very tedious when used to map a velocity field, since the velocity can only be measured at a single point at one time. PIV techniques are far more efficient, since the velocity field over an entire plane of the model can be measured

instantaneously. However, PIV has lower spatial and temporal resolutions ~.0.25 mm, and typically 15 Hz; up to 1000 Hz available at prohibitive cost. Both LDV and PIV can only be used in transparent models. DUS and magnetic resonance velocimetry (MRV) both have rather low spatial resolution compared to LDV and PIV ~cf. 3 mm for DUS and 1 mm for MRV. However, DUS and MRV both have the advantage that they can be used in vivo, enabling direct comparison between in vitro and in vivo studies. Modeling or measuring wall and fluid shear stresses is challenging even in healthy blood vessels. Even more daunting is the characterization of shear stresses in the highly irregular lumen of a diseased blood vessel. Currently, no available technique can measure the real time distribution of velocities in vivo, and therefore shear stresses have been, at best, estimated.

2.8 Literature Review Conclusions

A review of literature on numerical and experimental modeling of the cardiovascular system under diseased and non-diseased cases has been presented. For DES modeling, the drug release in the arterial walls via DES, computational arterial hemodynamic studies, and arterial phantoms has been presented. Presently, the majority of DES studies have incorporated reversible binding reactions. The most noteworthy recommendations for DES studies are: (1) incorporating factors related to the pathological conditions; such as plaque, thrombus, and regions of tissue compression, (2) incorporating design optimization studies with reversible reacting mechanisms, and (3) including modeling the coating and finite drug reservoir, the presence of thrombus, or allowing for neighboring or overlapping stents. The latter might require the inclusion of luminal flow in the model to achieve the correct delivery patterns.

For arterial phantom studies, future studies need to capture the effects of local hemodynamics on global hemodynamics. In the case of computational arterial hemodynamic

studies, although the studies based on 2-D models have revealed some key features in fluid-structure interaction, there is a need nonetheless to develop three-dimensional models to define the physiognomies that only occur in realistic systems. Three-dimensional models can provide insight on realistic issues that occur in blood flow in the arterial network such as non-axisymmetric buckling of the tube and secondary flow. There are relatively few theoretical investigations of flow in three-dimensional collapsible tubes. The next chapter presents the methodology of the present study.

CHAPTER 3

Methodology

In Chapter 3, the measuring tools, flow loop components, design requirements, and calibration techniques developed and used in the present study are discussed. It is important to know what a measuring tool cannot do as well as what it can do before a final selection is made. Each measuring tool has advantages and disadvantages, and the degree of performance is directly related to how well a measuring tool's capabilities and shortcomings are matched to the working environment and application. A thorough explanation of the selection of each measuring tool is provided in addition to decision matrices which were developed and used as a down selecting tool in the design process. The design requirements for the cardiovascular phantom developed for the present study is presented. The process developed for designing and calibrating the phantom flow loop is also presented. The next section presents a discussion on the design requirements and design processes of the pulse duplicator and cardiovascular phantom.

3.1 Cardiovascular Phantom CAD Model Development

In the present study, an experimental cardiovascular phantom consisting of the major arteries that deliver blood from the heart to the head and feet is presented. The schematic presented in Figure 3.1a provides an overview of the major arteries that are modeled in the cardiovascular phantom. The schematic in Figure 3.1b is a CAD model schematic of the cardiovascular phantom which was created in Solidworks. The CAD schematic was used to create the mold for fabricating the phantom. The CAD model presented in Figure 3.1b was also used as a geometry mesh for the digital cardiovascular phantom used for CFD simulations which are presented later in Chapter 4 (specific objective 2).

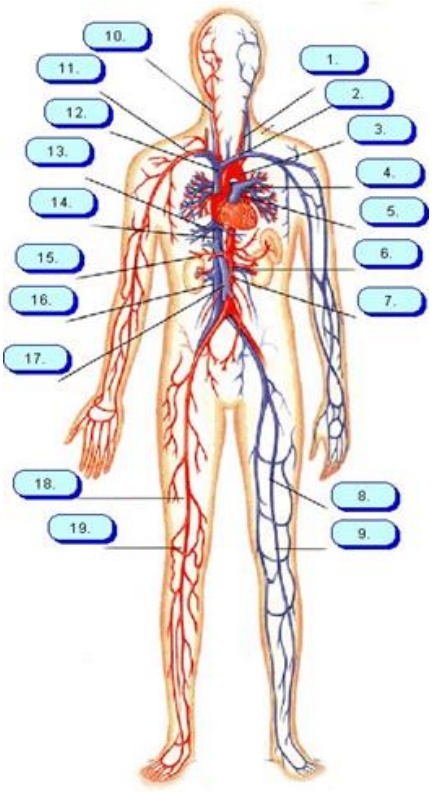

1. Jugular vein
2. Subclavian vein
3. Aorta
4. Pulmonary artery
5. Pulmonary veins
6. Renal artery
7. Mesenteric artery
8. Femoral vein
9. Popliteal vein
10. Carotid artery
11. Subclavian artery
12. Superior vena cava
13. Hepatic vein
14. Inferior vena cava
15. Hepatic artery
16. Renal vein
17. Hepatic Portal vein
18. Femoral artery
19. Popliteal artery
20. Jejunal artery
21. Coronary artery
22. Cranial artery

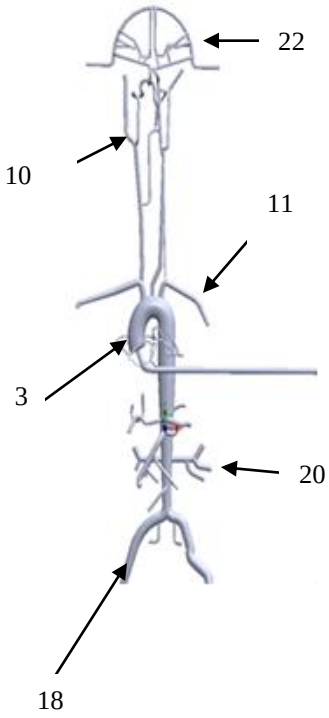

(a) **(b)**

Figure 3.1. Full cardiovascular system: (a) schematic representation of arterial system, and (b) Cardiovascular phantom CAD model.

The CAD model was created from patient-specific CTA scans. A Matlab code was written to upload the CTA scans of each artery, calculate the centroids, and produce surface splines at each discrete cross section along the lumen centerline to create the solid geometry. The process of generating the CAD model is described in more detail below:

1. Import the point cloud CTA image.
2. Calculate the centroids of the arterial fluid core (lumen) contours.
3. Translate the data so the fluid core is centered at the origin of the coordinate axes.

4. Estimate the centerline of the fluid core.
5. Rotate the data so that the centerline is aligned with coordinate axis.
6. Calculate the hydraulic diameter of the inlet.
7. Create surface splines at each cross section along the centroids.
8. Create a flow extension to ensure fully developed flow.
9. Export the new coordinates for the lumen cross section to Solidworks.
10. Unite the surface splines using the boundary boss base feature.

To align the fluid core with the x-axis, an estimate of the centerline had to be made. This was accomplished using cubic spline interpolation. The cubic spline produces a smooth continuous curve. Matlab contains in-built functions for implementing cubic splines, however the cubic spline method is described below.

$$S_i = a_i + b_i(\hat{x} - x_i) + c_i(\hat{x} - x_i)^2 + d_i(\hat{x} - x_i)^3 \quad \text{for } x \in [x_i, x_i + 1] \qquad \text{Eqn. 3.1}$$

For a spline with "n" centroids, there are n-1 cubic polynomials that have a total of 4n-4 unknowns. Continuously constraints account for 2n-2 unknowns:

$$S_i(x_i) = a_i \qquad \text{Eqn. 3.2a}$$

$$S_i(x_{i+1}) = S_i(x_i + 1) = a_{i+1} \qquad \text{Eqn. 3.2b}$$

smoothness in the first and second derivatives for the interior curves account or another 2n-4 unknowns:

$$S'_{i+1}(x_{i+1}) = S'_{i+1}(x_{i+1}) \qquad \text{Eqn. 3.3a}$$

$$S''_{i+1}(x_{i+1}) = S''_{i+1}(x_{i+1}) \qquad \text{Eqn. 3.3b}$$

The last two constraints are handled in Matlab with the "Not-a-Knot" constraint. This constraint is applied at the first two or last two cubic curves and matches the third derivatives of the paired

polynomials:

$$S'''_1(x_2) = S''2(x_2) \quad \text{Eqn. 3.4a}$$

$$S''_{n-2}(x_{n-2}) = S''_{n-2}(x_{n-2}) \quad \text{Eqn. 3.4b}$$

with the estimate of the centerline calculated, the geometry data can be rotated to align the fluid core with the x-axis. To rotate the geometry data a rotation matrix had to be constructed. Equation 3.5 is a generalized rotation matrix:

$$R = \begin{bmatrix} u_1^2 + (1-u_1^2)c & u_1u_2(1-c) - u_3s & u_1u_3(1-c) + u_2s \\ u_1u_2(1-c) + u_3s & u_2^2(1-u_2^2)c & u_2u_3(1-c) + u_1s \\ u_1u_3(1-c) - u_2s & u_2u_3(1-c) - u_1s & u_3^2 + (1-u_3^2)c \end{bmatrix} \quad \text{Eqn. 3.5}$$

where

$$c = \cos\theta \quad \text{Eqn. 3.6a}$$

$$s = \sin\theta \quad \text{Eqn. 3.6b}$$

and $u = (u_1, u_2, u_3)$ is the axis of rotation and θ is the angle of rotation. In the case of aligning the fluid core with the x-axis, u is determined by the cross product between the slope of the centerline estimate at the first contour, $\vec{n}$, and the unit vector along the x-axis, $\vec{x}$. The angle is determined by using the four-quadrant inverse tangent, atan2 function. This allows for accurate calculation of the angle of rotation even when the two vectors are nearly parallel.

The coordinates of the points from the original CTA point cloud images were defined on a cartersian coordinate system set far from the origin. The contours were translated and rotated

to have the first contour of the fluid core centered on the origin and the centerlines of the geometry were estimated to allow the fluid core inlet to be aligned to the x-axis. The hydraulic diameter of the fluid core was calculated to create the flow extension to ensure fully developed flow. This also allows the application of an unsteady inlet boundary condition. The hydraulic diameter is defined in Equation 3.7.

$$D_h = \frac{4A}{P} \qquad \text{Eqn. 3.7}$$

where A is the cross-sectional area and P is the wetted perimeter. The flow extensions are 0.06 times the systolic Reynolds number in length. The method of calculating the Reynolds number is provided in Eqn. 3.8.

$$\mathrm{Re} = \frac{\rho V D}{\mu} \qquad \text{Eqn. 3.8}$$

The entrance length was chosen to allow for a smooth transition to the irregular cross-section of the arterial lumen during the lofting process and to allow the diffusion of the viscosity. The flow extensions also allow the flow to develop to the patient-specific geometry. The lofting process was completed in Solidworks. The cross-sectional contours along the centerline of the model were united using the boundary boss base feature. The solid CAD model was used to create a mold for the cardiovascular phantom. The CAD model was also used for the digital cardiovascular phantom for CFD simulations. For CFD studies the digital cardiovascular phantom was looped such that the phantom had only one inlet and one outlet. The boundary condition for the inlet was an unsteady velocity profile specified by a user defined function (udf). The user defined function was used for both regular flow and dye trace studies. The next section presents the cardiovascular phantom design fabrication process.

3.2 Cardiovascular Phantom Design Fabrication Process

The design criteria of the phantom and pulse duplicator that was used in the design process are listed. The experimental cardiovascular phantom should:

1. Be made from a material that can mimic the compliance of the arteries.
2. Be made from a material that allows flow visualization for dye transport and physiological Peclet numbers.
3. Instrumented such that physiological parameters (flow rate, pressure, wall shear stress, and normal stress) can be determined.

The pulse duplicator should:

1. Be capable of producing simplified and patient-specific volumetric waveforms.
2. Be capable of performing user defined physiological parameters (temperature, pressure limits, volumetric waveform, and frequency)
3. Measuring diagnostic parameters.

The material used to construct the arterial vessels is a clear silicone material that matches the elasticity of human arteries and is optically transparent for flow visualization. The CAD model was sent to United Biologics for processing. United Biologics used a lost casting technique to produce the cardiovascular phantom for the present study. A picture of the cardiovascular phantom prior to connecting to the pulse duplicator, flow measuring devices, compliance chamber is presented in Figure 3.2. A decision matrix that was used to select the pulse duplicator for the present study is presented in Table 3.1.

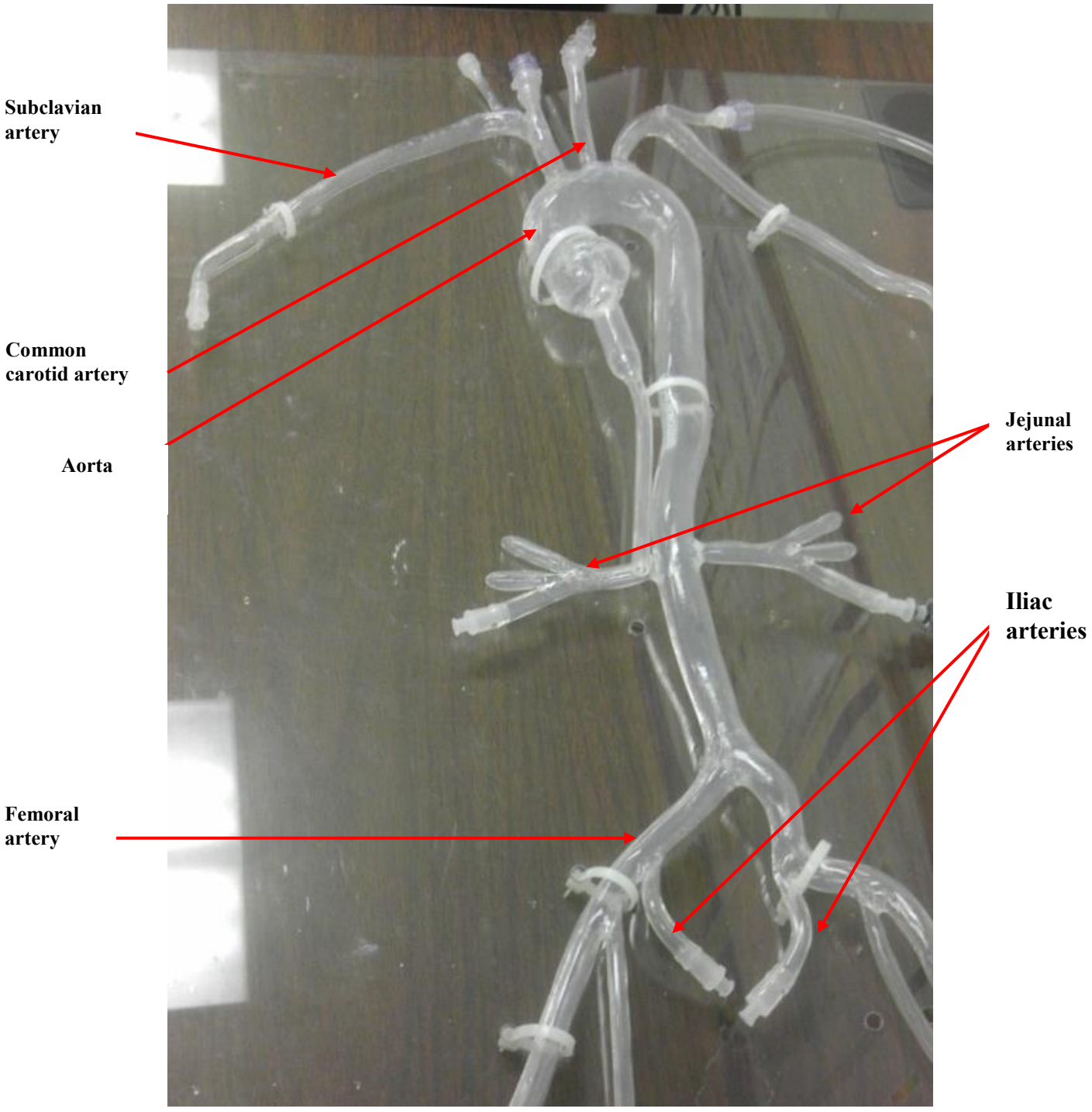

Figure 3.2. Cardiovascular phantom prior to looping with components.

Table 3.1

Pulse duplicator decision matrix.

Criteria	Weight %	Pulse Duplicator		
		1 United Biologics	2 Harvard Apparatus	3 BDC Labs
Accuracy	35	25 35	5 35	20 35
Functionality	25	30 25	15 25	40 25
Ease of Use	25	15 25	25 25	15 25
Cost	15	5 15	10 15	5 15
Total	100	75	55	80

The pulse duplicator that was used in the present study is a custom made BDC Labs pulse duplicator. In the present work, the pulse duplicator acts as the pumping heart; therefore with the pulse duplicator and the appropriate components, the local hemodynamics of the major arteries and vascular bed within the arterial system can be simulated. The pulse duplicator used in the present study is capable of producing physiological data and allowing more user defined functionality than previous studies have. The pulse duplicator is capable of producing simplified and patient-specific aortic volumetric waveforms for rest-state and exercise conditions. The maximum systolic volumetric waveform for the present study is 17 L/min. The pulse duplicator is also capable of producing user defined volumetric waveforms with the capabilities of adding on harmonic terms for the input waveform. The pulse duplicator is programmable for controlling the temperature of the working fluid, the frequency of the flow (heart rate), volumetric flow rate, pressure limits and stroke volume. The pulse duplicator has its own data acquisition software for monitoring real time volumetric flow rate and pressure during experimental runs. The data acquisition software also contains analysis capabilities that allow the user to analyze waveforms using techniques such as Fast Fourier Transform of output waveforms and signal analysis.

In addition to producing user defined volumetric waveforms, the pulse duplicator has its own in-built compliance chamber for allowing the user to control the compliance of the system. The pulse duplicator is a highly repeatable and a controllable pulsatile pump. A picture of the data acquisition used for the pulse duplicator is provided in Figure 3.4. The next section presents the flow meter and pressure measuring devices that were considered for the present study and the devices that were chosen.

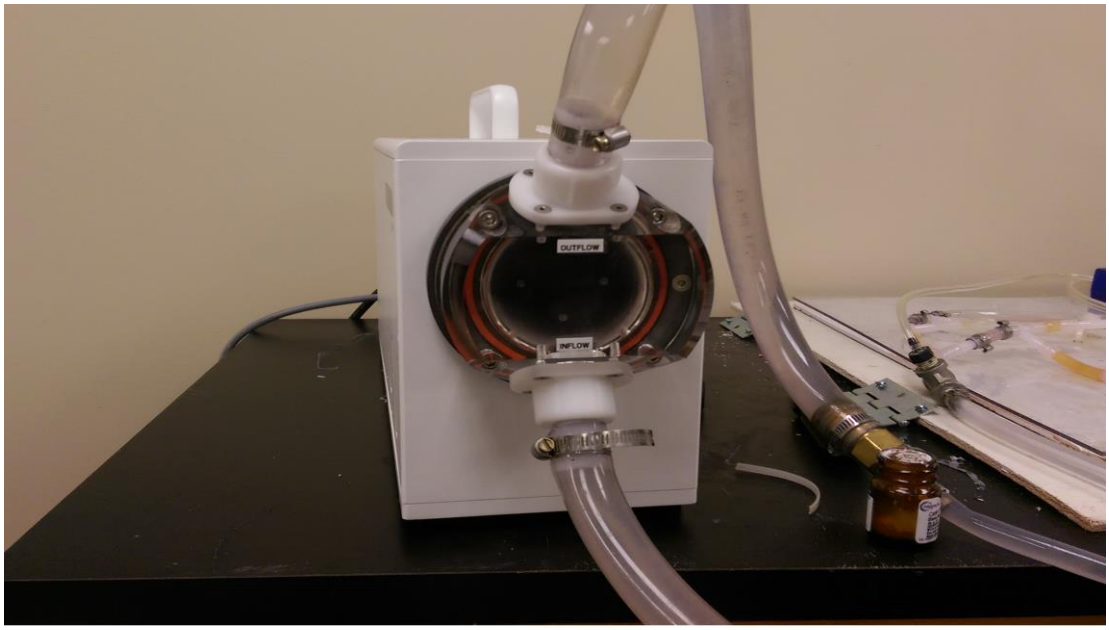

(a)

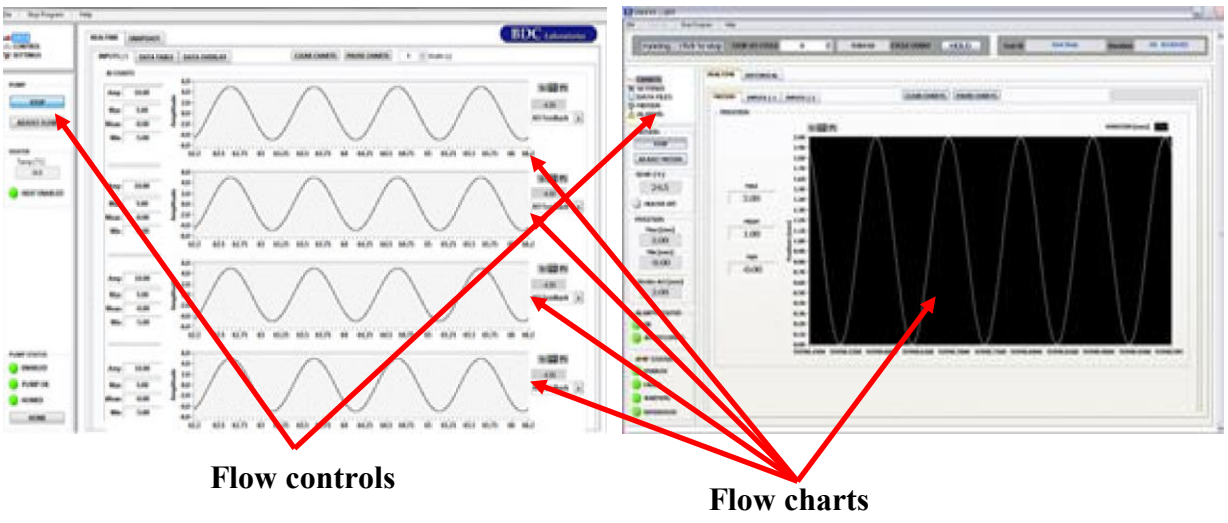

(b)

Figure 3.3. Photograph of: (a) pulse duplicator, and (b) screenshot of pulse duplicator data acquisition software.

3.3 Flow Meter and Pressure Measuring Device Types Considered

The first flow measuring device that was selected for the present study was a flow meter. There are a variety of methods available to measure volumetric flow rate. Table 3.2 provides a list of commonly used flow meter device types that are used in flow applications. Table 3.3 presents the decision matrix that was developed and used as the down selecting tool for the flow meter device type selection process. From the decision matrix listed in Table 3.3, a restriction flow metering device was deemed to be the most suitable choice for the present study. The following presents a discussion on the reason why the alternative choices were not used:

Table 3.2

Flow meter device types and specifications.

Mechanism	**Nominal Accuracy***	**Flow-sensitive or summing element**	**Operating Range**
Restriction flow meters	Dependent on the differential pressure device	Nozzle type opening	4:1 Range
Linear flow meters	0.05	Float type, turbine, vortex, and electromagnetic	0.25-160 L/min
Traversing Methods	0.2	Thermal anemometers	0.38-1000 L/min

Restriction flow meters for internal flow are based on acceleration of a fluid stream through a diverging area in which the differential pressure is measured using a pressure measuring instrument. The flow rate can then be inferred using a theoretical analysis or an experimental correlation device. The most popular restriction flow metering devices are orifice and Venturi meters. An orifice meter consists of an orifice plate with a machined hole in the center. The orifice plate is positioned between two straight pipes in length, usually flanged. When the fluid enters the orifice, it must accelerate due to the flow area being reduced.

Table 3.3

Flow measuring device decision matrix.

Criteria	Weight %	Flow Measuring Devices		
		1 SM600	2 F1250	3 Pasco
Accuracy	35	15 35	15 35	15 35
Functionality	25	15 25	15 25	25 25
Ease of Use	25	19 25	15 25	25 25
Cost	15	10 15	10 15	11 15
Total	100	59	55	76

The Bernoulli's equation describes the corresponding pressure drop that takes place and is also used to correlate the theoretical mass flow rate. An orifice meter was not used because a manufactured orifice meter requires at least 12 feet (3.658 m) of piping from the pipe connection

adapters to achieve the correct pressure drop to correlate a flow rate reading. As a result, the orifice meter is not space accommodating. The Venturi meter consists of a conical entrance and exit section connected by a reduced cross section area in length. The reduced area section is recognized as the throat of the Venturi.

Similar to the orifice meter, the Venturi meter is also based on the reduction of flow pressure accompanied by an increase in velocity. The pressure drop experienced is used to measure the rate of flow through the Venturi meter. On the discharge side of the meter, the fluid velocity is decreased and the original pressure is recovered. Because of the shape of the Venturi element, the pressure losses in a Venturi meter are less than in an orifice meter. The derivation and clarification of the correlation between theoretical mass flow rate and pressure drop can be found in (Fox R. 2004). A Venturi meter was not used because a Venturi meter requires molding and casting of the Venturi element. Hot-wire anemometers is another method used for measuring flow rate and is a traversing method. Hot-wire anemometers were not considered because the phantom material is sensitive to heat transfer and will deform and break under extensive heat.

From the decision matrix listed in Table 3.3, a Pasco Spark data acquisition system, with single pressure and differential pressure measuring and data capturing capabilities were chosen. The Pasco system was used to measure pressure at a point and to measure the volumetric flow rate of the pulsatile flow via differential pressure. An in-house wedge flow meter that was constructed from a PVC pipe was used in conjunction with the pasco pressure measuring device. The wedge flow meter element operates based on differential pressure. The spark system is factory calibrated to infer a volumetric flow rate reading based on differential pressure for flow metering elements. The second flow metering device is pulse duplicator itself which contains an

inbuilt flow meter. The cardiovascular phantom was connected to a fluid flow loop which consisted of a compliance chamber/fluid reservoir, pulse duplicator, two pressure meters (head and feet), and a flow meter. A Tilt table was also installed to test the phantom during transition from bed-rest to upright position. Figure 3.4 shows the phantom connected to the loop.

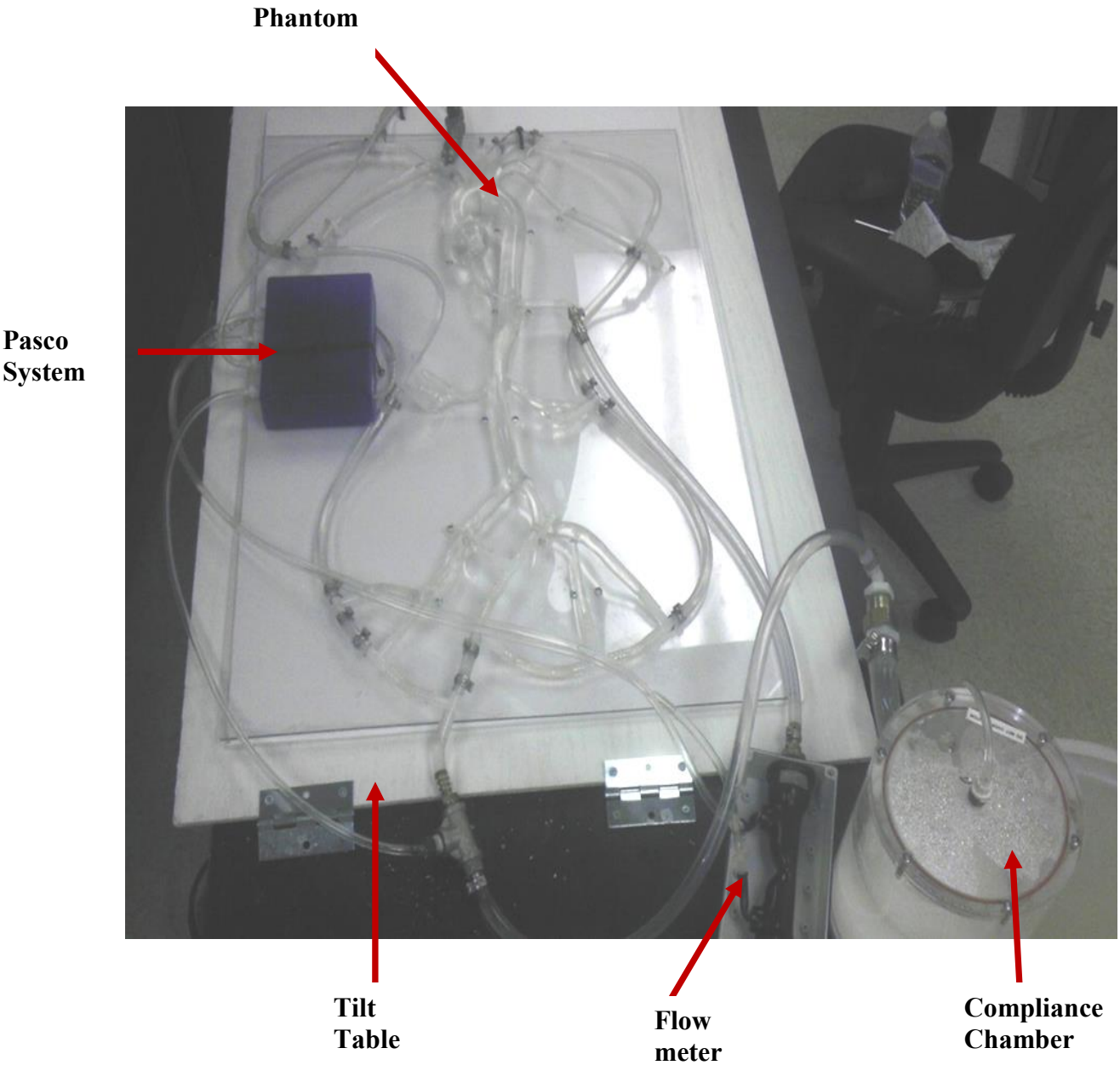

Figure 3.4. Photograph of cardiovascular phantom with looped components and tilt table.

3.4 Design of In-house Particle Imaging Velocimetry System

An in-house PIV system was designed and built for the present study. As mentioned earlier in Chapter 3, PIV consists of capturing images of small spherical hollow glass particulates moving with the flow field. The images are processed using software to determine information on the flow such as flow patterns, flow trajectory, and flow parametric data. The in-house PIV system used in the present study consisted of two high speed Basler acA2040-180 km CMOS cameras in conjunction with a PIXC1-E8 frame grabber (Epix, Inc.) which captured images of the particulates moving with the pulsatile flow field. Navitar NMV-35M1 lenses are used, which have an effective focal length (EFL) of 35 mm. The lenses have a minimum *f*-number of 1.4. The frame grabber is a Camera Link frame grabber that is able to capture the camera frame rate sequence using 1.4 Gbyte/sec burst transfer. The frame grabber is housed in an IBM Desktop computer with a PCI Express x8 79 bus slot and 512 MB of memory. The sensor and frame grabber was controlled using XCAP-Std software (Epix, Inc.) which allowed for sequence capture and manipulation of images.

The pulsatile flow field is illuminated by creating a laser light sheet using a MGH-H-532, solid-state green laser (Opto Engine) with a power output of 1.4 W. A 60° lens is attached to the laser as a line generator to create the light sheet. The laser was operated at a wavelength of 532 nm which was capable of producing a 1.5 mm thick. Figure 3.5 provides a photograph of the PIV system setup with the laser and cameras. The in-house PIV system uses open-source PIV processing software called PIVlab_1.32. The code uses time-resolved PIV to pair images and calculates the velocity distribution. The code is also able to derive, display, and export many other parameters of the flow field.

(a)

(b)

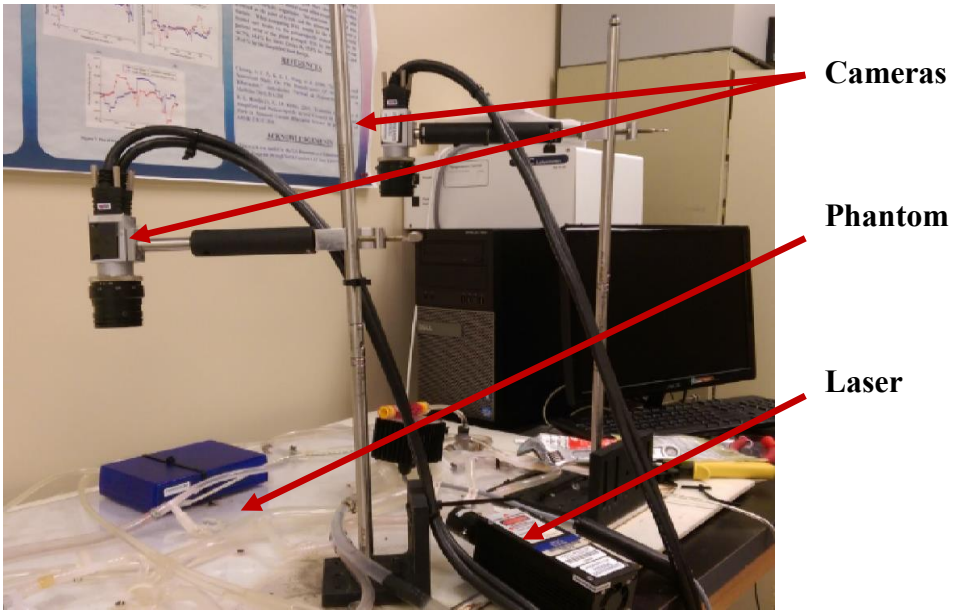

(c)

Figure 3.5. Photograph of PIV system (a) and (b) laser and (c) system setup.

Images can be analyzed using either Fast Fourier Transform (FFT) or direct cross correlation (DCC). For the present study the direct cross correlation technique is used for all analyses. Prior

to conducting any PIV analyses, the PIV system had to be calibrated to insure accurate measurements. The system was calibrated via gravity driven flow and Womersley flow (pulsatile flow). Analytical results were compared to experiments and were found to be within 3% agreement. The next section presents the gravity driven flow PIV calibration methodology and results.

3.4.1 Gravity Driven Flow PIV Calibration

For gravity-driven calibration, a simple, gravity-driven pipe flow problem was setup to test the accuracy of the system. Figure 3.6 shows a CAD schematic of the pipe flow experimental setup. A cylindrical polycarbonate tube (test tube) was used for testing. The outer diameter was 0.19m, inner diameter 0.016m and the length of the pipe was 0.61 m. The test tube was constructed so that the fluid was discharged through a circular orifice, 3.57 mm (9/64") in diameter. A constant pressure head was maintained to ensure a constant volumetric flow rate. A beaker was used to capture the fluid and a mass balance and stop watch was used to measure the mass of the fluid as a function of time to infer a volumetric flow rate measurement. For comparing the PIV results to the analytical solution of gravity-driven pipe flow, the solution had to be derived from the Navier Stokes equation. A simple explanation of the solution is provided here. Assuming one-dimensional (1D) flow, with gravity as the driving force, the parabolic velocity profile (analytical solution) can be obtained from:

$$u_z(r) = \frac{\rho g R^2}{4\mu}\left(1 - \frac{r^2}{R^2}\right)$$

Eqn. 3.9

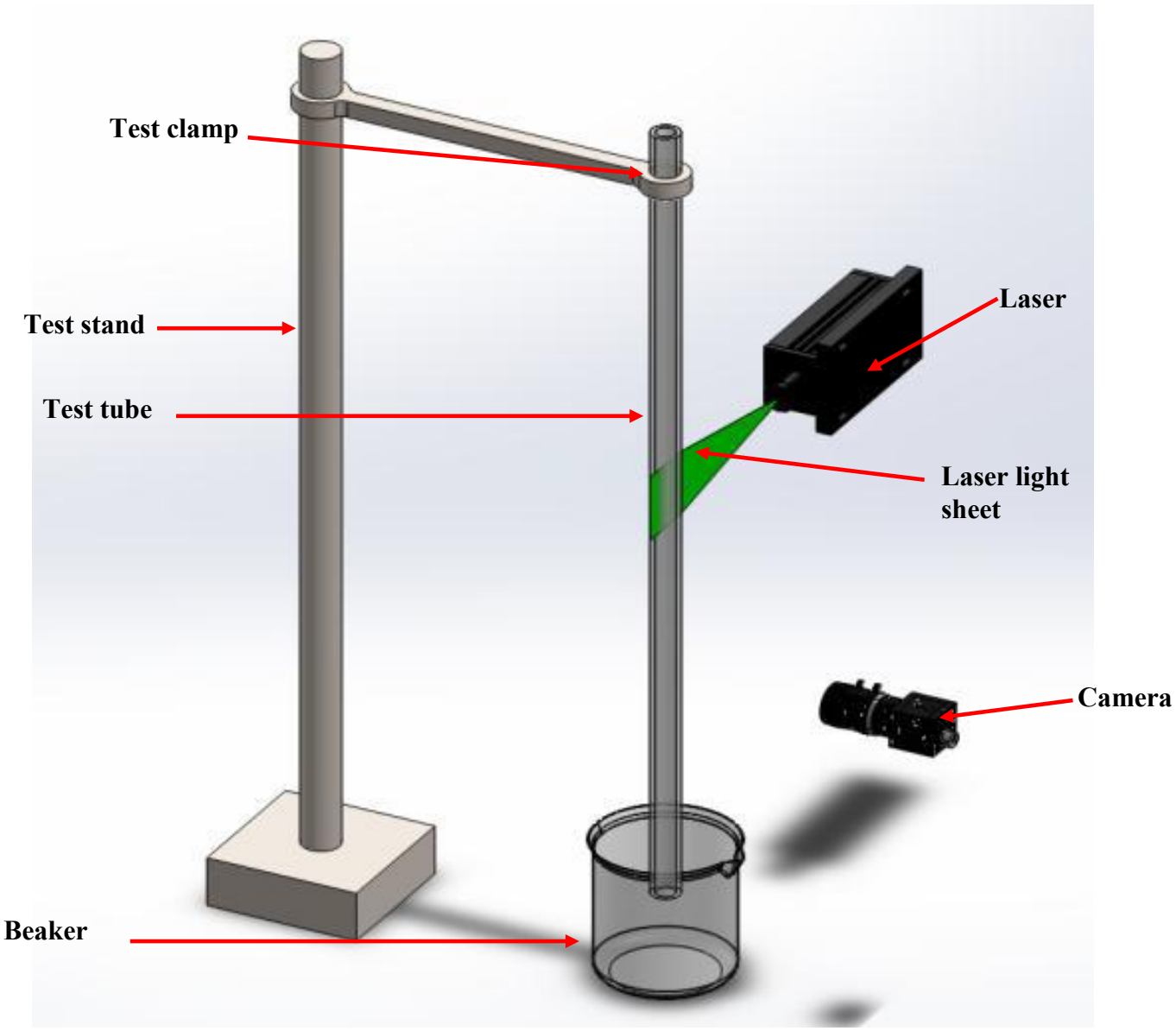

Figure 3.6. CAD Schematic of gravity-driven calibration setup.

The volumetric flow rate is obtained from the following:

$$Q = \int \vec{v} \cdot d\vec{A} = \int_0^R u_z(r) \cdot 2\pi r dr = \frac{\rho g \pi R^4}{8\mu} \qquad \text{Eqn. 3.10}$$

the average velocity V_{ag} is given as:

$$V_{avg} = \frac{Q}{A} = \frac{Q}{\pi R^2} \qquad \text{Eqn. 3.11}$$

the point of maximum velocity is found to be at r = 0, or at the centerline of the pipe. Therefore, the maximum velocity is given as:

$$V_{max} = 2\vec{V} \qquad \text{Eqn. 3.12}$$

The volumetric flow rate in the pipe is equal to the flow rate exiting the orifice due to continuity. So the velocity in the pipe can be determined. Prior to analyzing results, an interrogation window and grid step independent study was conducted. Table 3.4 shows the increments of pixel and step sizes used. The interrogation/grid step sizes were changed in increments of 10 pixels. The results were shown to be independent of interrogation area at 64 pixels and 32 pixels for grid steps sizes.

Table 3.4

PIV Interrogation Grid Independent Study.

Interrogation area [px]	**Grid (step) size [px]**	**Algorithm**	**Centerline Velocity (m/s)**
44	12	DCC	0.160
54	22	DCC	0.175
64	32	DCC	0.180
74	42	DCC	0.180

Figures 3.7a and 3.7b show the images that were processed in PIVlab_1.32. Figure 3.7a is the first of a series of images that were deployed to be analyzed and b is the resultant vector plot. Figure 3.7a shows the PIV results and analytical solution of the gravity driven pipe flow. Figure 3.7c displays the contour and vector plot of the measured velocity, which shows the parabolic nature of the velocity flow field. The parabolic shaped profile is observed from the Poiseuille

flow problem and is evident in the results. Figure 3.8 shows the comparison of the analytical and the experimental solution. The results are within 3 percent agreement. From Figure 3.8, it is shown that the largest contribution to error is at the wall were the reflection of the laser light distorts the image. However the no-slip condition is known to take place at the wall of the tube and rectifies this error and the error can be minimized at the wall by using vector smoothing.

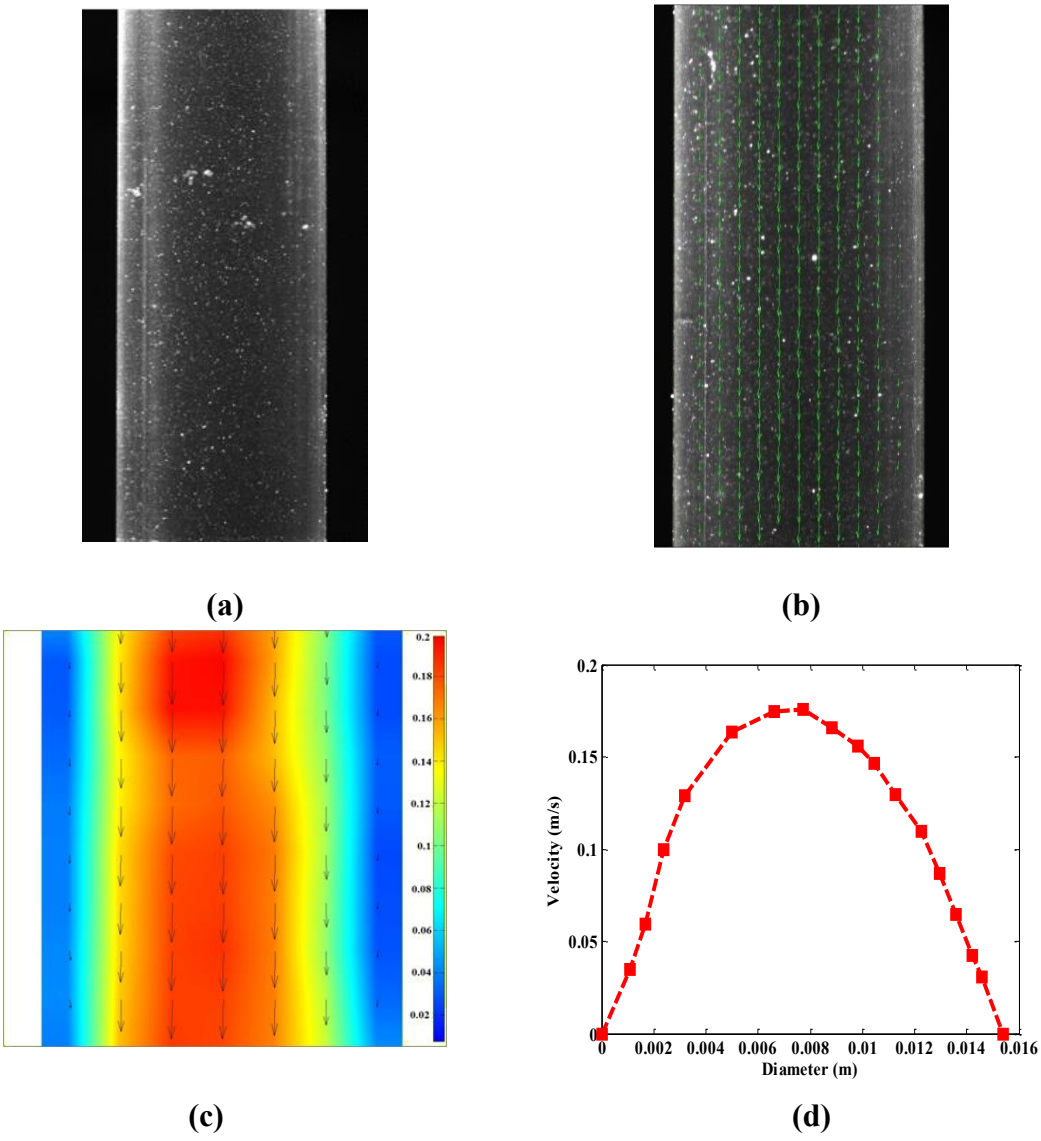

Figure 3.7. PIV Processing methodology

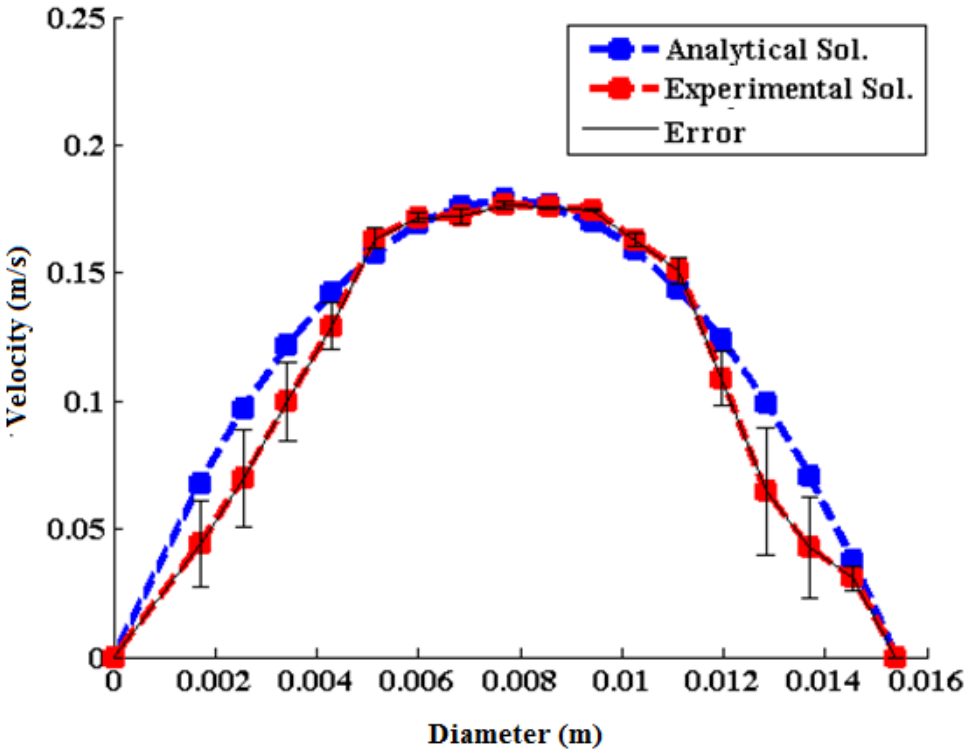

Figure 3.8. Calibration plot of gravity-driven flow with analytical and experimental solution.

3.4.2 Womersley Flow PIV Calibration

For comparing the PIV results to the analytical solution of Womersley flow, the solution had to be derived from the Navier Stokes equation in cylindrical coordinates. A simple explanation of the solution is provided here. The flow is assumed to be 1-D flow, with an oscillating pressure gradient. The oscillating pressure gradient is given as:

$$\frac{\partial P}{\partial z} = \mathrm{Re}\left[\sum_{n=0}^{\infty} a_n e^{j\varpi nt}\right] \qquad \text{Eqn. 3.13}$$

where n is the number of harmonics, a_n is the amplitude, j is an imaginary number, n is the number of harmonics, and ω is the frequency. With the oscillating pressure gradient as the

driving force and through much manipulation, the velocity profile (analytical solution) can be written as a harmonic series equation as a function of radius and time:

$$u(r,t) = u_o(r) + \sum_{n=1}^{\infty} u_n(r,t) \qquad \text{Eqn. 3.14}$$

where

$$u_n(r.t) = \mathrm{Re}\left[\frac{a_n}{j\rho\omega n} \left[\frac{J_o\left(\sqrt{\frac{j^3\varpi n}{\nu}} r\right)}{J_o\left(\sqrt{\frac{j^3\varpi n}{\nu}} R\right)} - 1 \right] e^{j\varpi nt} \right] \qquad \text{Eqn. 3.15}$$

the solution applies to the results of each harmonic. To find the velocity as a function of radius r and time t for the entire driving pressure, the steady flow (Pousellie flow) result u_o is added to the results for all harmonics. For the present study shear stress is a major parameter of interest. The shear stress can be found from:

$$\tau(r,t) = \mu \frac{\partial u_o(r)}{\partial r} + \sum_{n=1}^{\infty} \mu \frac{\partial u_n(r,t)}{\partial r} \qquad \text{Eqn. 3.16}$$

To expand the form of the shear stress equation the derivative terms are needed:

$$\frac{\partial u_o}{\partial r} = \frac{a_o}{2\mu} r \qquad \text{Eqn. 3.17}$$

and

$$\frac{\partial u_n}{\partial r} = \mathrm{Re}\left[-\frac{a_n \lambda}{j\rho\varpi n} \left[\frac{J_1(\lambda r)}{J_o(\lambda R)} e^{j\varpi nt} \right] \right] \qquad \text{Eqn. 3.18}$$

Thus, the oscillatory shear stress can be written as:

$$\tau_n = \frac{a_o}{2\mu} r + \sum_{n=1}^{\infty} \mathrm{Re}\left[-\frac{a_n \lambda}{j\rho\varpi n} \left[\frac{J_1(\lambda r)}{J_o(\lambda R)} e^{j\varpi nt} \right] \right] \qquad \text{Eqn. 3.19}$$

For pulsatile experiment calibration, the frequency of the flow was 70 beats per minutes (1.2 hertz), maximum systolic pressure of 90 mmHg, and a maximum flow velocity of 0.45 m/s. Figure 3.9 shows the measured velocity and pressure profile. The velocity and pressure was not measured at the same point. The captured data is for 4 cycles. Figure 3.10 shows the experiment and analytical velocity profiles at different time steps.

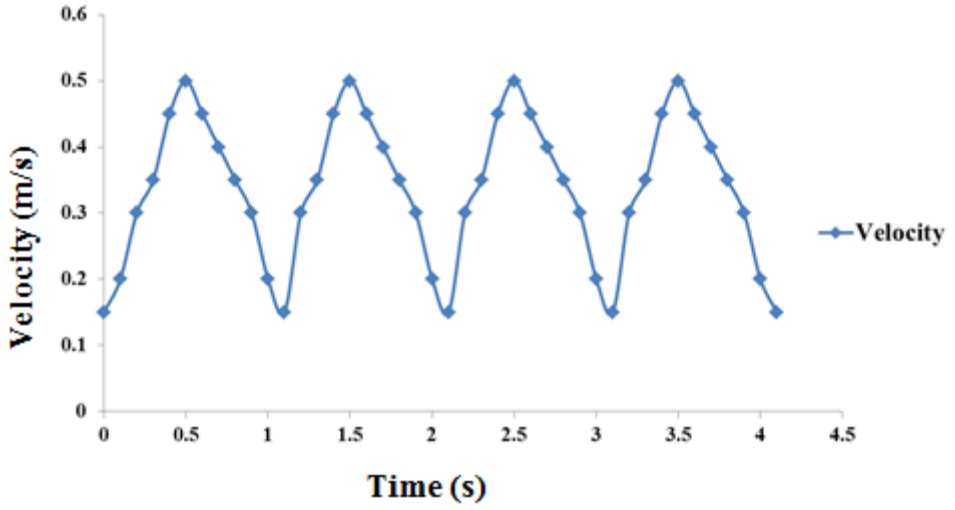

(a)

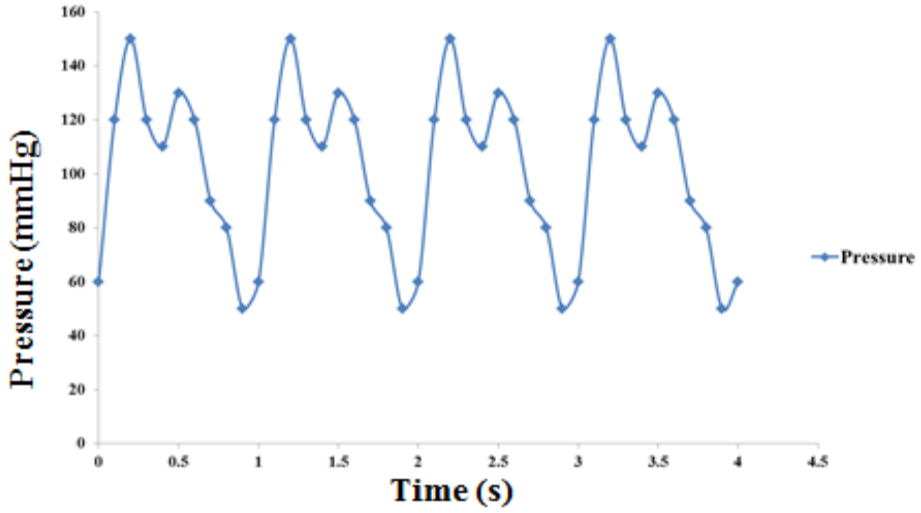

(b)

Figure 3.9. Pulsatile flow experiment waveforms: (a) volumetric flow rate, and (b) Pressure.

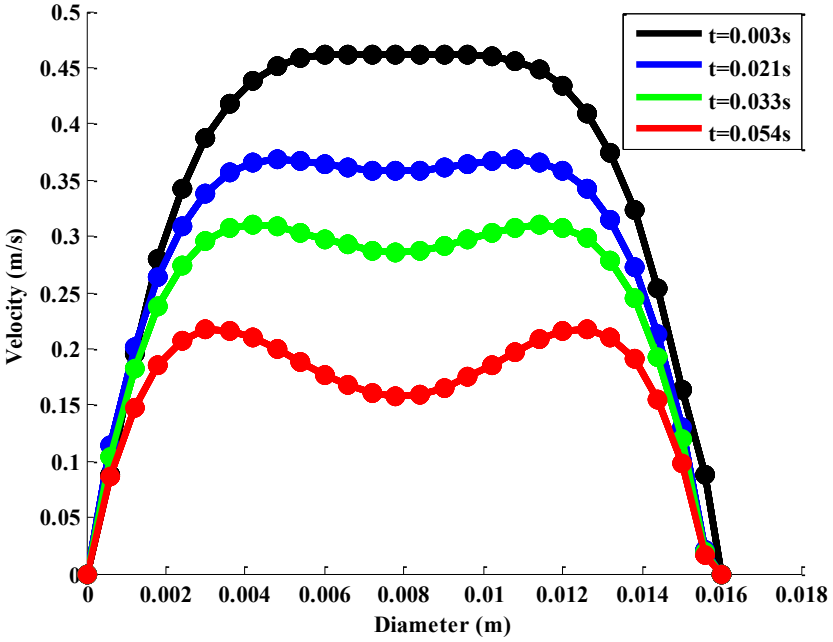

(a)

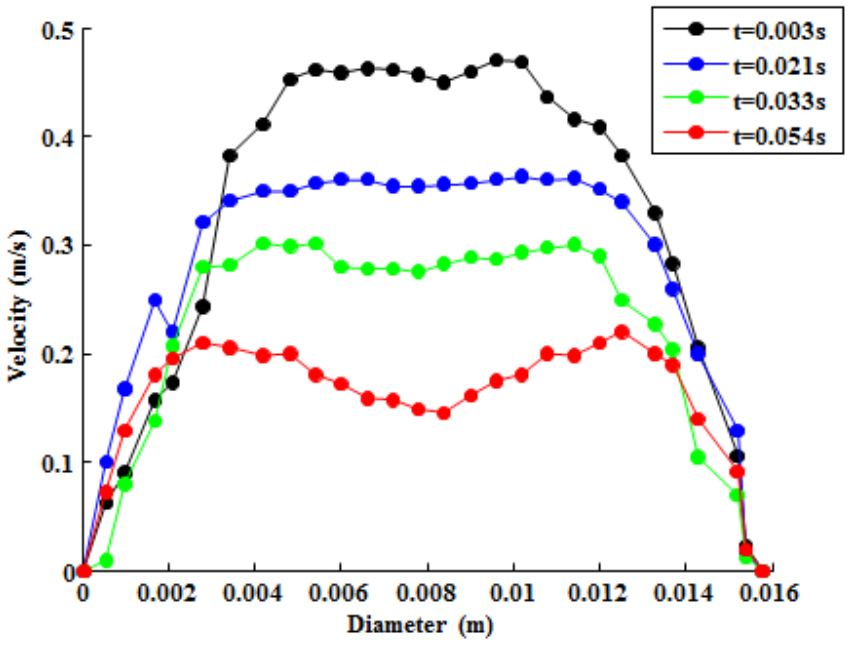

(b)

Figure 3.10. Womersley velocity profiles: (a) analytical and (b) experimental.

The experimental and Womersley velocity profile centerline velocity (maximum velocity) were shown to be within 3 percent difference in error. Similar to the gravity driven results, the maximum error was found to be at the wall. The results shown are for one cross-section along the longitudinal direction (z-direction) of the pipe. A more detailed analysis is needed to determine if the Womersley solution is valid along the longitudinal direction of the pipe. Figure 3.11 shows the PIV contour and vector plots of the velocity profile of the pulsatile flow.

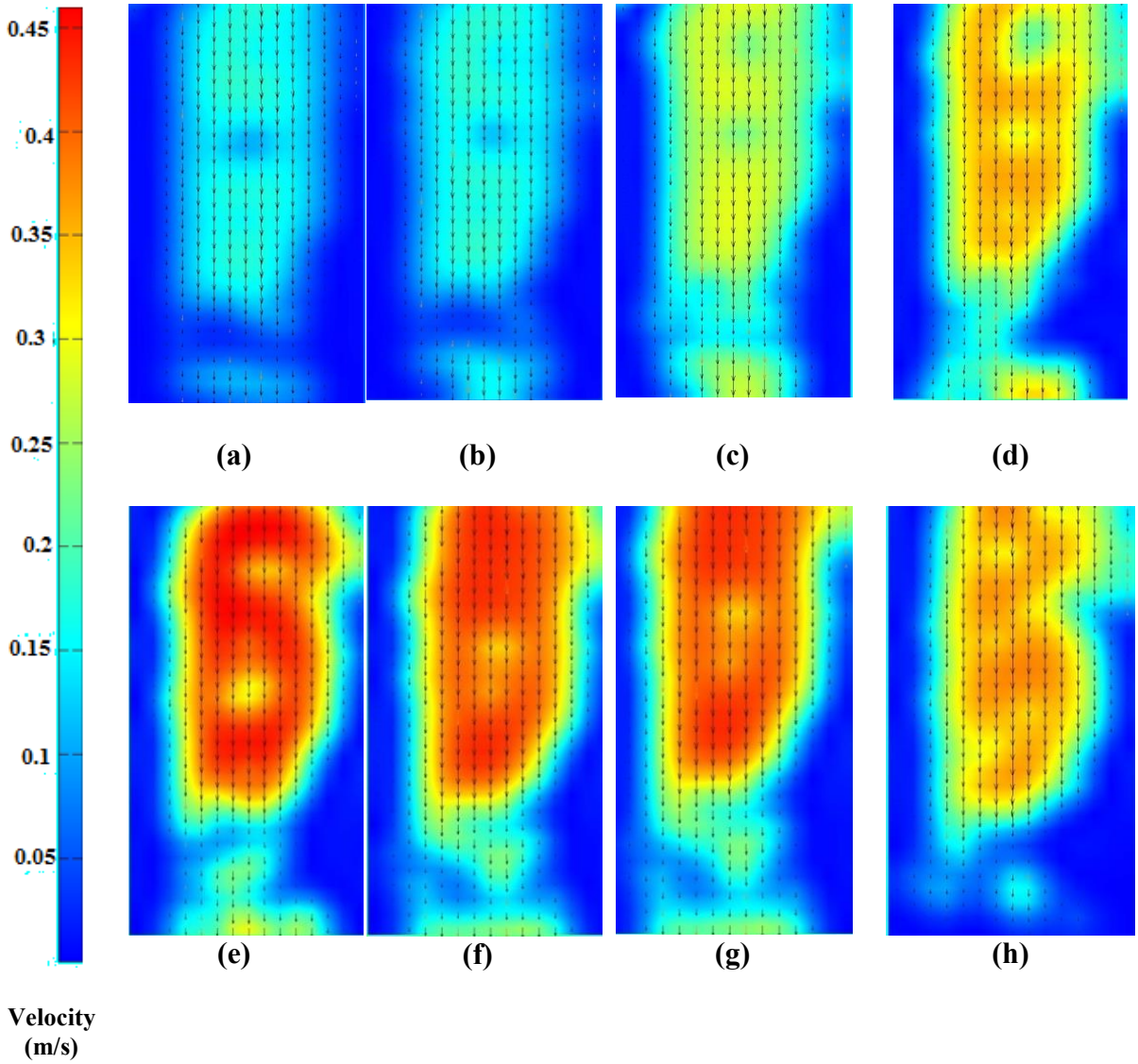

Figure 3.11. PIV velocity contour profiles at: (a) 3.0s, (b) 3.1s, (c) 3.2s, (d) 3.3s, (e) 3.4s, (f) 3.5s, (g) 3.6s, and (h) 3.8s.

The results for each time step shows that the flow is not symmetric along the centerline. For this particular case it is important to introduce the Womersley number. The Womersley number is defined as the ratio of the unsteadiness to viscous. The Womersley number is provided below:

$$\alpha = R\sqrt{\frac{\varpi}{\nu}} \qquad \text{Eqn. 3.20}$$

In the case of Womersley flow, if the Womersley number is large (greater than 10) and R is larger, the flow is dominated by unsteadiness. If the radius of the tube is small, then unsteadiness is not important and the flow is viscous. For the present study, the Womersley number is calculated as:

$$\alpha = (0.008m)\sqrt{\frac{1.2s^{-1}}{0.45\times10^{-6}\,\frac{m^2}{s}}} = 28.22 \qquad \text{Eqn. 3.21}$$

This calculation indicates that unsteadiness is dominant. When unsteadiness is dominant in pulsatile flow, the centerline velocity oscillates out of phase with the pressure gradient. Also, when unsteadiness is present in the system, this means that the velocity profile is not parabolic at each time step in the cycle. In addition, the velocity profile will not be constant at each cross-section along the axial direction of the pipe. In summary, non-symmetric flow will be present in the case of unsteady flow. Figure 3.12 provides contour plots and centerline data for the PIV results. Figure 3.12 provides a clear representation of non-symmetric velocity profile at each discrete time interval. Figures 3.13a 3.13b and 3.13c also show how the velocity at each discrete cross-section along the axial direction of the pipe is not constant. This is due to the unsteadiness of the system in which the Womersley solution cannot be applied. The Womersly solution assumes that the velocity is constant at each cross-section of the pipe along the axial direction.

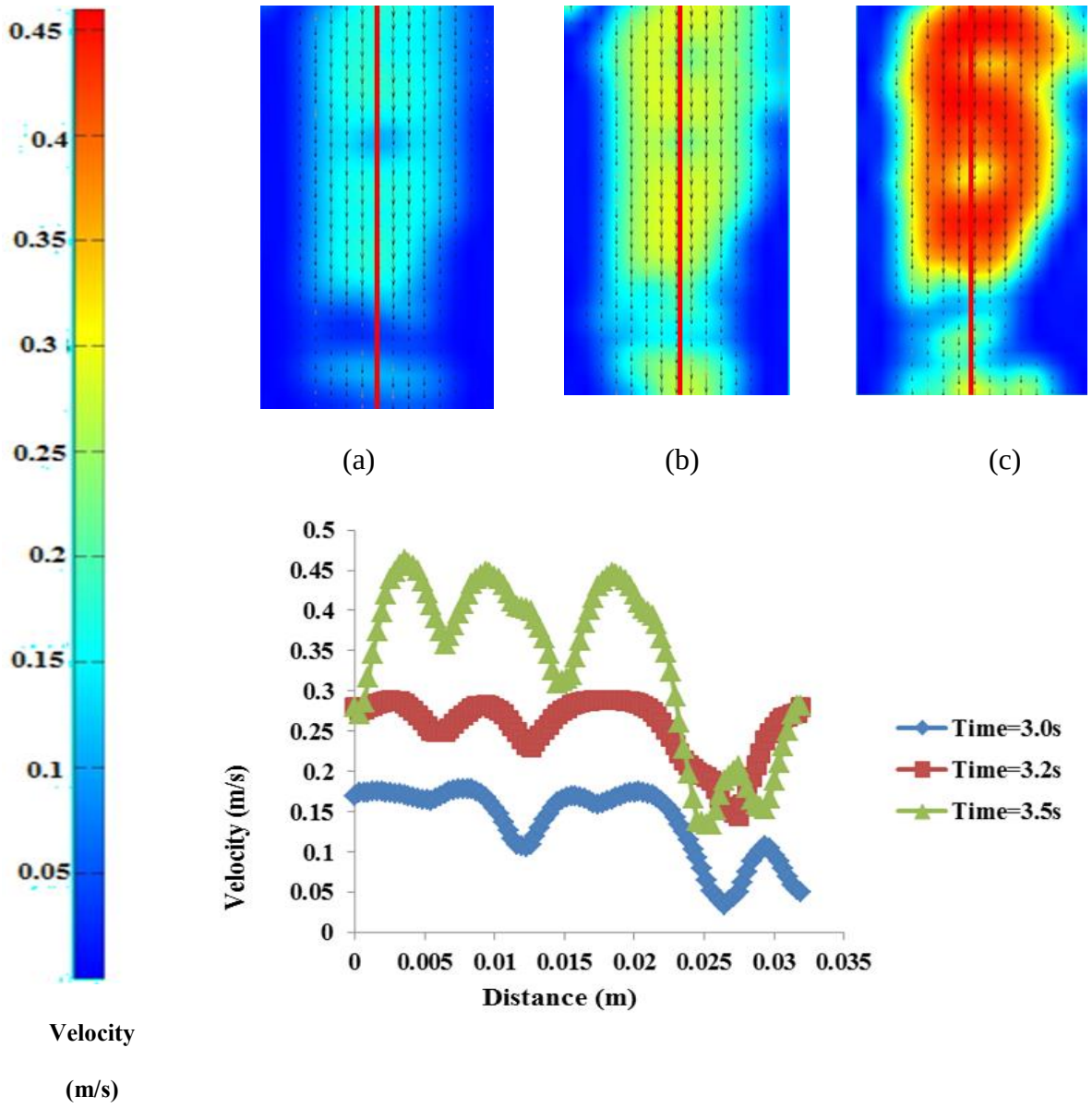

Figure 3.12. Experimental centerline velocity profile.

From the results shown in Figure 3.12e, at times 3.0 and 3.2 the results change in magnitudes slightly and maintain the same trend in profile. However at time 3.5, the profile changes due to the increase in velocity magnitude. From these results it is evident that the

Wormersley solution is only valid for small Womersley numbers or viscous flows. This because of the unsteadiness introduced into the flow by the harmonics of the waveform.

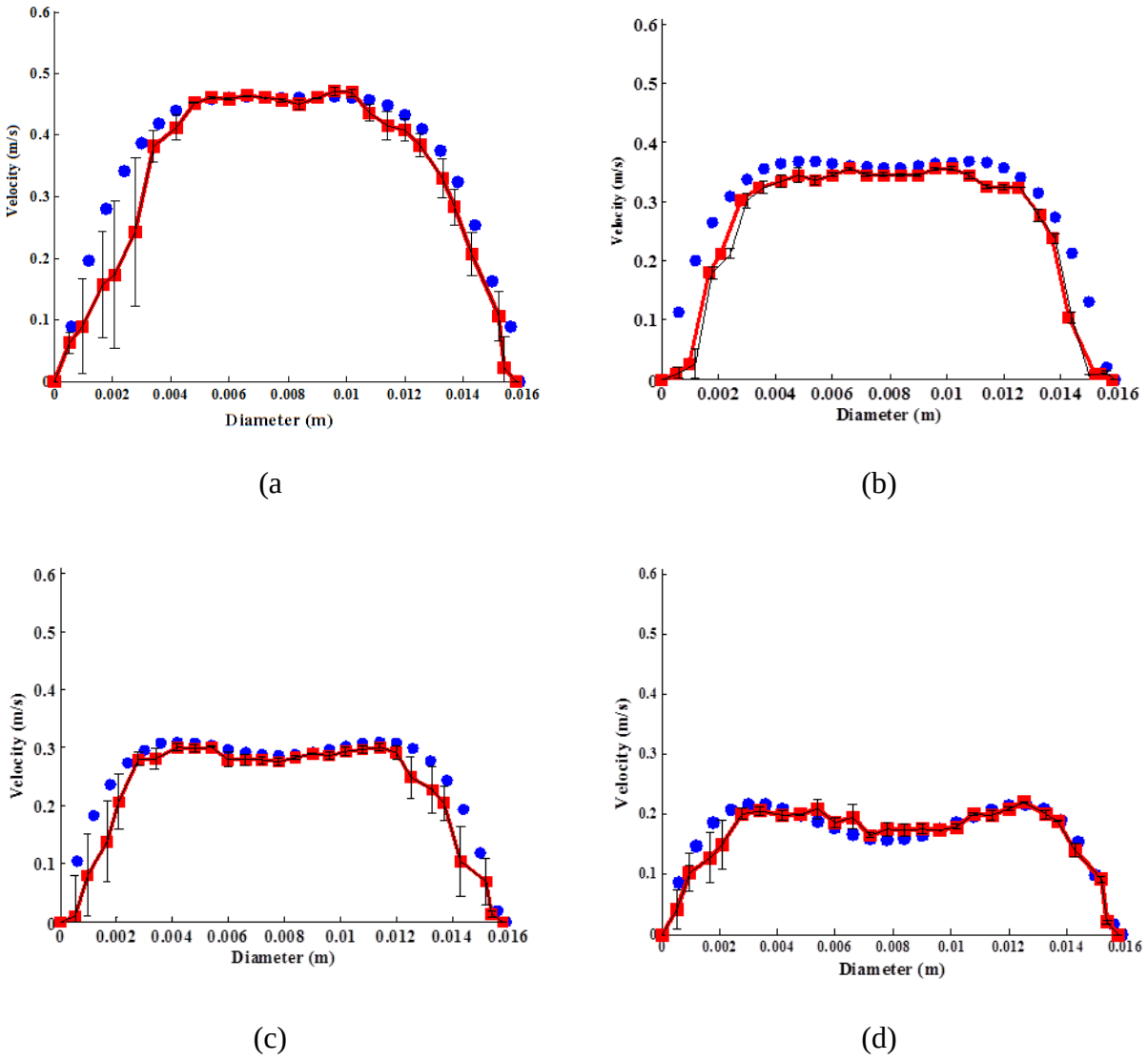

Figure 3.13. Experimental and computational velocity profile comparisons at(a) 4.3s, (b) 3.7s (c) 3.9s and(d) 4.0s

Figure 3.13 shows a comparison of the computational and experimental velocity profiles at each time step. The time steps chosen were time steps that were below transition time as shown in Figure 3.10. The transition time is the time where the experimental and computational profiles

no longer agree. As shown in Figure 3.13, the maximum error tends to be near the wall. This error is due to the harmonics present in the system and the distortion of the light sheet entering the conduit from the laser.

3.5 Dye Mass Concentration Methodology

For the present study, a dye mass concentration study was conducted on the phantom. The dye mass concentration methodology consists of measuring the dye front of the fluid. A time dependent point measurement can be taken at any point on the phantom. A detailed overview of this is provided in Chapter 4. However the methodology is discussed here. The dye mass concentration method is conducted via optical measurements using a standard LED light and CMOS camera system. The same camera system from the PIV system is used. The equation used to measure mass concentration is shown below:

$$C = \frac{m_{solute}}{m_{solution}} \qquad \text{Eqn. 3.21}$$

Prior to collecting any mass concentration measurements of the dye, the system setup had to be calibrated. The calibration consisted of creating known concentrations of the fluid (water) to dye and measuring the intensity. A Matlab script file was written to measure the intensity of images. The intensity could then infer a concentration measurement. It is assumed that both the ratio of initial intensity to indexed intensity is proportional to the ratio of initial concentration to indexed concentration as shown below:

$$\frac{I_0}{I} = \frac{C_0}{C} \qquad \text{Eqn. 3.22}$$

The intensity script written in Matlab collects the images and converts the image to a scaled grey image of 256 levels of gray. The 256 level of gray (all white) is considered to be the 0 concentration of fluid (no dye). The 0 level of gray which is all black is considered to be 1

concentration (black). Figure 3.14 shows the test tube with a concentration of dye to water and the LED light used. The script creates a measurement line across the tube and measures the average intensity across the diameter of the test tube. The test tube is made of the same material as the phantom so that an accurate mass concentration measurement could be made.

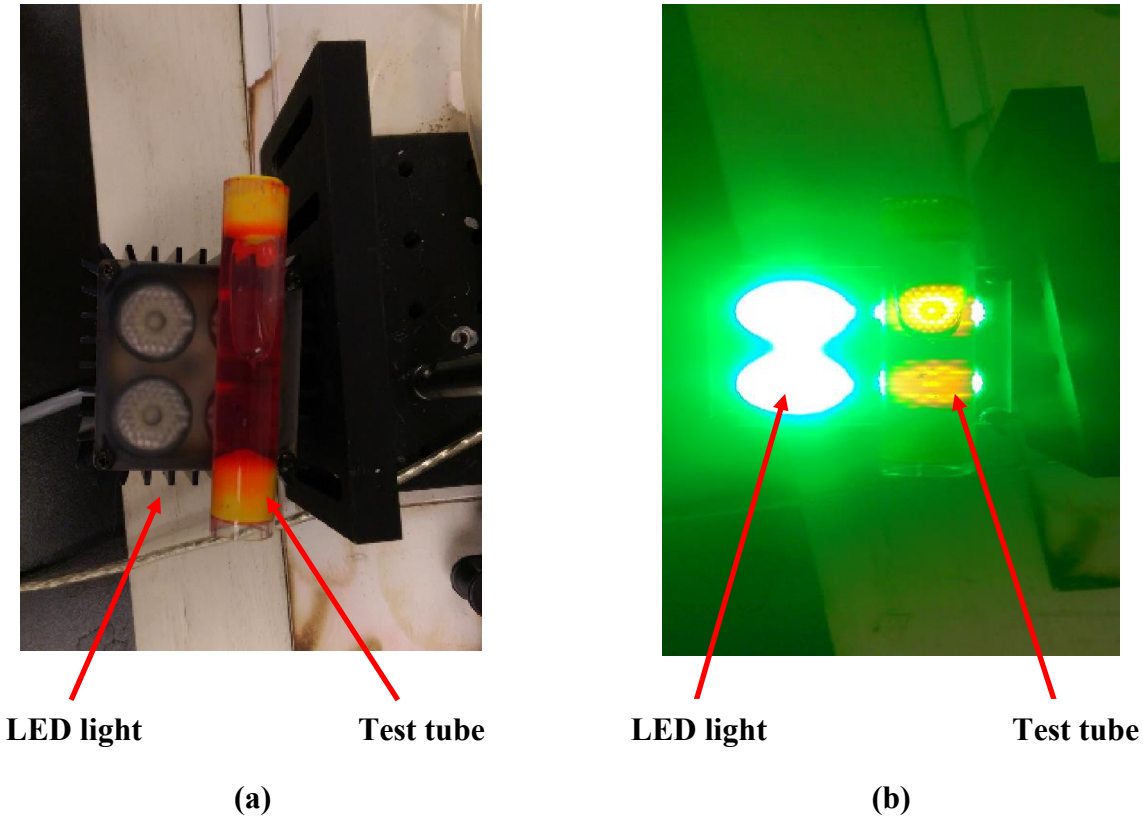

Figure 3.14. Dye Mass Concentration apparatus setup: (a) LED light of with a known mass concentration in fluid and (b) Light on with known mass concentration.

Eight mass concentrations were made ranging from 0 to 1. Each mass concentration was converted to intensity and a calibration plot was generated. The calibration plot of the Concentration vs. Intensity is shown in Figure 3.15. The calibration equation is shown and the R value for the line of best fit is 0.9975. The next section presents the stent geometry generation methodology for CFD.

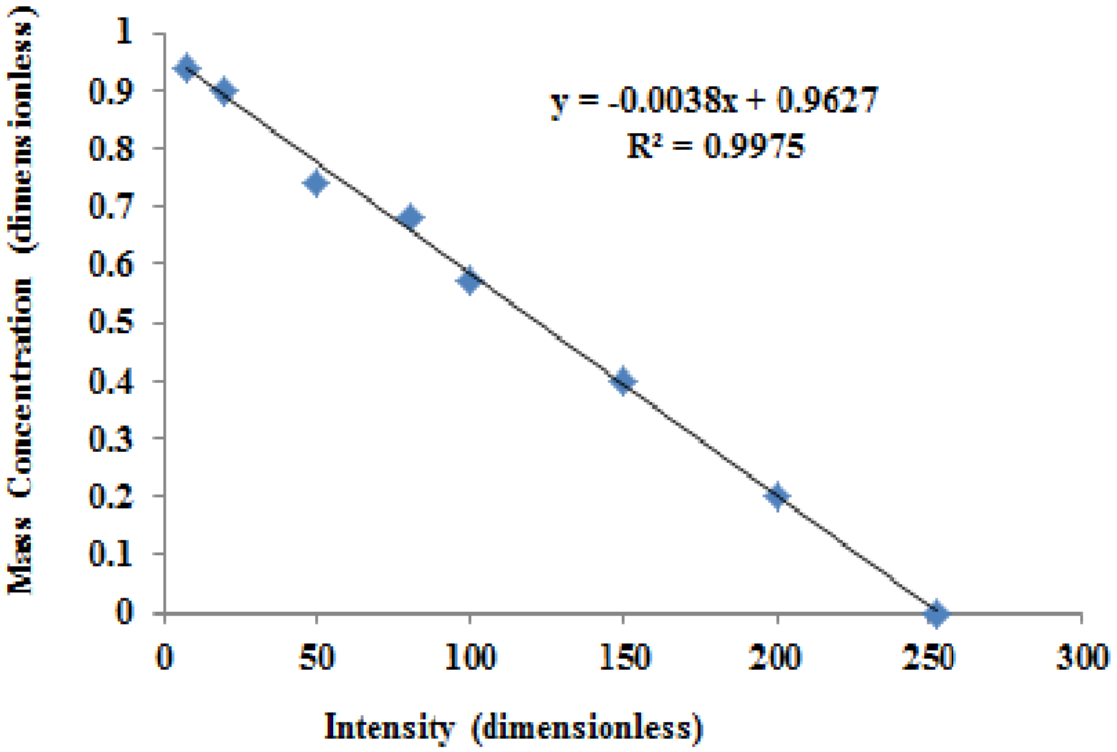

Figure 3.15. Calibration plot of Dye Mass Concentration setup.

3.6 Stent Geometry Modeling and CFD Modeling Methodology

The three in-house stent design patterns evaluated in the present work are similar to stents manufactured by Abbott Laboratories (Abbott Park, Illinois, U.S.A.) and Biosensors (Europe, SA (BESA), Switzerland). The geometric details of each stent are provided in Table 3.5. To make a design comparison, representative geometries for each stent are constructed with the same strut: diameter (5 mm), length (24 mm), and thickness (0.24 mm). The strut spacing for each stent design evaluated is representative and differs to some extent from commercially available stent designs. Figure 3.16 shows the flattened out geometries for the three in house stent designs. The flattened out geometries shown in Figure 3.16 were created in Solidworks.

The flattened geometry was sketched on a plane, extruded to the required thickness, and then converted to a circular meshed tube (stent) using a wrap feature. For CFD simulations in the present work, the flow in the carotid bifurcation artery is Newtonian, laminar, and incompressible.

Table 3.*5*

Geometric details of stent models.

Model label	**A**	**B**	**C**
Number of Columns	**10**	**10**	**10**
Number of Struts	**42**	**10**	**72**
Outer diameter	**5 mm**	**5 mm**	**5 mm**
Strut thickness	**0.24 mm**	**0.24 mm**	**0.24 mm**
Length	**20.25 mm**	**20.25 mm**	**20.25 mm**
Aspect Ratio (e/d)	**0.048**	**0.048**	**0.048**
Aspect Ratio (e/L)	**0.012**	**0.012**	**0.012**
Aspect Ratio (d/L)	**0.250**	**0.250**	**0.250**

The physiological assumptions used in the present work has also been used in the work of (Siauw, Ng et al. 2000; Zhao, Ariff et al. 2002; Farmakis, Soulis et al. 2004; Giannoglou, Soulis et al. 2005; Cheung, Wong et al. 2010). Blood is modeled by the incompressible Navier-Stokes equations with blood density specified as 1060 kg/m^3 and the corresponding kinematic viscosity 0.0032 m^2/s. The commercial software ANSYS was used for geometric meshing and FLUENT^{TM} was used to solve the Navier-Stokes equations in the finite volume formulation.

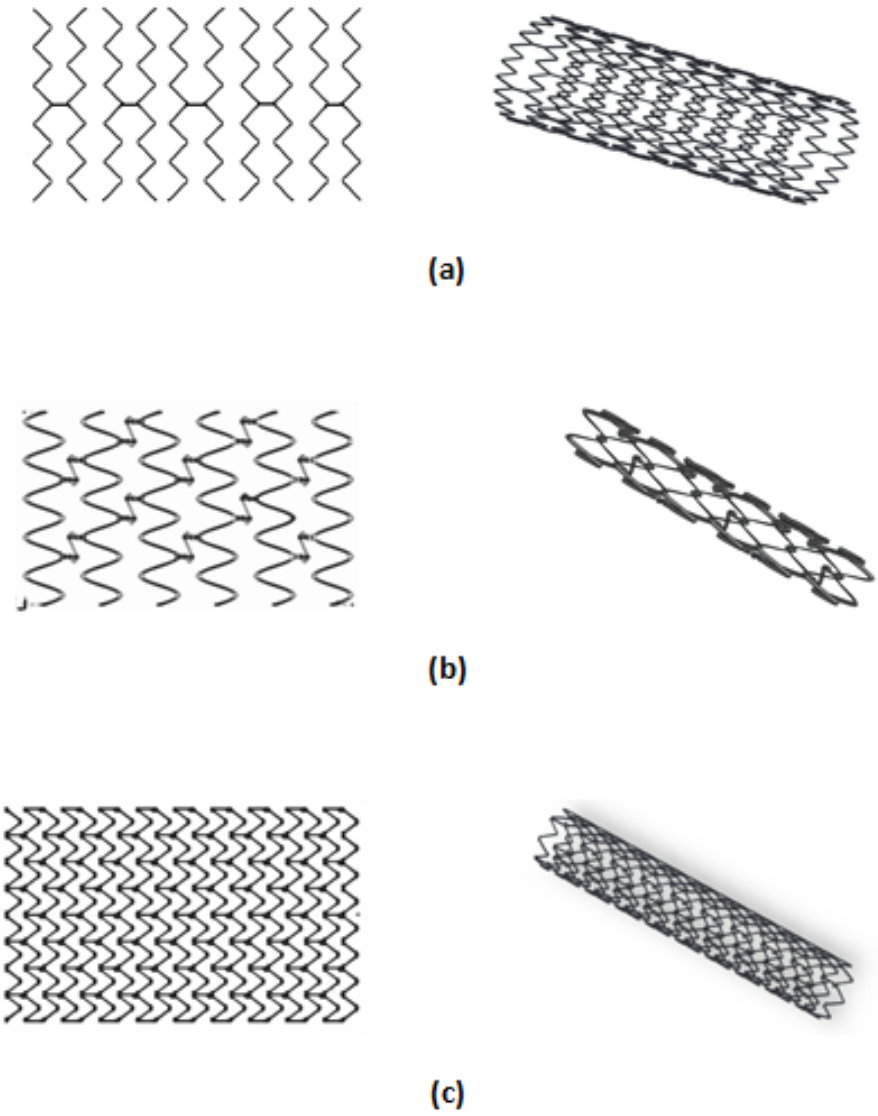

Figure 3.16. Stent designs used for the present study.

Numerical simulations were performed for simplified arterial stented cores and patient-specific arterial stented cores. Figure 3.17 shows the simplified arterial stented cores and patient-specific arterial cores that were evaluated in the present work. The simplified arterial stented cores consisted of a half-plane stented segment since the stent is axisymmetric as shown

in Figure 17b. The patient-specific stented core consisted of an arterial geometry obtained from a computed angiographic (CT) scan of a 50 year old male as shown in Figure 16c. The image contained a point cloud, which defines the surface geometry of the carotid bifurcation by discrete domains. The image was processed in CAD software called Solidworks using a curve creation feature. The curve creation feature united the point cloud with 3-D surface splines. This technique was repeated at each domain until the entire arterial geometry was defined. Each 3-D spline domain was then united using a lofting and boundary boss feature until the final solid product was obtained. This process is outlined in (Hewlin and Kizito 2011). The arterial wall at the stented region for both the simplified arterial stented core and the patient-specific arterial stented core is straight with constant diameter.

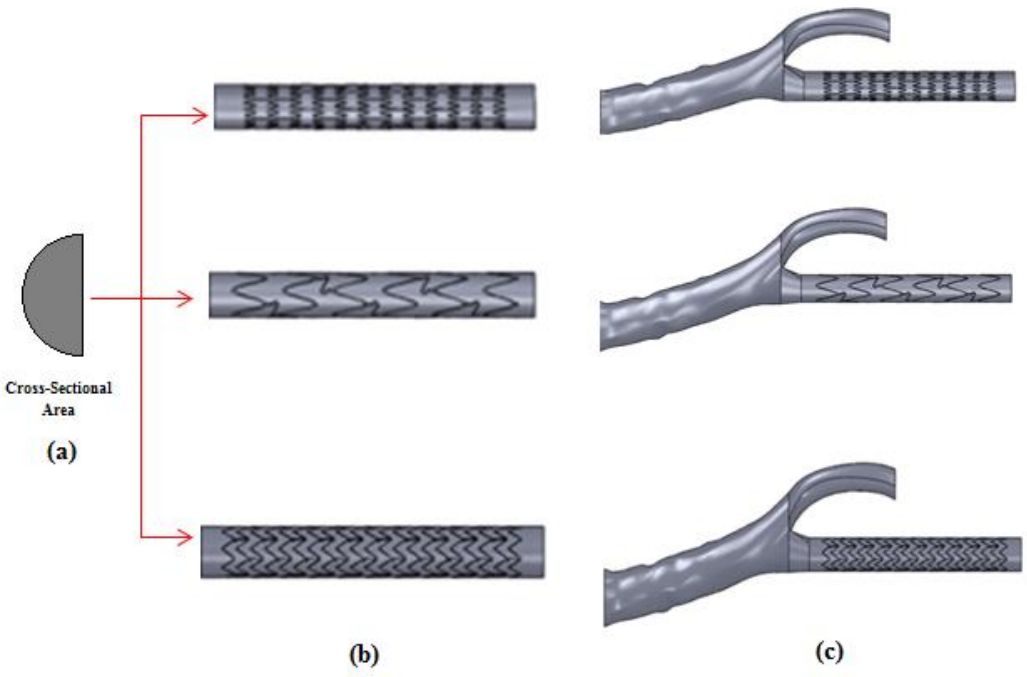

Figure 3.17. Arterial stented fluid cores evaluated for the present study.

The three dimensional stented regions were created in Solidworks with a solid cylinder dimensioned 1.5 times the length and the diameter of the core is the same as the stent. The core

geometry represents full strut exposure to the blood flow. The stent geometry and the solid cylinder were united using the mating feature then removed using a Boolean operator in which the geometry of the stent is removed from the cylinder and the stent geometry impression remains in the cylinder. The models are discretized and used as computational domains. Grid meshing levels were performed at three levels: coarse (132,226), coarse (155,998) and medium (306,085). A sinusoidal velocity waveform boundary condition was specified at the inlet and the outlet(s) was modeled as pressure outlets at 12 kPa (90 mmHg). The No-slip boundary conditions were imposed at the walls. The flow velocity amplitude in the inlet of each stented core was set to 0.2 m/s and a heart rate of 168 beats/min (2.8 Hz) to simulate normal cardiac behavior. The comparison of the velocity magnitude at the ICA for arterial stented core geometric models resulted in a 0.32% difference in velocity in a grid independence study. With such a small difference, simulation results were independent of the computational mesh when the disparity between mesh spacing varying densities was less than 1%. For numerical solutions, the velocity coupling solving technique was implemented. Table 3.6 presents the grid independent study.

Table 3.6

Arterial geometry mesh independent study data.

Number of Cells	Wall Shear	Velocity	Pressure
104,406	15 Pa	1.2 m/s	99 mmHg
143,948	8.3 Pa	0.51 m/s	90 mmHg
233,045	8 Pa	0.5 m/s	90 mmHg

The WSS, normal stresses, and vorticity values are predicted on fluid domain surfaces that represent the interface boundary between the fluid, struts, and the neighboring tissue. Figure

3.18 shows the stented core unit cell schematic and geometric data of each stent design. The next section presents the DES drug concentration study methodology.

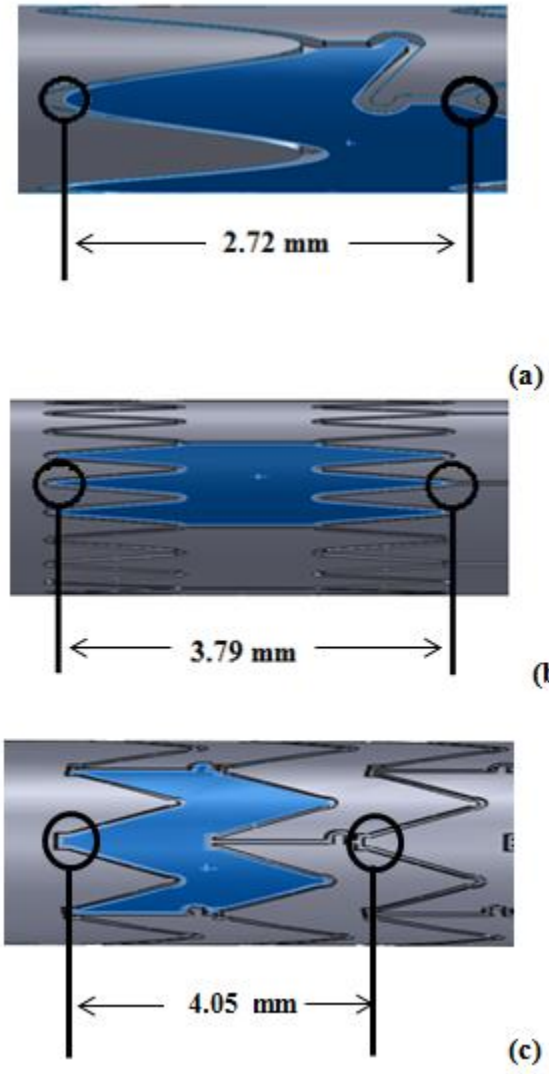

Area	22.07 mm²
Radius	2.3 mm
Perimeter	33.32 mm

Area	4.89 mm²
Radius	2.5 mm
Perimeter	18.39 mm

Area	5.04 mm²
Radius	2.5 mm
Perimeter	16.65 mm

Figure 3.18. Stent Unit cell specifications.

3.7 DES Drug Concentration Study Methodology

Solidworks was used to model the stent deployment to the vessel wall. A schematic of the artery wall and stent impression is shown in Figure 3.19a. In the present study, a transmural pressure drop induces filtration of plasma through the vessel wall. The arterial wall was modeled

as a porous media. The Darcy Law model was used to solve the plasma flow field. Fluent implements the Darcy Law equation as a source term in the Navier-Stokes equations:

$$\rho\left(\frac{\partial v}{\partial t}+v\cdot\nabla v\right)=-\nabla p+\mu\nabla^2-\frac{\mu v}{K} \qquad \text{Eqn. 3.23}$$

where c is the velocity vector, P is the pressure, K is the permeability of the vessel wall, and are the density and viscosity of plasma. The density of plasma is 1.02 g/cm^3 and the viscosity is 0.012 g/cm s. The permeability of the plasma wall was set at 2.0E-18m^2.

The arterial wall concentration profile was not solved in conjunction with fluid flow analyses. Instead, the models were solved separately. This introduces an assumption because the flow decreases axial non-uniformity of the drug in the artery wall. The degree of non-uniformity is observed to increase with increasing aspect ratio of stent struts. The impact of the assumption is minimized by the use of square struts with an abluminal coating which is the case used in the present study.

3.7.1 Boundary Condition for Drug Transport

The boundary conditions for each zone are provided in Figure 3.19. The ‘‘plasma velocity inlets’’ zone represents the exposed inner surfaces of the artery. The ‘‘stent impression’’ represents the location where the stent is in contact with the vessel wall. The rest of the surfaces shown in Figure 3.19 are treated as symmetry planes. For the velocity inlets, a component (x,y,z) velocity inlet is specified. The normal velocity component (v_n) was set equal to 1.0E-8 m/s. The tangential velocity components were set equal to zero on the ‘‘velocity inlets’’ zone. The no-slip condition was applied on stent surface and lumen wall.

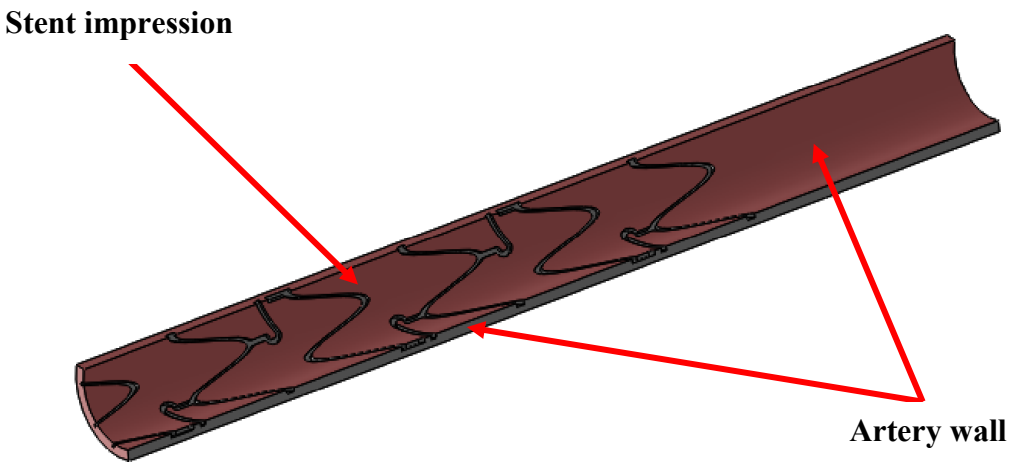

(a)

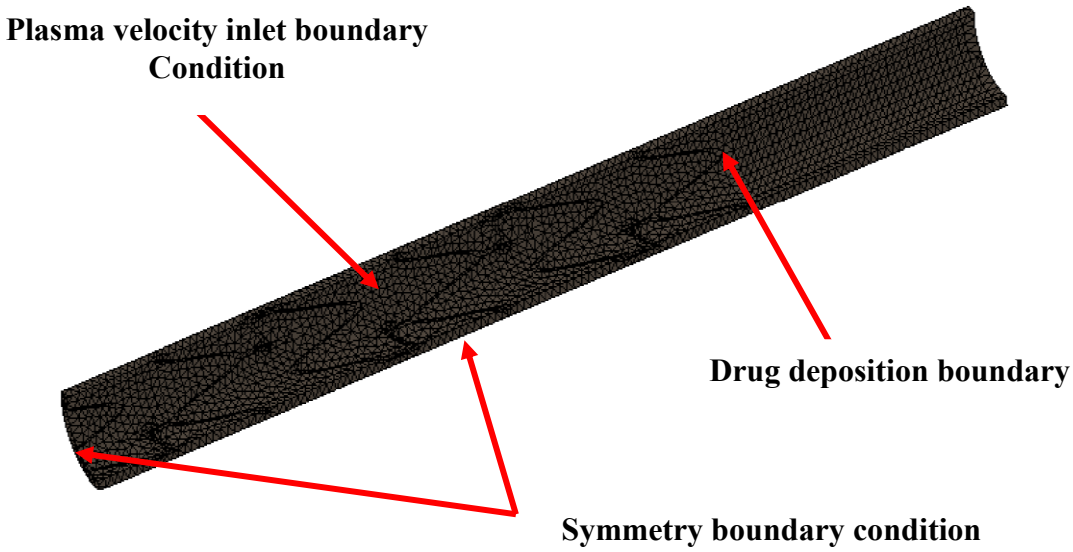

(b)

Figure 3.19. Arterial and DES CFD geometry model: (a) solid model and (b) computational mesh.

3.7.2 Formulation of the Drug Transport Model

For the Drug transport problem, the vessel tissue was modeled as a composite material, one unbound and bound. The bound material is a collection of drug binding sites, and the unbound compartment as the neighboring constituents. Each material is a homogeneous material. The elution process is modeled such that the drug diffuses out of the stent coating into the plasma and then partitions into and out of the drug binding site compartment. A two-species model was used to account for the two materials and the partitioning of the drug between the two materials. The free transport of the drug into the unbound material which is referred to as C_u. The restrained drug is referred to as the bound drug, denoted C_b. The inter-conversion between the unbound plasma phase and the bound phase of tissue binding sites is controlled via an equilibrium reaction described by:

$$C_u \underset{k_R}{\overset{k_F}{\rightleftharpoons}} C_b \qquad \text{Eqn. 3.24}$$

Where k_f is the forward reaction rate and k_r is the reverse reaction rate, K_{eq} is the equilibrium coefficient which is equal to the ratio of the forward and reverse reaction. The affinity drug for the plasma phase decreases as k_{eq} increases. The reaction rate R between the bound an unbound form is:

$$R = k_f C_u - k_r C_b \qquad \text{Eqn. 3.25}$$

The unbound drug is subject to transport by plasma flow, diffusion, and reaction. The transport equation for the unbound drug is given by:

$$\frac{\partial C_u}{\partial t} + v \cdot \nabla C_u = D_u \nabla^2 C_u - R \qquad \text{Eqn. 3.26}$$

where D_u is the diffusion tensor for the unbound drug. The unbound drug was assumed to by completely immobilized in the tissue. This was accompanied by setting v=0, which leads to the following transport equation for C_b:

$$\frac{\partial C_b}{\partial t} = D_b \nabla^2 C_b + R \qquad \text{Eqn. 3.27}$$

where D_b is the diffusion tensor for bound drug. The contribution of the diffusion term was minimized by setting D_b=1.e-7D_u.

3.7.3 Initial and Boundary Condition for the Drug Transport Model:

The arterial wall was assumed to have no drug present at the time of stent implantation, therefore the concentration at the wall was set to zero. The boundary conditions for the model were:

$$C_{u,stent} = 1 \qquad \text{Eqn. 3.28}$$

$$C_{u,lumen} = 0 \qquad \text{Eqn. 3.29}$$

$$\frac{\partial C_{u,sidewalls}}{\partial \eta} = 0 \qquad \text{Eqn. 3.30}$$

$$\frac{\partial C_{u,outerwall}}{\partial \eta} = 0 \qquad \text{Eqn. 3.31}$$

The zero concentration of drug at the lumen assumes a continuous supply of drug in the stent coating. This is probably the most unrealistic of the applied boundary conditions as it is typical for the drug to be depleted after 1–3 months. The zero concentration of drug at the lumen also assumes that the drug concentration in the blood is negligible. Eqn. 3.30 is a symmetry condition and Eqn. 3.31 assumes that the convective flux is the dominant transport mechanism at the far wall. Zero-flux boundary conditions were applied for C_b at all domain boundaries since

the convective and diffusive components were assumed to be negligible for this drug form. The next Chapter presents the results for the present study.

CHAPTER 4

Results

4.1 Cardiovascular Phantom Posture Transition Studies

In this section, the present study addresses the cardio- and cerebrovascular responses to the everyday orthostatic challenge of moving from bed rest to upright standing position. The vascular pressure change (cerebral and femoral) profiles that occur doing a transition from bed rest to an upright position on the cardiovascular phantom is discussed. The age range of the simulated subject (cardiovascular phantom) is 28-40 years of age. The most prominent condition that is accelerated and progressed by an accelerated change in posture is orthostatic hypotension and intolerance. The results discussed are addressed to provide insight on the magnitude of vascular pressure changes and the types of parametric profiles that exist during a transition from bed rest to upright position.

Orthostatic intolerance is a broad term used for several conditions characterized by symptoms of light headedness, dizziness and faintness on assuming upright posture. The underlying mechanism of orthostatic intolerance is the inability of the autonomic nervous system to maintain adequate hemodynamic behavior of the body during upright posture resulting in cerebral hypoperfusion which leads to its symptoms. Upright posture is the most physiological orthostatic stressor and it imposes stress leading to gravitational pooling of blood in the splanchnic venous reservoir and leg veins. On standing 300 to 500 ml of blood is forced downward to the abdominal area and lower extremities. A healthy subject is able to reach orthostatic stabilization in 60 seconds or less by an increase in sympathetic outflow resulting in vasoconstriction of capacitance and arteriolar vessels. However, in patients with orthostatic intolerance this compensatory mechanism is disturbed and reflex mediated changes in autonomic

nervous system leads to decreased vascular tone, heart rate and cardiac output with resultant acute cerebral hypo perfusion. Normally a reproducible cardiovascular reactivity (CVR) pattern mediated via autonomic nervous system results in slight increase 10–15 bpm in heart rate and blood pressure 10–15 mmHg (1.33-2 kPa) to balance the situation. When autonomic nervous system is dysfunctional normal CVR pattern is altered so that blood pressure is not maintained at adequate levels during upright posture resulting in cerebral hypo perfusion and symptoms of orthostatic intolerance.

In the absence of volume depletion, younger patients with orthostatic hypotension usually have chronic autonomic failure. A related problem, postprandial hypotension, is common in older patients and those with autonomic dysfunction. In postprandial hypotension, there is a decrease in systolic blood pressure of at least 20 mmHg (2.7 kPa) within 75 minutes of a meal. A normal hemodynamic response to changes in posture requires normal function of the cardiovascular and autonomic nervous systems. Standing results in blood pooling of approximately 500 to 1,000 mL in the lower extremities and splanchnic circulation. This initiates an increase in sympathetic outflow, which increases peripheral vascular resistance, venous return, and cardiac output, thereby limiting the decrease in blood pressure. These compensatory mechanisms result in a decrease in systolic blood pressure 5 to 10 mmHg (0.67-1.33 kPa), an increase in diastolic blood pressure 5 to 10 mmHg (0.67-1.33 kPa), and an increase in pulse rate (10 to 25 bpm). However, orthostatic hypotension may result if there is inadequate intravascular volume, autonomic nervous system dysfunction, decreased venous return, or inability to increase cardiac output in response to postural changes. Decreased cerebral perfusion produces the neurologic symptoms of orthostatic hypotension.

Figure 4.1 presents a plot of the scaled hemodynamic flow parametric flow profiles. The flow profiles are scaled and plotted on the same graph to show that a time lag exists between the profiles. The volumetric flow rate waveform is scaled with the maximum flow rate, which is the flow rate at systole and the pressure waveform is scaled with the maximum pressure at systole. As shown in Figure 4.1, there is a time lag from the systolic peak of the pressure waveform to the systolic peak of the flow rate wave form (peak to peak) at 0s, 1s, 2s, and 3s. However, the time lag at 1s is different between the time lag at 1s, 2s and 3s. This may be due to some abnormality during startup or during data capturing. The time lag between the profiles is at systolic peaks is 0.3s, and 0.5s at diastolic peaks. This is due the pulsatile pressure being the driver of the flow and the flow rate being the response. Also in the present study, a static trial was conducted to measure the pressure change from cerebral (head) to femoral (feet) during bed rest (lying down) and upright (standing up).

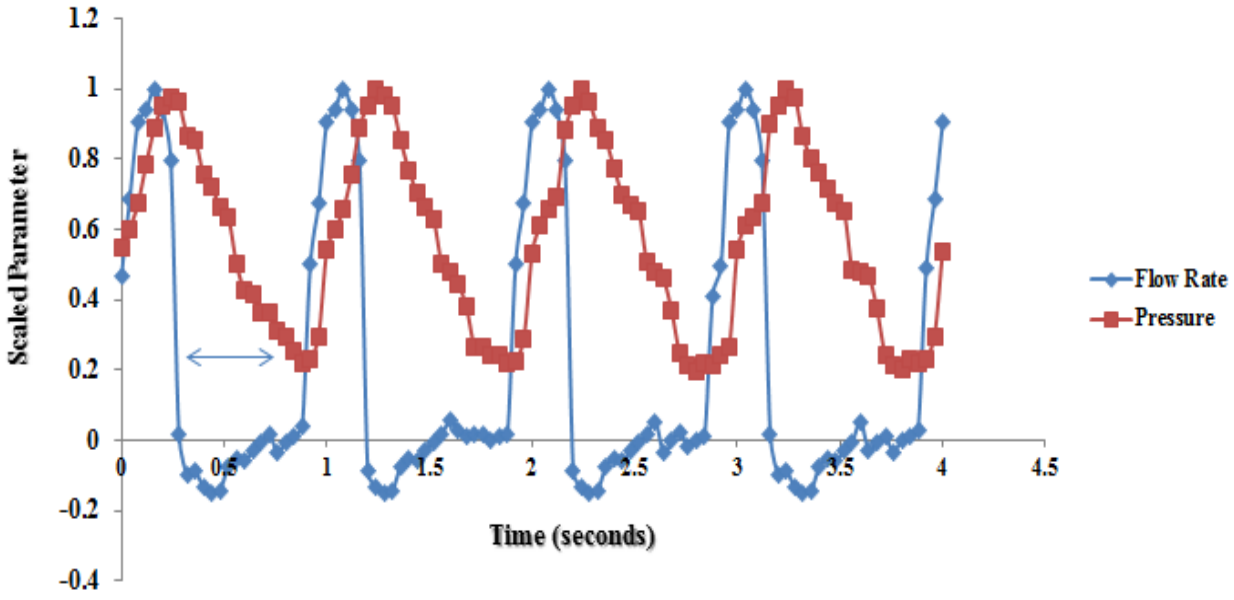

Figure 4.1. Static parametric flow profiles: (a) unscaled volumetric flow rate, and (b) scaled volumetric flow rate and pressure.

The negative flow rate observed in Figure 4.1 is due to a regurgitation of flow (reverse flow).

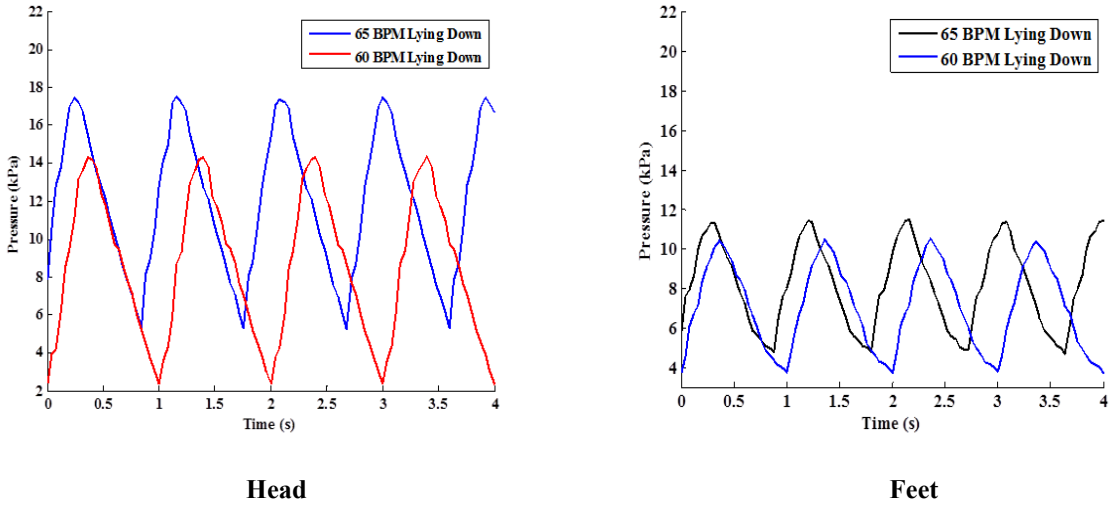

(a)

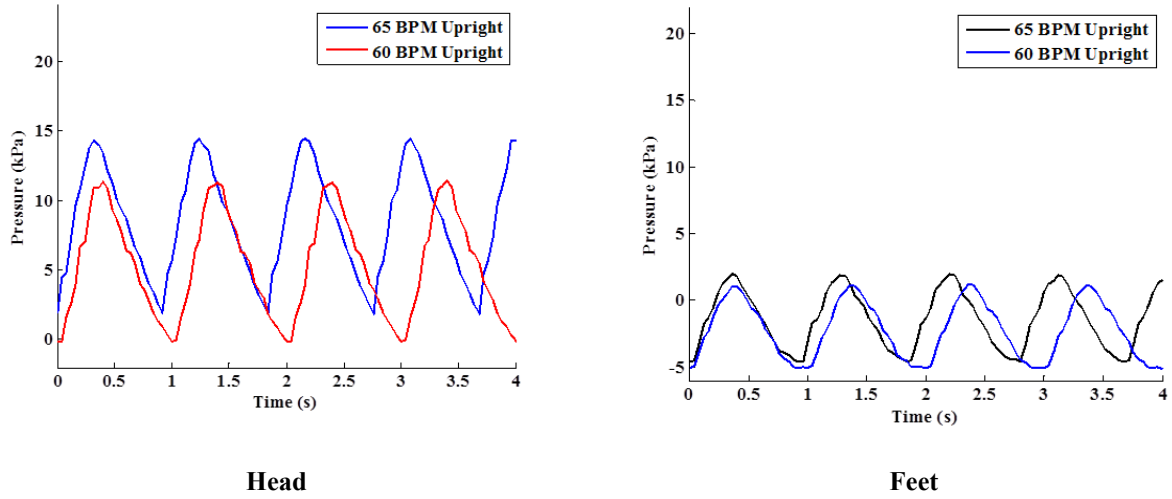

(b)

Figure 4.2. Static trial run pressure results for: (a) lying down and (b) standing up (upright).

Two heart rates were evaluated (60 and 65 bpm) to simulate rest state (normal heart rate) and semi-exercise (accelerated heart rate). Figure 4.2 provides a plot of pressure changes from head to feet in both lying down position and upright position. From Figure 4.2, during the lying

down position and during rest state cycle, the head systolic pressure is 14 kPa (105 mmHg) and the head diastolic pressure is 2 kPa (15 mmHg). During the semi-exercise (accelerated heart rate) cycle and lying down, head systolic pressure is 17.2 kPa (129 mmHg) and head diastolic pressure is 5.8 kPa (43.5 mmHg). During the lying down position and during rest state cycle, feet systolic pressure is 10.2 kPa (76.5 mmHg) and the feet diastolic pressure is 5.4 kPa (40.5 mmHg). During the semi-exercise (accelerated heart rate) cycle and lying down, head systolic pressure is 17.2 kPa (129 mmHg) and head diastolic pressure is 5.8 kPa (43.5 mmHg). For upright position and during rest state, the head systolic pressure is 10.4 kPa (78 mmHg) and the diastolic head pressure is 0 kPa (0 mmHg). During the semi-exercise cycle and in the upright position, the systolic head pressure is 14.8 kPa (111 mmHg) and the diastolic head pressure is 2.5 kPa (18.8 mmHg). The feet systolic pressure during upright position and during rest state was found to be 1kPa (7.5 mm Hg) and diastolic pressure was -5 kPa (-37.5 mmHg). The feet systolic pressure during upright semi-exercise 3 kPa (22.5 mmHg) and diastolic pressure is -4 kPa (-30 mmHg).

A more generalized statement is that the pressure difference from systolic to diastolic is approximately 12 kPa (90 mmHg) during rest state cycle and exercise, whereas the feet systolic to diastolic pressure difference during rest state and exercise is approximately 5 kPa (37.5 mmHg). The systolic pressure difference from head to feet during rest state and lying down is 4 kPa (30 mmHg) and the systolic pressure difference during rest state and upright is 9 kPa (67.5 mmHg). The pressure cycles show a shift in time phase between heart rates. The phase shift in head pressure 0.25 seconds and the phase shift for feet pressure are 0.2 seconds. The pressure difference between head and feet is important because it gives insight on the level of blood return to the heart, pressure spikes during posture transition, and magnitude of oxygen transfer.

Pressure difference is also important when considering accelerated movement from bed rest to upright position. This pressure difference is referred to as blood pooling. Because of this pooling, the amount of blood carried back to the heart by the veins is decreased. Subsequently, less blood is pumped out from the heart, resulting in a sudden drop in blood pressure. By definition, the drop in blood pressure must be greater than 2.6 kPa (20 mmHg) during contraction of the heart muscles (systole) and more than 10 mm of mercury during expansion of the heart muscles (diastole). Normally, specialized cells in the body (baroreceptors) quickly respond to changes in blood pressure. These baroreceptors then activate the autonomic nervous system to increase, via reflex action, and increase levels of catecholamines (e.g. epinephrine, norepinephrine) in the body. Increased catecholamine levels rapidly restore the blood pressure. A defect in this spontaneous response (reflex) prevents the heart rate and blood pressure from rising adequately and orthostatic hypotension results.

Figure 4.3 shows a plot of the pressure cycle profiles during transition from bed rest to upright position. The two pressure cycle profiles simulate two scenarios, an atherosclerotic diseased stenosis at the ascending aorta (stenosed at 42%) and a hypertension stage 1 patient. Table 4.1 provides an outline of the stages of hypertension and the analogous hemodynamic conditions.

Table 4.1

Orthostatic hypertension blood pressure assessment.

Systolic Blood Pressure	**Diastolic Blood Pressure**	**Assessment**
Below 120	Below 80	Normal
120-139	80-89	Prehypertension
Over 140-159	90-99	Hypertension Stage 1
160 or higher	100 or higher	Hypertension Stage 2

From Figure 4.3, the hypertension stage 1 pressure cycle has a maximum systolic pressure of approximately 136 mmHg in the time range of 3.7 seconds. After 3.7 seconds the phantom is transition to bed rest to upright position and the systolic head pressure changes to 126 mmHg (16.8 kPa) at and 124 mmHg at (16.5 kPa) and stabilizes to 120 mmHg (12 kPa). For the stenosis case, the maximum head pressure is at 159 mmHg (21.2 kPa) in the range of 3.7 seconds. After 2.4 seconds, the pressure spikes to 163 mmHg (21.7 kPa) at 3.44 seconds and 151 mmHg (20.1 kPa) 4.4s and then 149 mmHg (19.9 kPa) at 5.4s and then stabilizes to 145 mmHg (19.33 kPa). From the static condition mentioned previously and referring to Figure 4.1, the maximum pressure is 70 mmHg (9.33 kPa) for normal conditions in the upright position. A comparison can be made between normal, stage 1 hypertension and a 42% stenosis case.

The transition pressure difference for normal and stage 1 hypertension is 66 mmHg (8.8 kPa) and the stabilized pressure difference is also 50 mmHg. The most notable difference (6.7 kPa) is the pressure difference during the maximum pressure and transition pressure. The transition pressure has to be greater than 2.6 mmHg (0.35 kPa) to avoid blackout. The transition pressure for stage 1 hypertension is 2 mmHg (0.27 kPa) and the transition pressure for the stenosed case is 1 mmHg after the spike in pressure during the transition. For both cases the phantom produces hemodynamic data which suggest the patient will be subject to blackout during posture changes. In terms of pressure head, the pressure head is higher when the phantom is in bed rest position as oppose to upright position. The reason that the pressure is higher during bed rest position is because the pump produces less work when gravity is negligible. The pressure head is calculated using the density, gravity, and height. When the pump is working against gravity the pressure is less as oppose to negligible gravity.

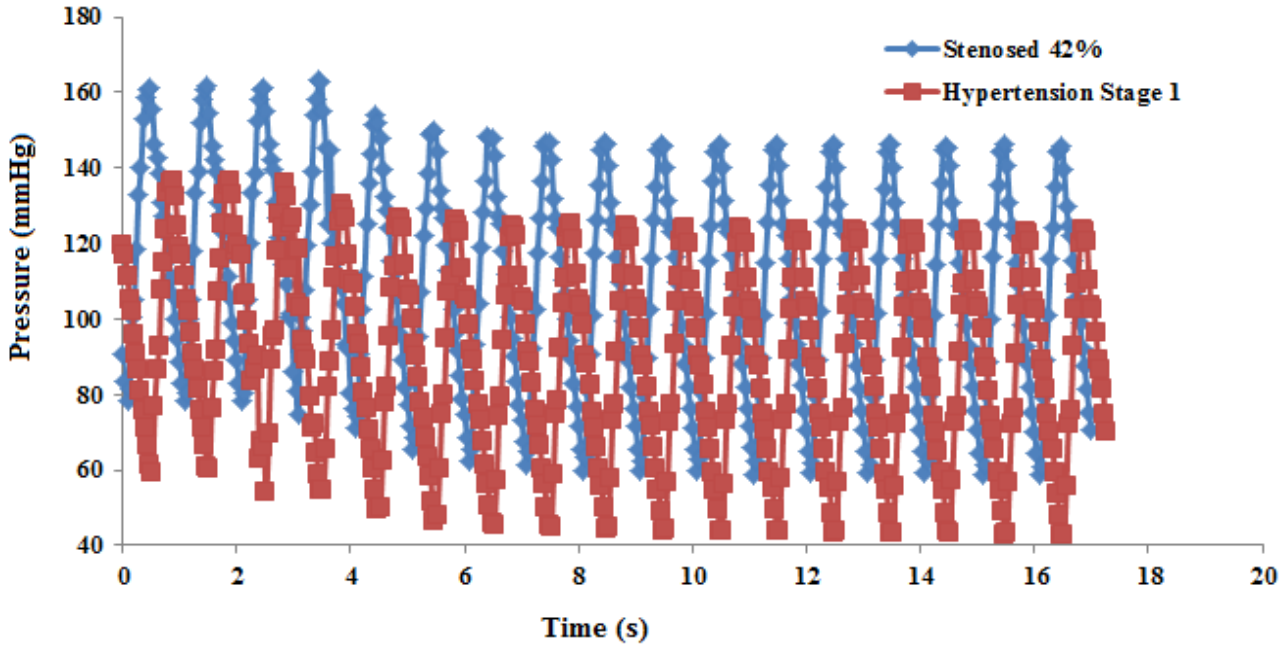

Figure 4.3. Posture transition pressure cycles at.

Figure 4.3 present the transition pressure for several cases of stenosis. In Figure 4.3, it is shown that for a normal case the maximum transition pressure is 120 mmHg (16 kPa) and for the stenosis case presented earlier (42% stenosis), the pressure is 151 mmHg (20.1 kPa). For an extremely severe case, the maximum transition pressure is 170 mmHg. Figure 4.3 is useful in the sense that it provides insight of the magnitude of transition pressure that occurs for each stenosis case. Data shown in 4.3 can provide useful information to interventionist that aim to address early onset atherosclerosis and orthostatic hypotension cases prior to extreme stages of stenosis.

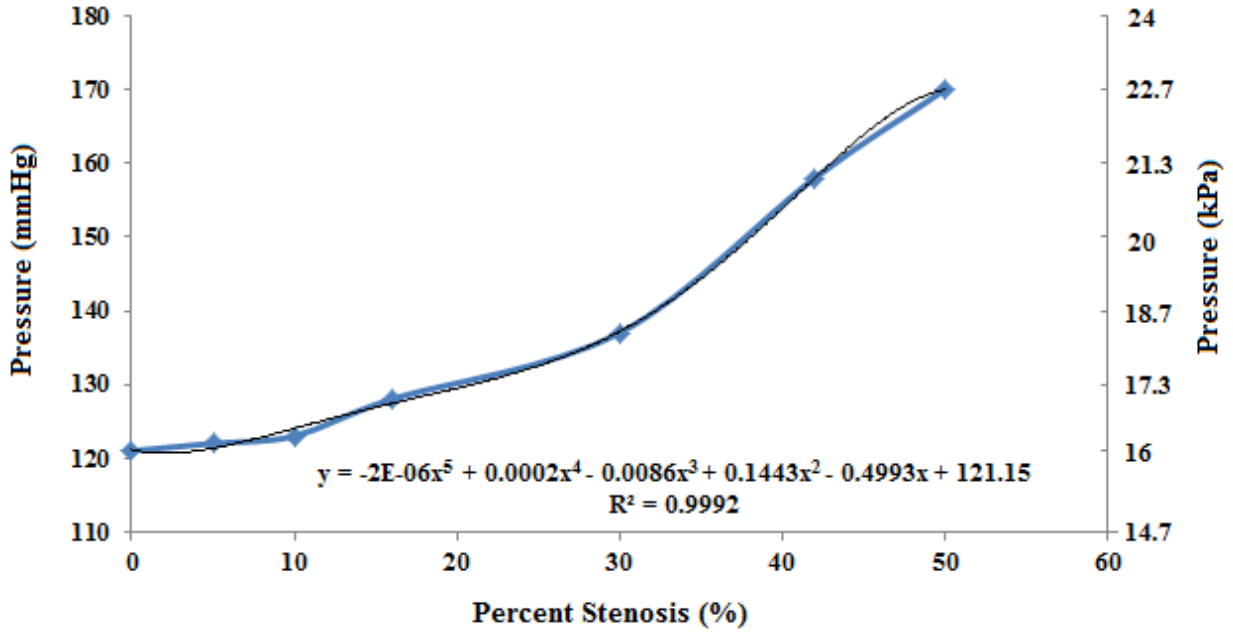

Figure 4.4. Pressure change versus percent stenosis.

A general conclusion from the data mentioned is that stage 1 hypertension occurs at 40% stenosis and the onset of blackout occurs within this regime. The next section of the present study presents a study on the transfer of dye in the cardiovascular phantom.

4.2 Cardiovascular Phantom Dye Mass Concentration Studies

In the present study, a dye mass concentration study was performed on the ascending aorta of the experimental cardiovascular phantom. The transport of dye mass in the present study is performed to simulate the transport of an injected medical drug (intravenous drug delivery/intra-arterial drug delivery). Intravenous injection involves injecting the aqueous form of a drug into a superficial vein or continuous infusion via a needle or a catheter placed in an artery or deep vein. This is the only method of administration available for some drugs and is chosen in emergency situations because of the onset of action is rapid following injection.

Theoretically, none of the drug is lost, and smaller doses are required other than with other routes of administration. The rate of injection can be controlled for prolonged and continuous administration. Intra-arterial involves direct injection into the arteries and is not a usual route for therapeutic drug administration. Arterial puncture and injection of contrast material has been carried out for angiography. Most of the intra-arterial injections or arterial perfusions via catheters placed in the artery for regional chemotheratpy of some organs and limbs. Intra-arterial drug delivers is mostly used for the treatment of malignant tumors of the brain. Although the goal of the present study is centered towards cardiovascular disease and not cancer, dye transport is important in cases of cardiovascular disease such as the erosion of a medical drug coating from a stent, the deposition and transport of plaque in the cardiovascular system, and the transport of a x-ray dye into the cardiovascular system to map out blood flow trajectory paths.

The present study determined the transit time of the dye front, the axial physiological Peclet numbers, and the validity of using numerical experiments as a surrogate for experimental setups. The physiological Peclet number provides information on convective and diffusive dominance. As mentioned previously mentioned in Chapter 3, the dye mass concentration methodology consists of illuminating a section of the tubing with a green LED light and filming the time the dye front enters the illuminated area. For the purpose of comparing the experimental mass concentration dye transit times to numerical transit time plots for validity, a digital cardiovascular phantom was constructed using the same CAD model used to construct the experimental cardiovascular phantom for numerical analyses. A schematic of the digital cardiovascular phantom is shown in Figure 4.5.

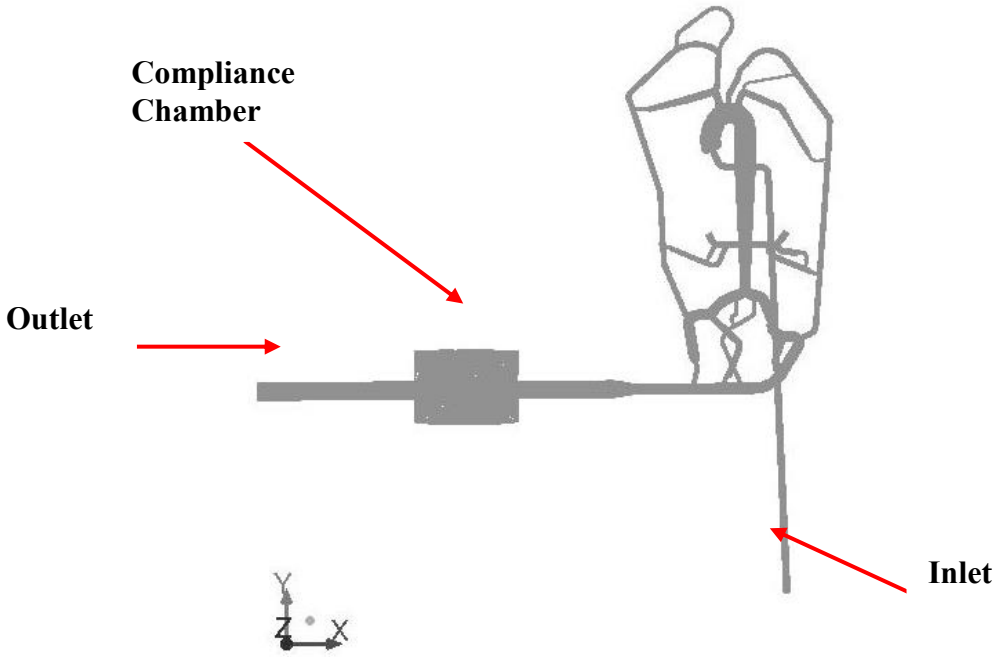

Figure 4.5. CAD schematic of the digital cardiovascular phantom.

During experimental observation, the illuminated section or region of interest (ROA) of the aorta appears to be pure water at the time 0s through about 13s. At approximately 13s, the dye front approaches the ROA around. For visual purposes, the zero mass concentration time was not included in the mass concentration. Figure 4.6 provides a more accurate assessment of the transit time of the dye front. From the time the dye front reaches the ROA, the trend of the graph grows exponentially. The mass concentration is calculated using Eqn. from Chapter 3. The digital cardiovascular phantom contained one inlet and one outlet and a mirrored boundary condition was imposed to simulate a closed loop system. The drug material properties in the dye trace study were set to have the same diffusive properties as a water-in-water solution to simulate a liquid drug injection.

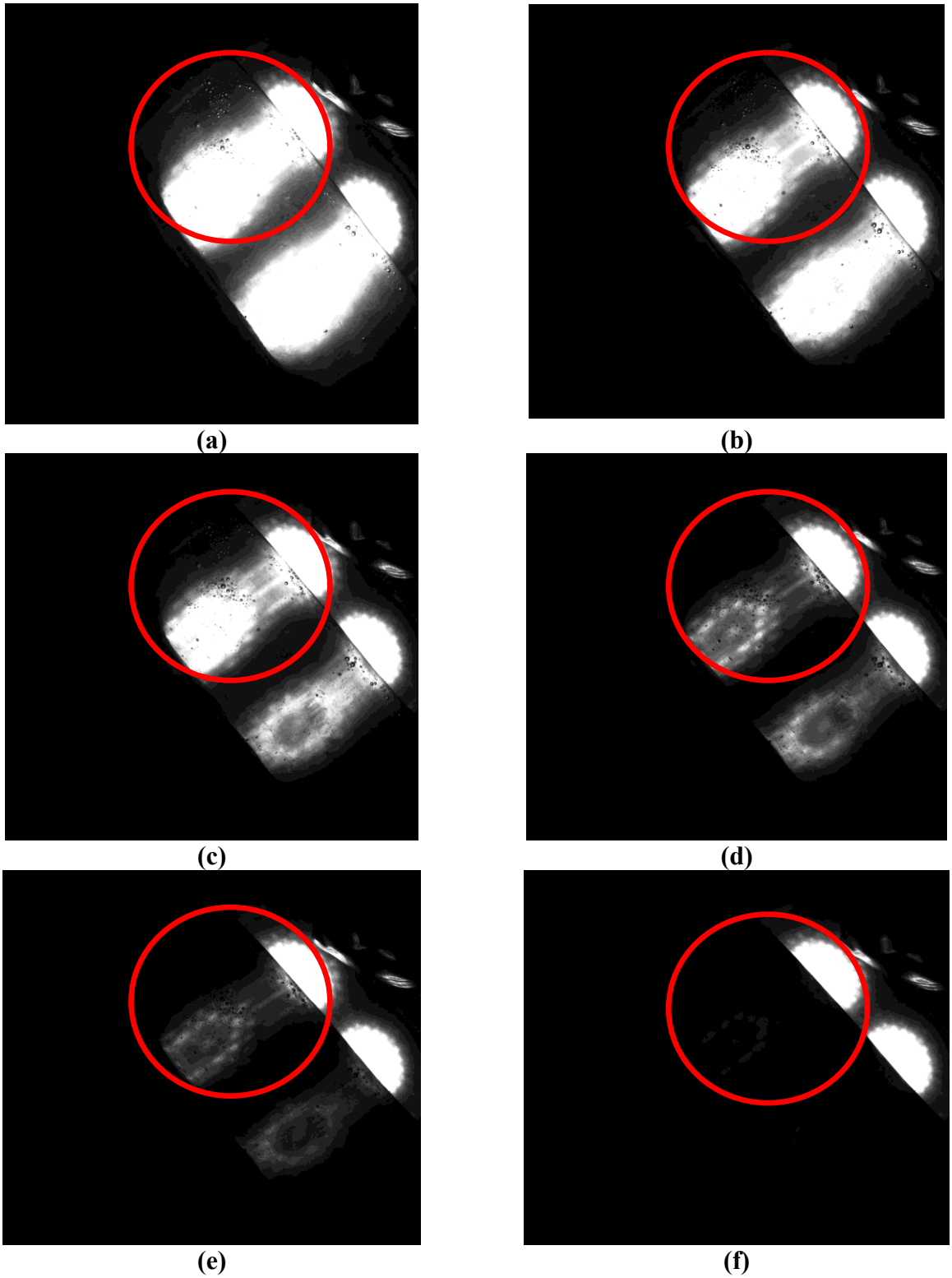

Figure 4.6. Photograph of LED illuminated aortic section for dye mass concentration analysis at: 0.0s (b) 12.58s, (c) 13.05s, (d) 13.67s, (e) 14.012s, and (f) 16.5s

Figure 4.7 provides a plot of the mass concentration vs. time. From 0s until 4s the ROA increases in concentration until it stabilizes at 4s throughout the duration of continuous injection. Based on normal heart rate and bed rest conditions the transit time for the drug to reach the descending aorta is 14s when including the time of injection. The physiological Peclet number is calculated using equation 4.1:

$$Pe = \frac{vh}{D} \qquad \text{Eqn. 4.1}$$

Where h is the distance, v is the velocity and D is the diffusivity. The diffusivity of water is approximately $1.6\text{x}10^{-9}$ m^2/s. The maximum Peclet number (systole) is 20,000,000 whereas the minimum Peclet number is 400,000 (diastole). The physiological Peclet number provides insight on the balance of convection to diffusion.

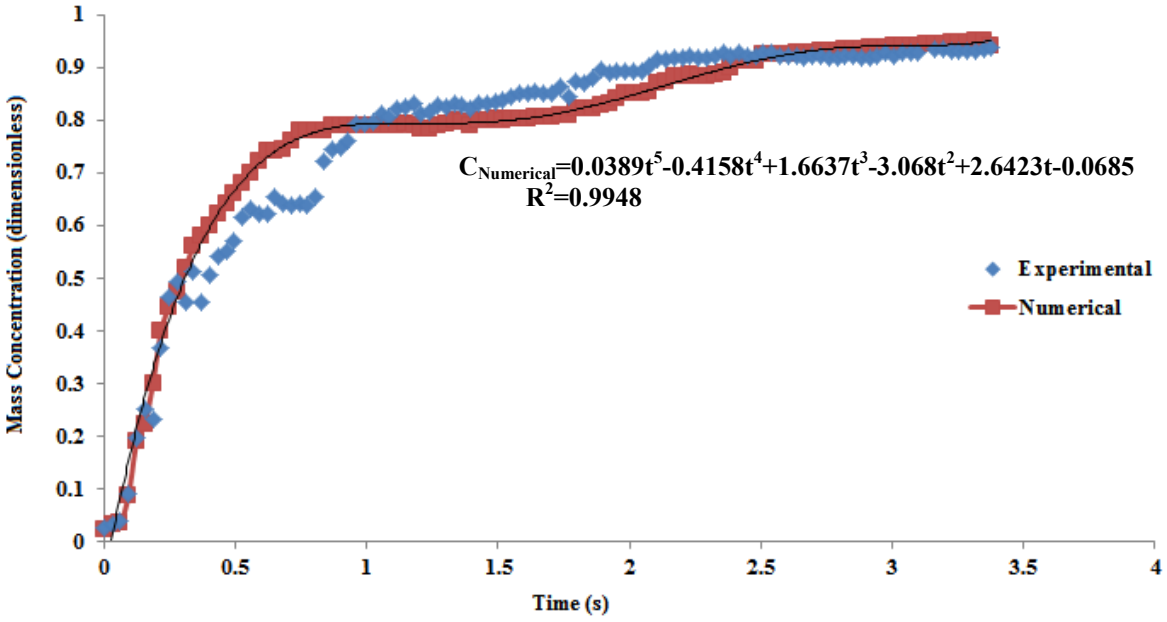

Figure 4.7. Plot of mass concentration vs. transit time.

Figure 4.8 provides a numerical vector and contour plot of the velocity at the section where the numerical mass concentration profile was obtained. A plane was sliced in mid-section of the descending aorta where the mass concentration measurements were obtained to view the magnitude of velocity and provide an explanation of the monotonic behavior/trend in the plot. Figure 4.8a provides a vector plot of the velocity at diastole of the cardiac cycle. The velocity is scaled from 0 to 0.122 m/s in terms of radial velocity. From Figure 4.8a, the direction of the flow points to the outward radial direction and the highest flow occurs in regions near the wall which indicates flow reversal.

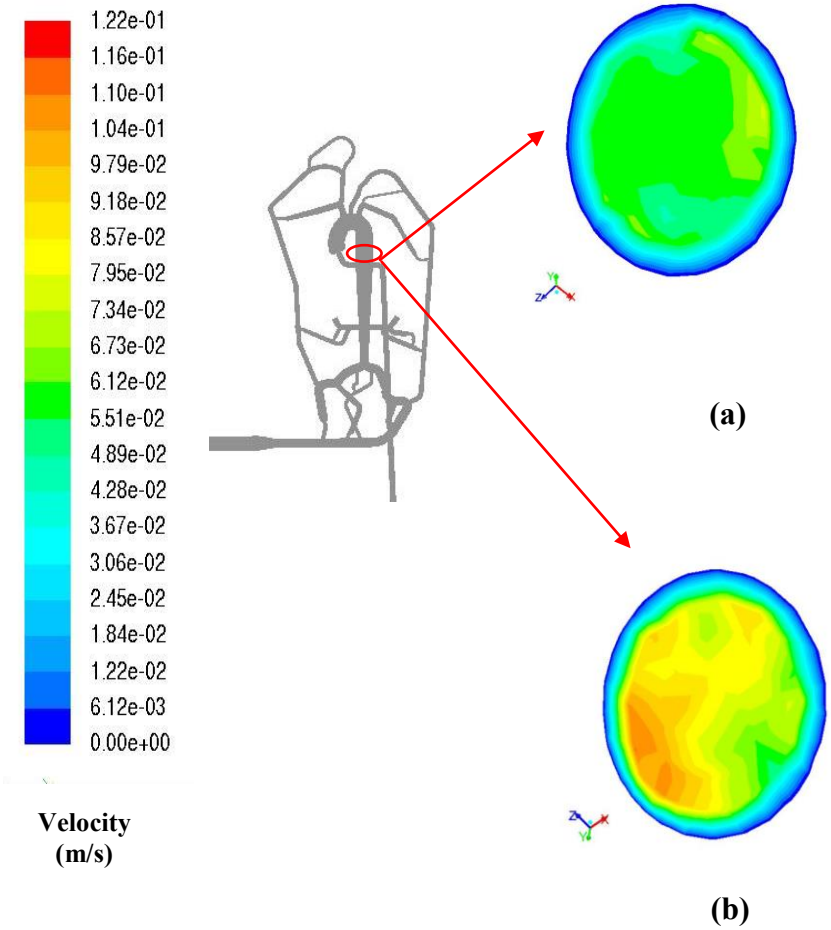

Figure 4.8. Aorta cross-sectional view of: (a) velocity vectors (left) and velocity contour (right) at diastole and (b) velocity vectors (left) and velocity contour (right) at systole.

Also from Figure 4.8, the `highest velocity occurs at the peak and near the wall. Figure 4.9 provides a snapshot of the vorticity at the cross-section of the aorta. Vorticity is defined as the magnitude of the spin of the fluid. An explanation of how vorticity is calculated is provided. The derivation of the vorticity equation begins with the Navier-Stokes equations in vector form:

$$\frac{\partial \vec{V}}{\partial t} + \vec{V} \cdot \nabla \vec{v} = -\nabla\left(\frac{p}{\rho} + gy\right) + \nu \nabla^2 \vec{V} \qquad \text{Eqn. 4.2}$$

By taking the curl of the Navier-Stokes equations, the vorticity equation can be obtained. In detail and taking into account $\nabla \times \vec{u} \equiv \vec{\varpi}$, the following is obtained:

$$\nabla\left(\frac{\partial \vec{V}}{\partial t} + \vec{V} \cdot \nabla \vec{v}\right) = \nabla\left(-\nabla\left(\frac{p}{\rho} + gy\right) + \nu \nabla^2 \vec{V}\right) \qquad \text{Eqn. 4.3}$$

The first term on the left side, for fixes reference frames, becomes:

$$\nabla \times \frac{\partial V}{\partial t} = \frac{\partial}{\partial t}\left(\nabla \times \vec{V}\right) = \frac{\partial \vec{\varpi}}{\partial t} \qquad \text{Eqn. 4.4}$$

In the same manner the last term on the right side becomes:

$$\nabla \times (\nu \nabla^2 \vec{V}) = \nu \nabla^2 \vec{\varpi} \qquad \text{Eqn 4.5}$$

Applying the identity $\nabla \times \nabla \cdot s = 0$, where s is a scalar, the pressure term cancels, provided that the density is uniform

$$\nabla \times \left(\nabla\left(\frac{p}{\rho} + gy\right)\right) = 0 \qquad \text{Eqn 4.6}$$

The inertia term $\vec{V} \cdot \nabla \vec{V}$, can be rewritten as:

$$\vec{V} \cdot \nabla \vec{V} = \frac{1}{2}\nabla(\vec{V} \cdot \vec{V}) - \vec{V} \times (\nabla \times \vec{V}) = \nabla\left(\frac{V^2}{2}\right) - \vec{V} \times \vec{\varpi} \qquad \text{Eqn 4.7}$$

Where $V^2 \equiv \left|\vec{V}\right|^2 = \vec{V}\cdot\vec{V}$, and then the second term on the left side can be rewritten as:

$$\nabla\times(\vec{V}\times\nabla)\vec{V} = \nabla\times\nabla\left(\frac{V^2}{2}\right) - \nabla\times\left(\vec{V}\times\vec{\varpi}\right) = \nabla\times(\vec{\omega}\times\vec{V}) \qquad \text{Eqn. 4.8}$$

The vorticity equation can be obtained and written as:

$$\frac{D\varpi}{Dt} = \left(\omega\cdot\vec{\nabla}\right)\vec{V} + \nu\nabla^2\vec{\omega} \qquad \text{Eqn. 4.9}$$

From Figure 4.9 the highest amount of vorticity occurs during diastole, at which could be due to the dampening of the flow. However, at both systole and diastole the highest vorticity occurs at the wall, which indicated flow reversals. This explains the non-monotonic behavior in the mass concentration profiles.

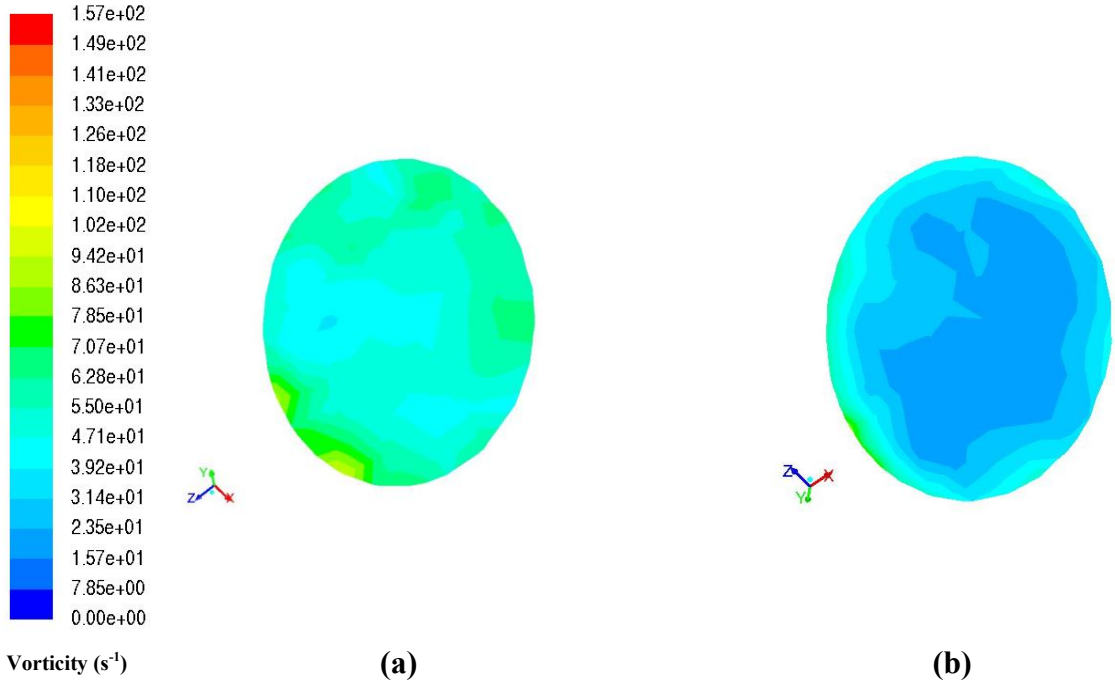

Figure 4.9. Aorta cross-sectional view of vorticity contours at: (a) diastole and (b) systole.

The experimental results have been compared to the experimental results for validation purposes. The key take away from the dye trace study is the experimental and numerical results are within 3 percent agreement (0.3-1s and 1.7-2s) and that the monotonic behaviors of the mass concentration profiles are due to flow reversals. The study above is a direct simulation of intra-arterial injection where a catheter is placed in the artery. Figure 4.10 provides a contour plot at discrete time intervals to provide an illustration of the drug trajectory path and transit time during the cardiac cycle.

From Figure 4.10, the dye enters the ascending aorta through the aortic valve at time t=0.0s. The flow appears to be purely convective. The parameter that describes the convective dominance of the flow is the Peclet number. The Peclet number equation is described earlier in Eqn 4.1. The minimum Peclet number for the flow is whereas the maximum is. The minimum and maximum Peclet number is described by the peak of the cardiac cycle. From Figure 4.10, after the dye enters the aorta, the dye reaches the descending aorta around 4.5s and then reaches the femoral section around 11.6s. The dye does not start traveling up the common carotid artery until around 29.6s. Ultimately, the flow of the dye is focused from the aorta to the femoral section. The flow diverts later into the branching networks after flow has reached the femoral sections. This is important because if a drug is injected into the cardiovascular system and has a specific target sight, it is important to know where the drug will go and how much of that drug will divert. Also as shown in Figure 4.10, the time that it takes for the dye to enter the upper (cranial) part of the phantom is much longer than it take for the dye to travel around the aorta to the descending aorta. This is due to the centripetal forces that occur around the bend of the aorta. These forces, force the dye to accelerate around the aorta curve which creates the unsteadiness as

shown in the monotonic trend of the mass concentration curve and the rapid transport of dye to the descending aorta.

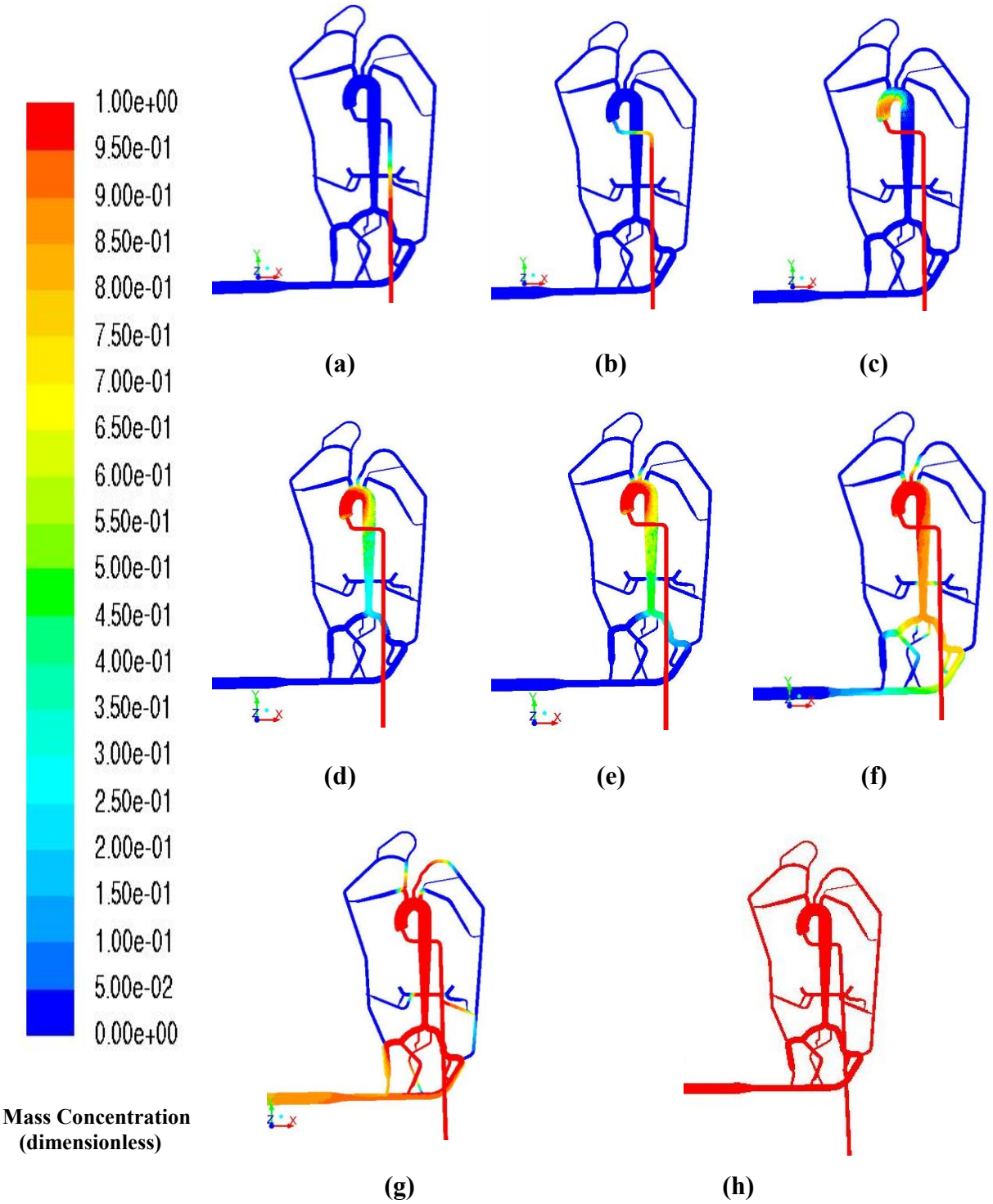

Figure 4.10. Dye mass concentration at time: (a) t=1.75s (b) t=2.1s, (c) t=4.5s (d) t=11.6s (e) t=15.1s (f) t=29.6s (g) t=94.6s, and (h) t=150s.

Clinical studies may find studies such as these useful to find approximate time frames of drug delivery and the trajectory path of the drug from the point of injection. Due to the fact that in the cardiovascular system there are many curves and bends that the drug can take route to, clinicians may need to know where exactly the drug may go after injection. Another study that may find this useful is medical implants that disperse drugs into the arterial system. The next section presents a study on the aorta and carotid artery using particle imaging velocimety (PIV).

4.3 Aorta and Carotid Artery PIV Studies

The present study also examines the hemodynamic parameters of flow in the aorta and carotid artery during rest cycle using PIV. The aorta and carotid artery geometry was reconstructed using the same process outlined in Chapter 3. The geometry used to construct the aorta and carotid artery part of the phantom is from a 28 year old patient. The purpose of this section is to address the flow patterns and magnitude of wall shear stress present in the aortic section during the rest state cycle. The carotid artery is branched from the CCA branch of the aorta. Although the geometry used is from a 28 year old patient, the geometry can be modified to simulate diseased and non-diseased cases as shown in the previous section. The aortic section of the cardiovascular system is considered to be the main branch/vessel responsible for delivering blood to the entire cardiovascular system. In most cases, the aorta is the first section that experiences a buildup of plaque and/or rupture. The buildup of plaque in any artery reduces blood flow throughout the system which in turns reduces the level of oxygenated blood to the brain. Aortic rupture or aneurysm is also another effect of plaque buildup. Aortic aneurysm is a pathological enlargement of the aorta area taking the fusiform shape and may extend to neighboring arteries. The mortality of this pathology is high in elderly patients (15% for

ruptured aneurysms), and the current standard of determining rupture risk is based on anteposterior diameter. The high increase of wall shear stress also plays an important role in the health of arteries and cardiovascular system. High levels of wall shear can lead to blood cell lysising or endothelial rupturing. Extremely low levels of wall shear can lead to endothelial cell death. The study begins with flow in the carotid artery. Figure 4.11 present an image of particulates dispersed in the flow through the carotid artery for PIV analysis. The arterial model shown is a glass model and the analyses are conducted from a single unit rather than from a full cardiovascular system.

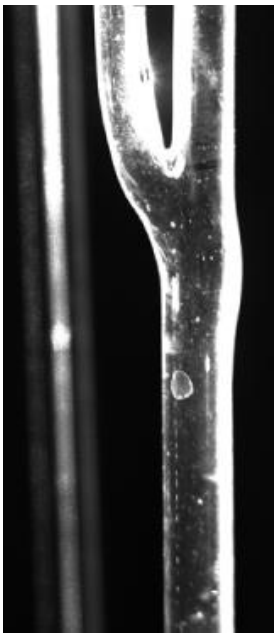

Figure 4.11. Photograph of particulates dispersed in carotid artery flow field.

Figure 4.12 presents the velocity contours at 3.2 s and 3.5 s. As shown in Figure 4.12, the highest magnitude of velocity is present in the bifurcating region of the CCA. There are also period where the flow dampens and accelerates which is due to the fluctuations and harmonics produced by the heart valve.

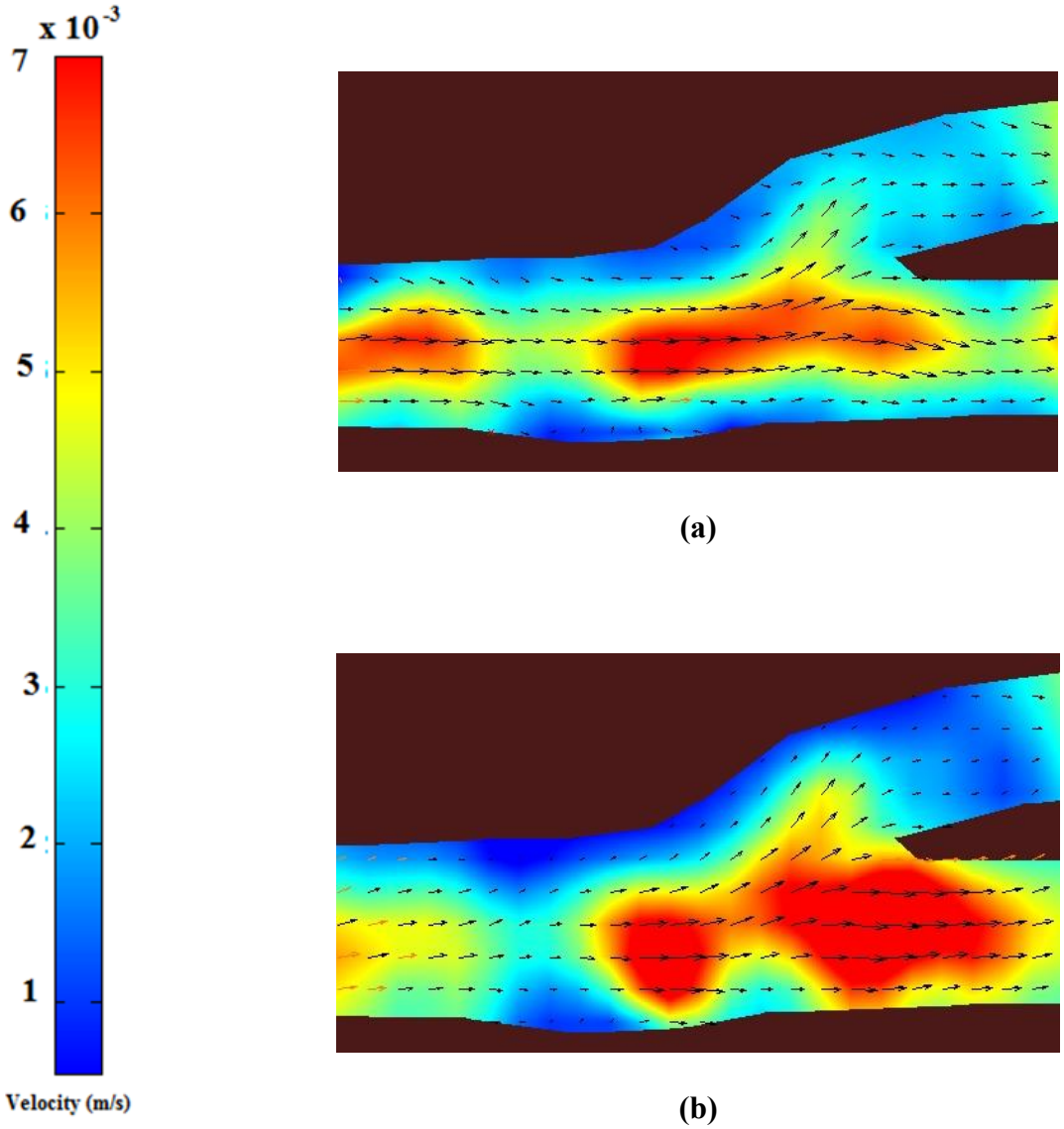

Figure 4.12. PIV carotid artery velocity contour plots at time: (a) 3.2 and (b) 3.5s

Figure 4.12 presents the velocity waveforms of the carotid artery during rest state cycle at 3.2 and 3.5s. Figure 4.12a presents the velocity waveform at 3.2s and Figure 4.12b at 3.5s. The centerline velocity at 3.2s is 0.0045 and 0.004 at 3.5s.

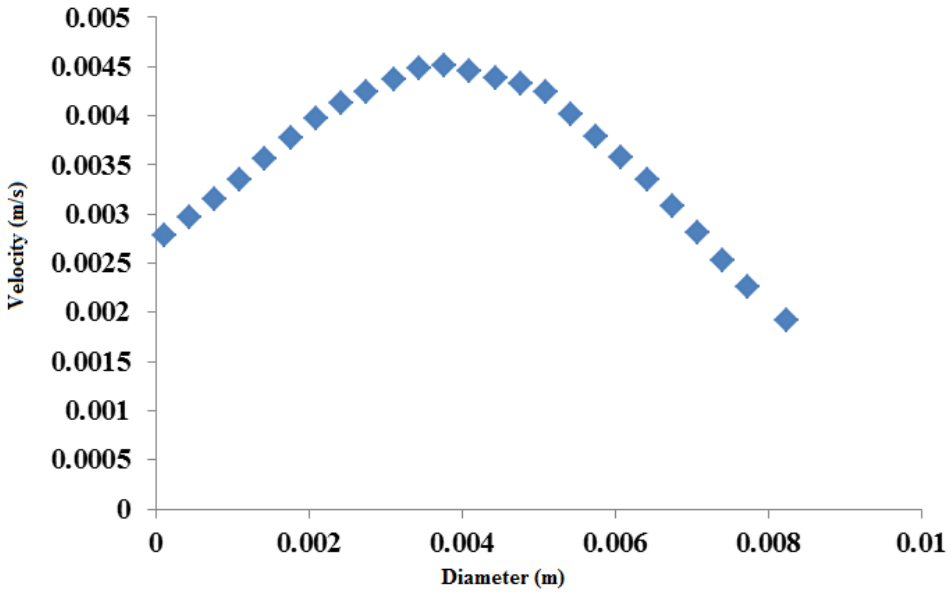

(a)

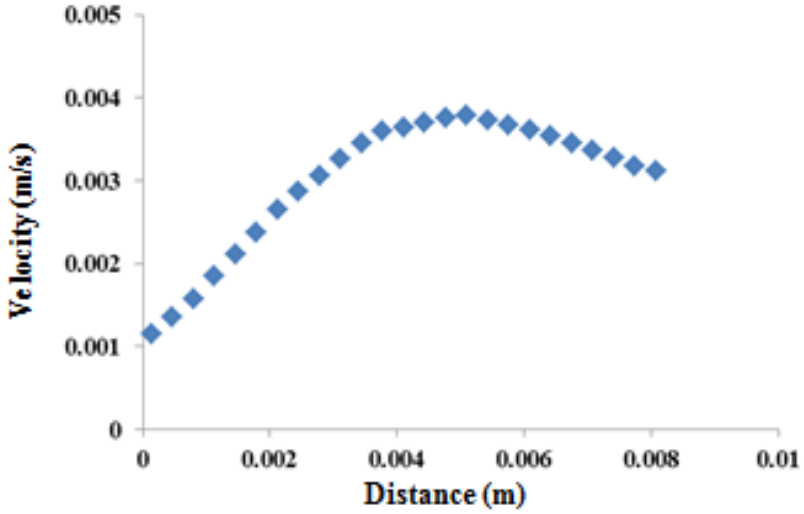

(b)

Figure 4.13. Carotid artery velocity waveforms extracted from PIV experiments at: (a) t=3.2s and (b) t=3.5s.

As shown in both Figure 4.13a and 4.13b, the no slip condition is not captured due to the glare in the wall from the PIV lighting. The hemodynamic parametric results of the aortic section of the cardiovascular phantom are also discussed. Figure 4.14 shows a velocity contour and vector plot

of the aorta. The contour plots contain a region of interest area (ROA) that focuses on the area after the arch which is the descending aorta. The scale of the velocity magnitude is from 0 to 0.9 m/s with the color scale ranging from blue being 0 m/s and red being 0.9 m/s. As shown in Figure 4.14, the velocity magnitude distribution/profile appears to be uneven about the centerline of the aorta. This profile continues further down from the ROA site. However when approaching the arch area near the aortic valve, the largest magnitude of velocity occurs near the centerline. The largest magnitude of velocity occurs near the outer wall of the aorta near the descending aorta region. Although there are areas of high velocity approaching the wall, the no-slip condition is captured at the outer wall. In Figure 4.12 highlights this phenomenon more clearly.

Figure 4.15 contains a plot of the velocity profile at one location of the ROA site at different time intervals (T). The velocity profiles shown in Figure 4.15 highlight the change in velocity as a function of time. The profiles confirm the uneven distribution of velocity across the diameter of the ROA site. At time T= 3s, the velocity reaches systole which is the peak velocity in the cardiac cycle. The maximum velocity at systole appears to be around 0.5 m/s. However when looking at the velocity contours, the contour highlights sections where the velocity reaches a maximum around 0.9 m/s. The velocity profiles were extracted midway of the ROA site. From the velocity profiles and the velocity contours, a general conclusion can be made that that the velocity profile is not constant along the axial direction of the aorta. This in part could be due to the curves and bends in the aorta that produces vortices and unsteadiness in the trajectory of the flow. This could also be due to the dampening/fluctuations of harmonic from the pump/heart.

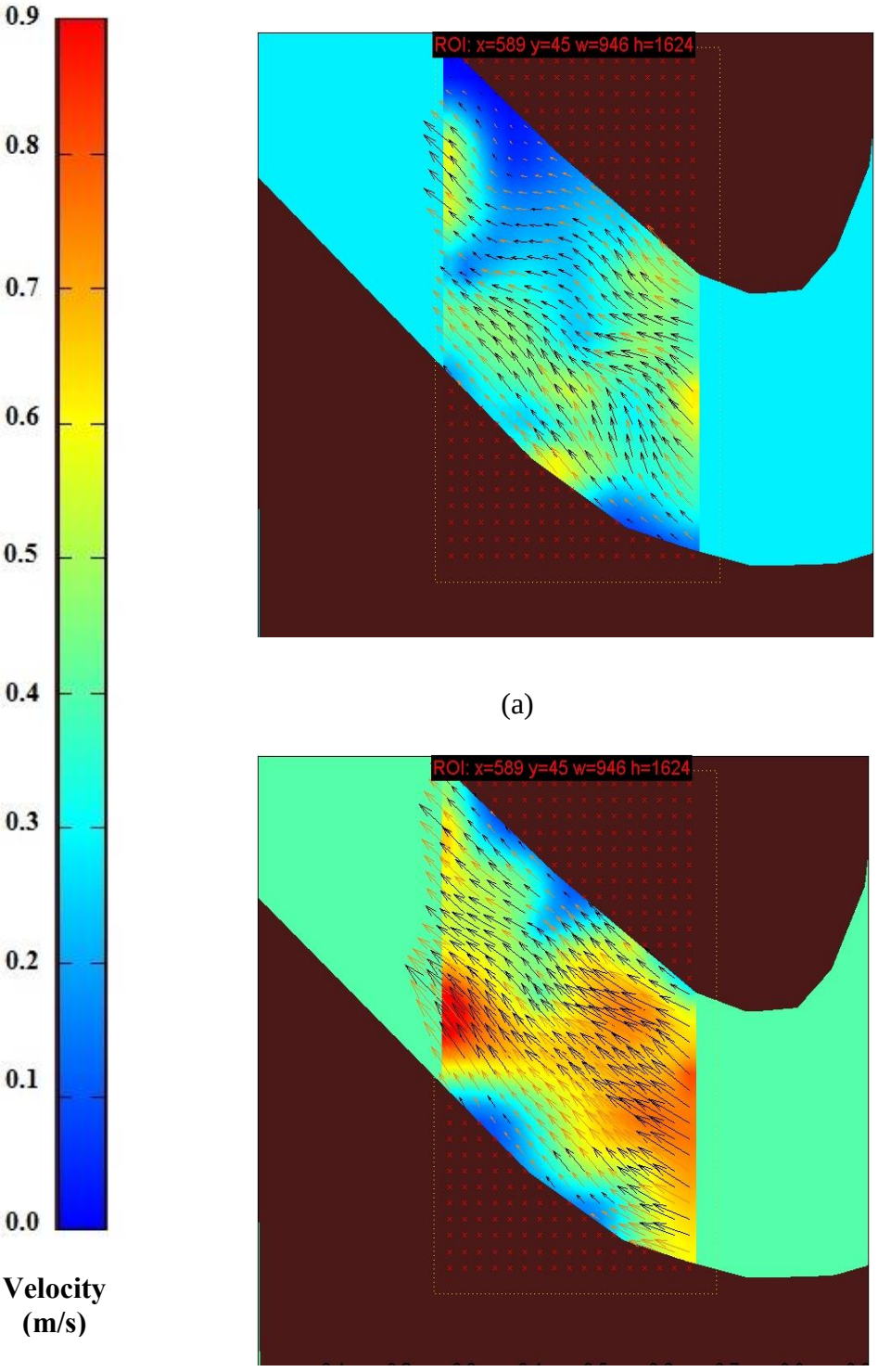

Figure 4.14. PIV velocity contours at: (a) 0.1s and (b) 0.5s

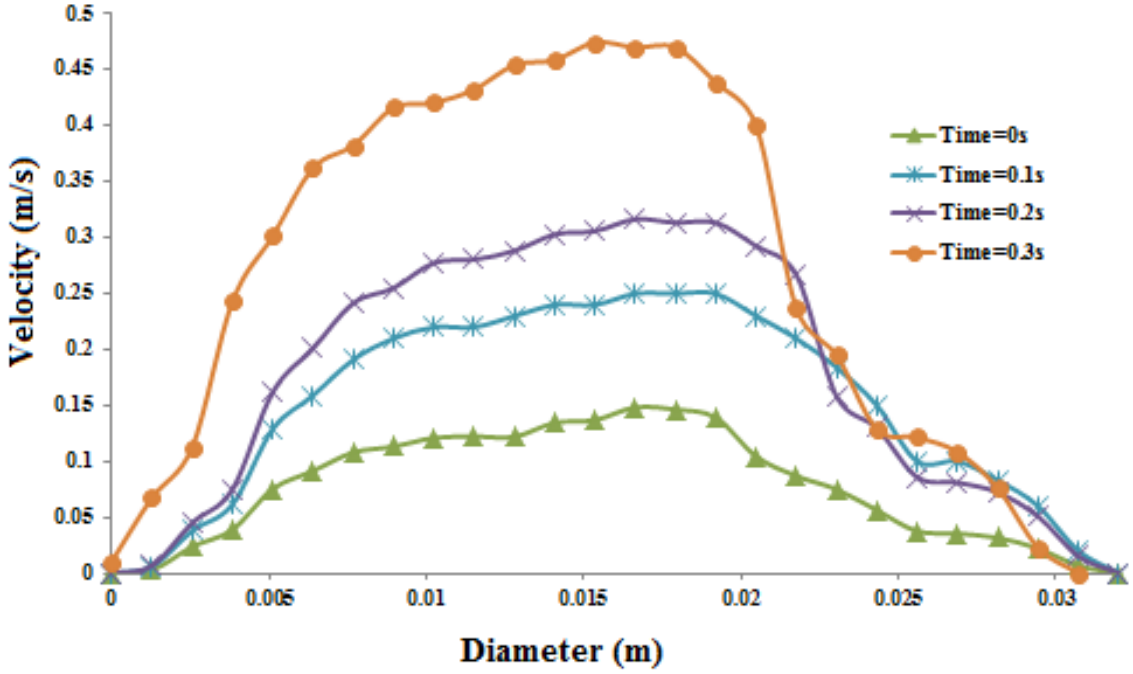

(a)

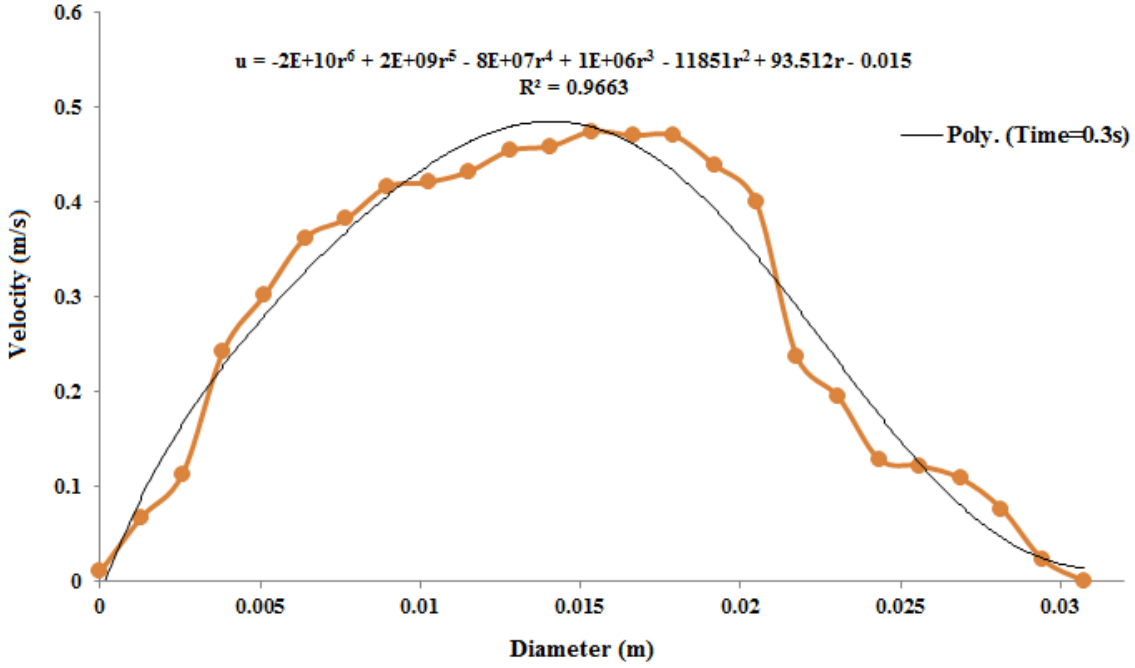

(b)

Figure 4.15. Plot of velocity profile for: (a) different time steps and (b) profile and velocity equation at time T=0.3s.

The velocity contours are also useful because it provides information about the transport of blood. The artery itself contains a lining of cells in the interior core in which the blood is in contact with. The blood feeds nutrients to these cells. It has been hypothesized that the wall shear stress promotes or deters cell growth and maintenance. In actuality, the transport of blood to the artery wall provides the necessary nutrients to the cell lining. From the contour plots, one can see that high levels of transport take place near the wall. Figure 4.16 provides a plot of diameter vs. wall shear stress at systole (time T=3s). The wall shear stress was derived from the velocity distribution. The equation for calculating the wall shear stress is shown below:

$$\tau = \mu \frac{\partial u}{\partial r} \qquad \text{Eqn. 4.10}$$

The derivative of the velocity distribution was taken and multiplied by the viscosity of the working fluid and fitted using the diameter of the pipe. A plot of this is shown below in Figure 4.16.

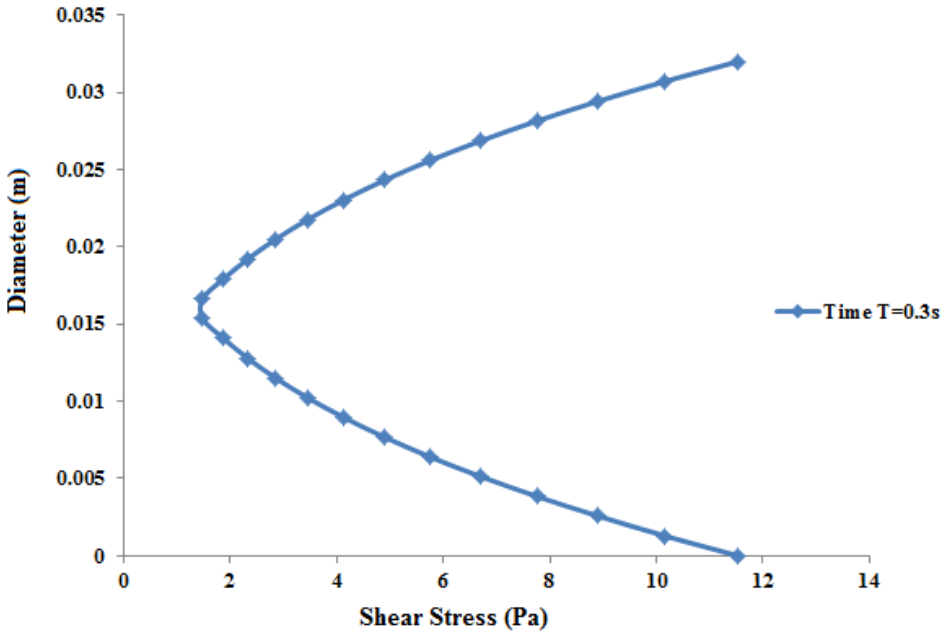

Figure 4.16. Diameter vs. wall shear stress at time T=0.3s.

As shown in Figure 4.16, the minimum wall shear takes place at the centerline which indicates that the gradient is near zero at the centerline. The highest wall shear takes place at the wall. The normal range of wall shear stress in the arteries ranges from 1-12 Pa. The highest wall shear stress occurs during systole and falls within the range of 1-12 Pa. The highest wall shear observed is around 11.8 Pa. Information such as this is useful for predicting cell death, rupture, and buildup of plaque. Compliance is another important parameter in the analysis of cardiovascular disease.

Compliance in the aorta is thought to have a strong role in the progression of cardiovascular diseases. In the present study, compliance is not calculated directly. However the change in diameter is used determine the overall compliant nature of the arterial wall. Figure 4.17 provides a plot of the diameter of the aorta as a function of time during the rest state cardiac cycle. The relaxed diameter (diameter of the aorta with the pump off) is 32 mm. The maximum diameter 34 mm (systole) is and the minimum diameter is 32.9 mm (diastole). The maximum change is diameter is 2 mm and the minimum diameter change is 0.9 mm. The percent difference in diameter change is calculated below using Equation 4.3:

$$\%\Delta d = \frac{|d_1 - d_2|}{\left(\frac{d_1 + d_2}{2}\right)} \qquad \text{Eqn. 4.11}$$

Using equation 4.11, the maximum percent change in diameter is 6% and the minimum is 2.7%. The change in diameter in this case is important because it provides insight on the possibility of aneurysm/rupture. In most cases, the aorta ruptures after severe hardening but can also rupture during cyclic expansion. Also it is evident that the change in diameter promotes additional perturbations in the flow which are mentioned earlier. This is important in cases where CFD is

used for prediction of flow patterns and profiles. Most CFD studies use rigid models that don't capture the full effect of fluid structure interaction effects.

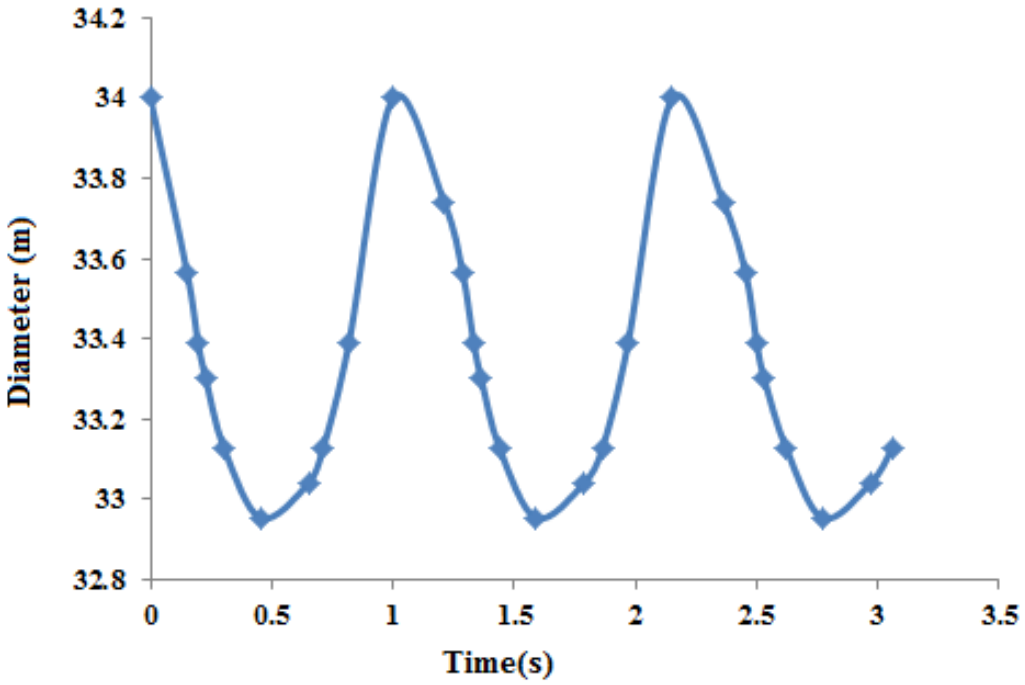

Figure 4.17. Diameter vs. Time for the aorta during rest state cycle.

4.4 Drug Eluting Stent Drug Mass Concentration Studies

In the present study, a drug eluting stent (DES) diffusion time analysis study was conducted. The DES simulations for the present study compare the intravascular drug delivery from a drug coated stent with its coating diffused into the arterial wall. The model developed for drug delivery, the drug internalization rate, interstitial fluid flow, and strut embedment are investigated for their impact on the drug transport and distribution. In the model simulations, a half strut-embedment is considered and the internalization rate and the interstitial fluid flow velocity are both set to zero, for the purpose of comparing with previous modeling work and

examining the impact of individual model factors. As mentioned previously, the plasma flow which is normal to the lumen flow is set to 1E-8m/s. The no-slip condition is specified at the wall. Figure 4.18 shows the velocity contour of the plasma flow into the arterial wall.

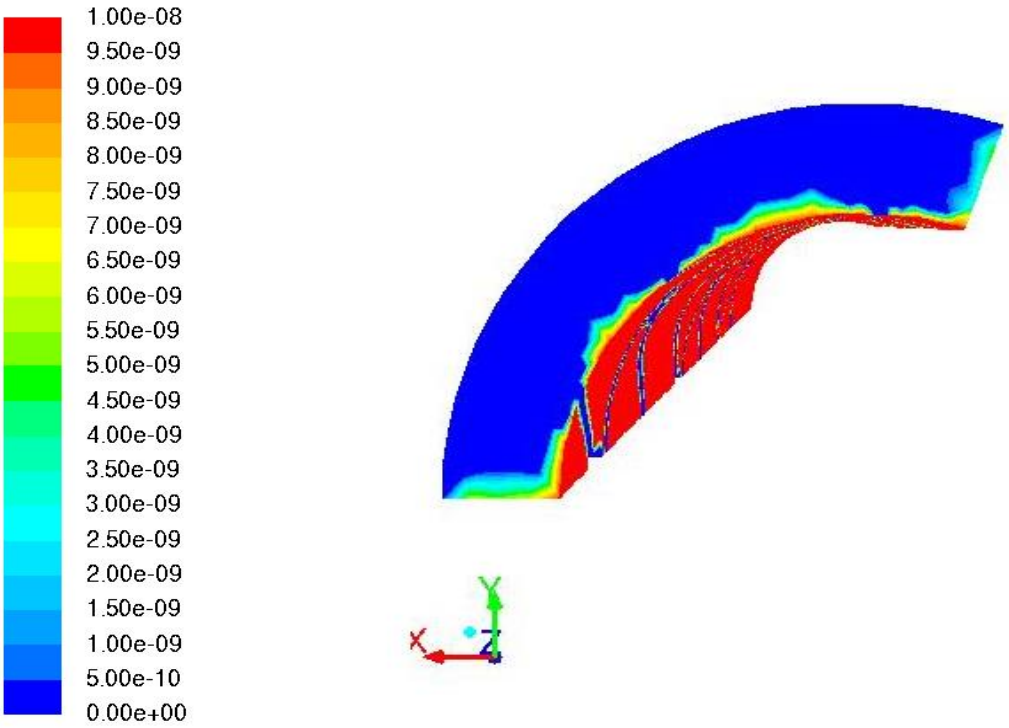

Figure 4.18. Velocity contour of plasma flow into the artery wall.

The simulation results are reported for unbound drug release profiles in the arterial wall. Specifically, the average drug concentration in the arterial wall is defined as the spatial average of the drug. The three means of characterizing the drug delivery process are consistent with other modeling works, while contributing to the possibility for potential comparison with future experimental measurements. In the simulation comparison, the total drug release is achieved in limited drug dissipation, not the plasma flow from the arterial wall. The zero flux boundary

condition is also applied to the left and right boundaries based on symmetry, and at the coating-strut interface. At the coating-arterial wall interface, an equal flux constraint and equal concentration partitioning are applied. For the initial conditions the drug is initially uniformly distributed into the arterial wall as shown in Figure 4.19a and Figure 4.19b.

In observing drug release profiles, from the time of deployment up until the first five days when the degradation and erosion appear to be minor. In the simulation comparison, the drug concentration is around 95% on day 115. Corresponding to the difference in the release profiles, the average drug concentrations in the arterial wall starts off with similar levels for the released drug. The drug concentrations gradients appear very early in the case around day five. The drug level increases as a result of accelerated drug release by degradation and erosion in the coating. The fast increase in drug concentration is contributed by the fast drug clearance rate at the interface. In each case, the trends of concentration evolution for the free drug are highly identical, as a result of the fast reversible binding process in comparison to drug diffusion.

The drug distribution is close to uniform in the circumferential direction (x-direction) as shown in Figure 4.19 c, d, and e, whereas in the transmural (z-direction) direction a gradient is clearly observed closer to the perivascular interface. Upon close inspection, minor asymmetries in the concentration profiles can be observed in Figure 4.19 e, f, g, and h. This is not numerical error but occurs because of slight differences in the volume of tissue proximal and distal to the stent after deployment. The stent was centered with respect to the axial direction before deployment. This symmetry was broken during deployment because of stent foreshortening. While these asymmetries are noticeable, they are not significant enough to affect the interpretation of the parametric studies. It is even more visible in Figure 4.20. A measurement line was drawn on the arterial wall in the longitudinal direction to capture the effects of drug

concentration of the wall. The better uniformity in the circumferential direction is expected with the aniostopic drug diffusivity which results in fast drug diffusion in the circumferential direction. The observed arterial drug distribution patterns appear to have nonlinear trends in drug concentration distributions from.

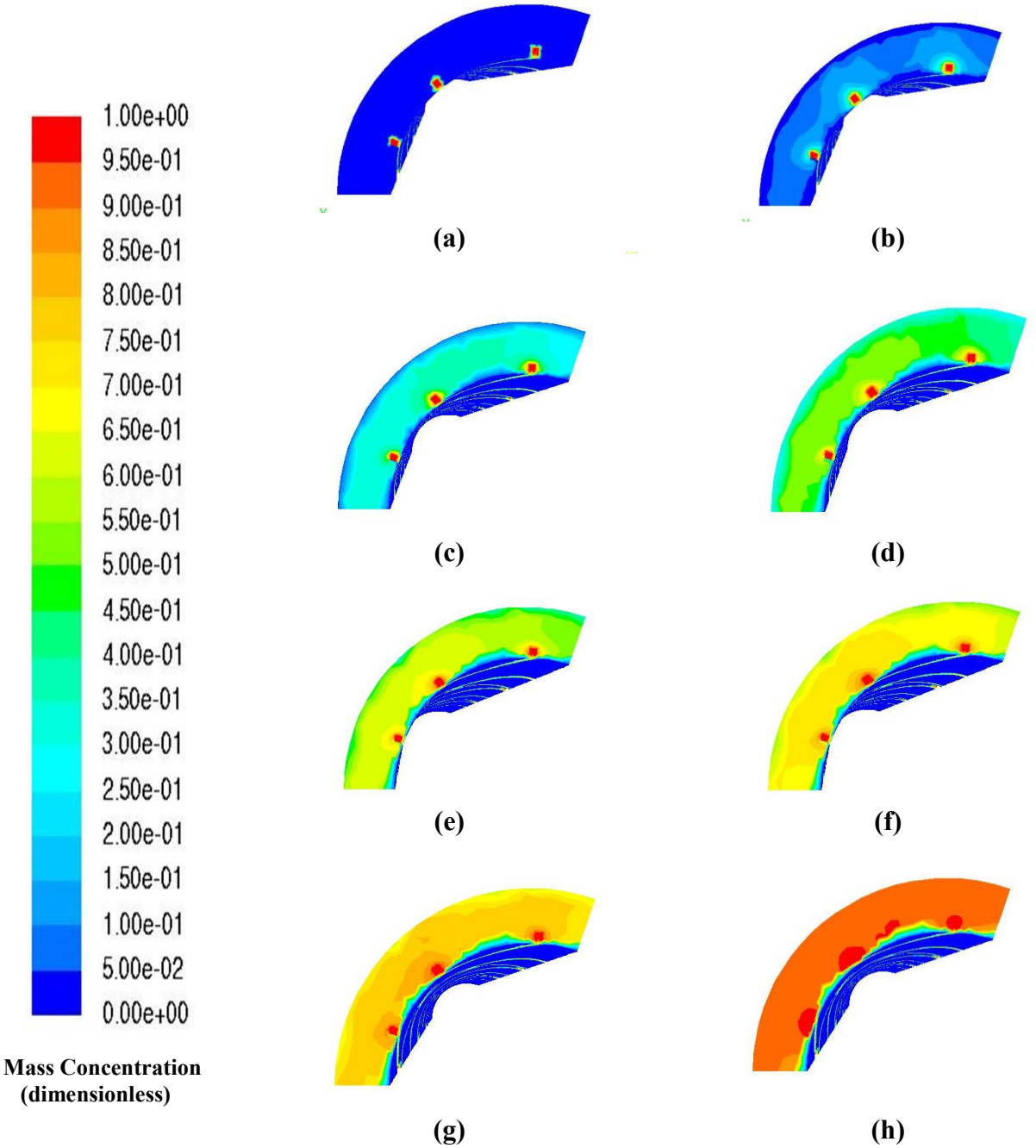

Figure 4.19. (a) 5 days, (b) 15 days, (c) 25 days, (d) 35 days, (e) 45 days, (f) 55 days, (g) 65 days, and (h) 115 days.

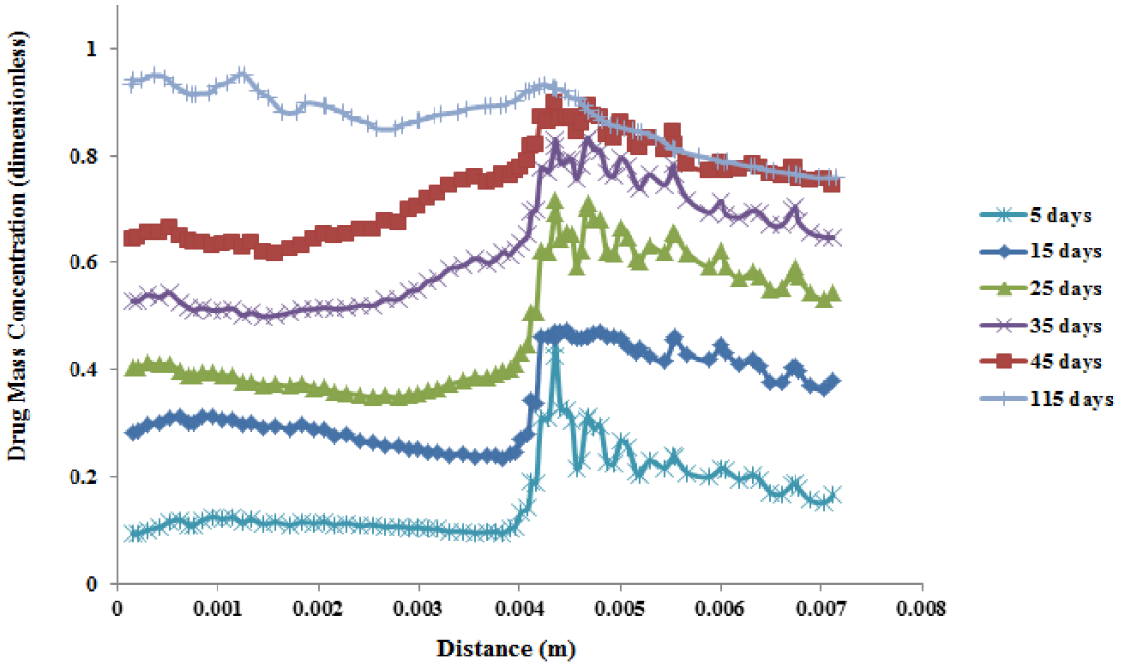

Figure 4.20. Drug concentration vs. distance for DES analysis.

Figure 4.20 reveal how the deposition patterns tend to follow the pattern of the stent struts and how the drug is able to penetrate deep into the vessel wall. Figure 4.20 also shows a trend that shows that the concentration profile from strut to strut becomes more steep and linear as time progresses. The profile becomes more linear near day 45. For this particular case, the drug used diffuses completely around 3.5 months. A drug release profile study was also conducted on the entire cardiovascular system using CFD.

4.5 Evaluation of the Effect of Patient-Specific Geometry on Hemodynamic Flow

In the present work, CFD analyses were performed on a simplified carotid bifurcation arterial geometry and two patient-specific carotid bifurcation arterial geometries. The geometries are discretized and used as computational domains. For blood flow simulations, the conventional assumptions: flow in the carotid bifurcation artery is Newtonian, laminar,

incompressible, and isotropic are implemented. By these assumptions, blood can be modeled by the incompressible Navier-Stokes equations with blood density specified as 1060 kg/m^3 and the corresponding dynamic viscosity as 0.0035 kg/m s. The commercial software Gambit^{TM} was used for geometric meshing and FLUENT^{TM} was used to solve the Navier-Stokes equations in the finite volume formulation. Equation 4.12 is used to solve the fluid flow equations in the finite volume form.

$$\rho\left(\frac{\partial v}{\partial t} + v \cdot \nabla v\right) = -\nabla p + \mu \nabla^2 \qquad \text{Eqn. 4.12}$$

Two CFD analyses were conducted. The first analysis was conducted with a simplified sinusoidal velocity waveform which simulates a rest-state cycle. The rest-state cycle is implemented as a boundary condition at the inlet of the CCA branch of each arterial geometry. The first analysis compares the magnitude of hemodynamic parameters in a simplified arterial geometry and two patient-specific geometries and compares the efficacy of modeling simplified geometries as opposed to patient-specific geometries. The second analysis implements two patient-specific velocity waveforms, one at rest-state and exercise and compares the magnitudes of hemodynamic parameters at both rest state and exercise. The second analysis also compares the efficacy of modeling patient-specific geometries over simplified geometries. For both analyses, the ICA and ECA outlets were modeled as pressure outlets at 12 kPa (90mmHg). A grid independent study was conducted prior to assessing the hemodynamic results. Grid meshing levels were performed at three levels: coarse (104,406), coarse (143,948) and medium (233,045) and it was determined when evaluating wall shear stress and pressure that the CFD results were no longer depending on the size of the mesh at 233,046 cells. Table 4.3 show the grid independent study data.

In comparison of the velocity at the ICA for geometric models, a 0.21% difference in velocity was observed for a grid independence study. For numerical solutions, the velocity coupling solving technique was implemented. The WSS vectors are predicted on fluid domain surfaces that represent the interface boundary between the fluid and the neighboring tissue. For analyses, the WSS are calculated using Eqn 4.13. Velocity is monitored at the CCA, ECA, and ICA and vorticity is calculated at the sinus bulb. CTA images of stenosed carotid bifurcations were taken from a 50 and 66 year old male and were processed in Solidworks. Figure 4.21 presents a schematic diagram of the Solidworks processing methodology. The parametric data of the patient-specific carotid artery geometries (CA-1) and (CA-2) is provided in Table 4.3. Simulations and analyses were performed for three geometries, the simplified carotid bifurcation arterial geometry (SA-1) and two patient-specific carotid bifurcation arterial geometries (CA-1) and (CA-2). For the second analysis, SA-1 geometry is replaced with a second simplified geometry that resembles a patient-specific geometry. The simplified geometry used in the second analysis contains the same diameter for the CCA, ICA, and ECA as in patient-specific geometry (CA-1). The difference however is that the diameters are constant on all branches as opposed to a variation in diameter along the centerline of the branch.

Table 4.3

Patient-specific carotid bifurcation geometry parametric data.

Parameters	**Carotid Bifurcation Model**	
	Model CA-1	**Model CA-2**
Age	66 year(s)	60 year(s)
Sex	Male	Male
Side	Left	Left
Basis of disease	Atherosclerosis	Atherosclerosis
Direct cause of death	IMA	Aneurysm
Diameter of CCA	7.475 mm	7.725 mm
Diameter of ECA	5.35 mm	5.0 mm
Diameter of ICA	8.0 mm	6.075 mm
Diameter of Carotid Sinus	5.7 mm	7.6 mm
Branch angle between CCA and ICA	45 degrees	29.5 degrees
Branch angle between CCA and ECA	42 degrees	21 degrees

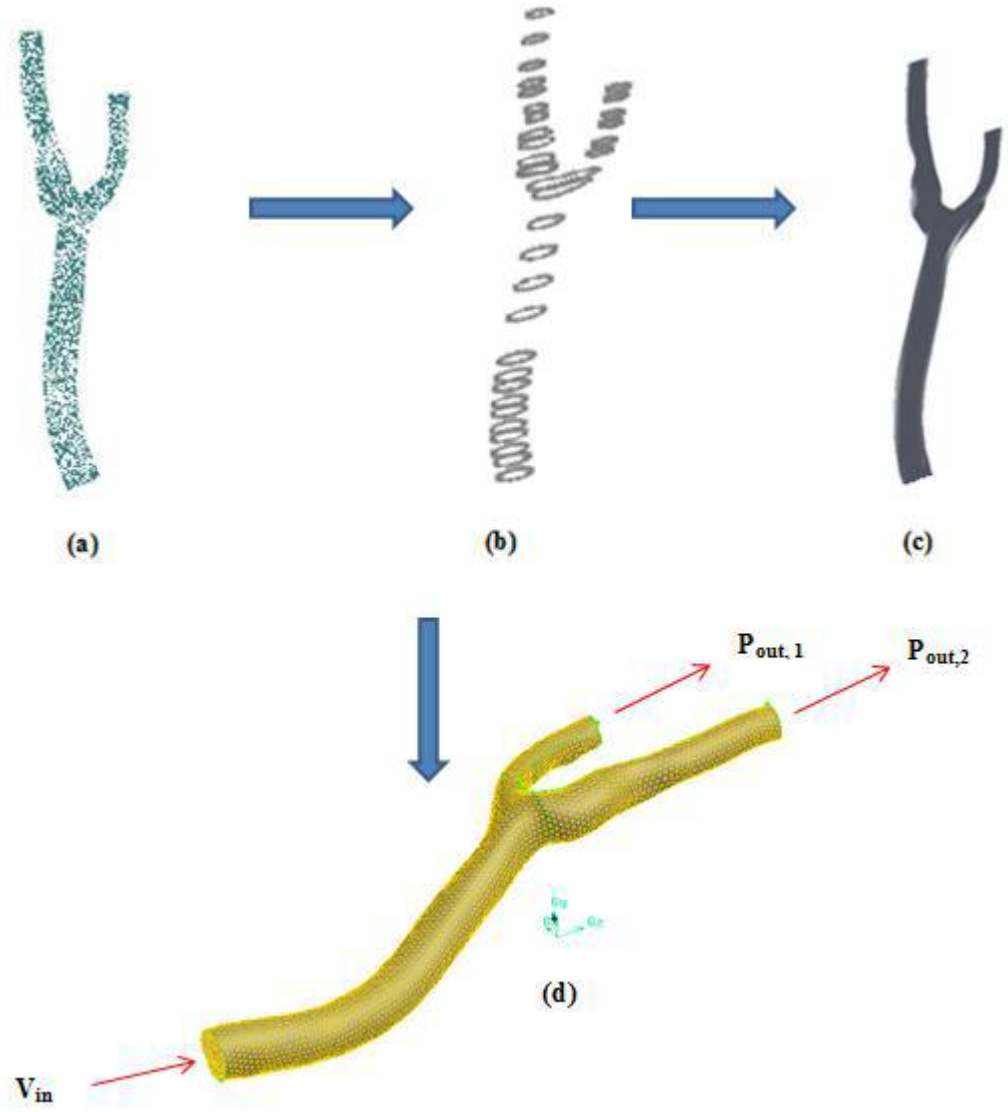

Figure 4.21. (a) CTA scan point cloud image, (b) 3D spline surface generation, (c) lofted and boundary base solid part model of the carotid bifurcation, (d) meshed post-processed carotid artery geometry.

Figure 4.22 shows a CAD drawing of both arterial models. The location of the sinus bulb was monitored for calculating WSS and vorticity as a function of time. Previous studies have suggested that vortictity measurements are predictors of flow disturbances which in turn produces high levels of shear and promotes the onset of shear licensing and or rupture of the vessel lining. Velocity has been calculated throughout the CCA, ECA, and ICA of the simplified

arterial geometry and patient-specific arterial geometries at any point in time. Figure 4.23 shows the velocity waveform monitored at the ICA outflow of the three geometries at time 0s to 3s. At the beginning of the cycle, the blood flow rate starts increasing and reaches a maximum level around 0.45s and then decreases to the lowest level at 1.3s. Figures 4.23 present a plot of the vorticity vs. time for the SA-1, CA-1, and CA-2 geometries.

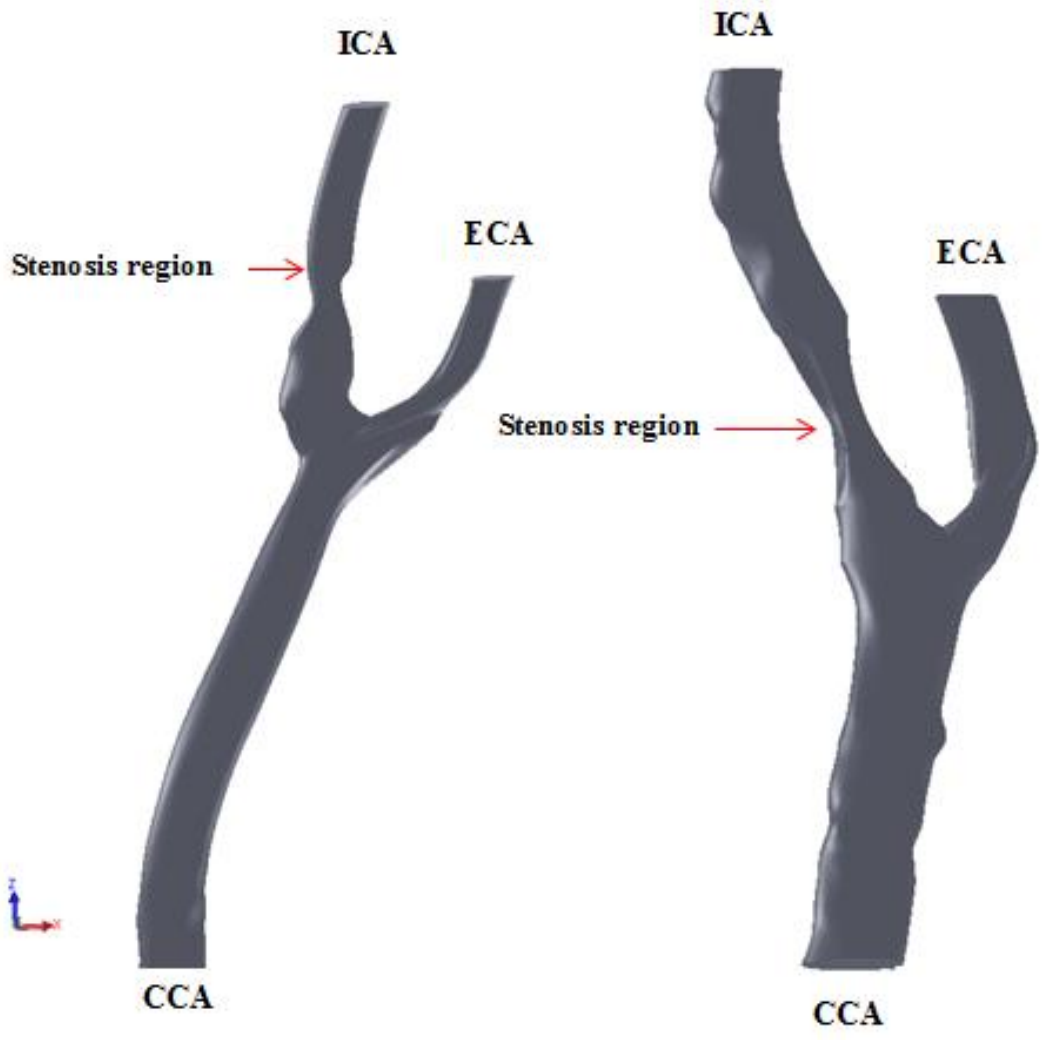

Figure 4.22. CAD drawing of CA-1 and CA-2 bifurcation CFD geometries.

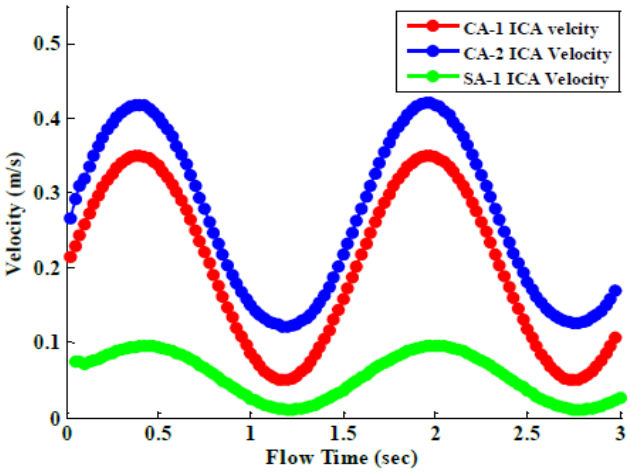

(a)

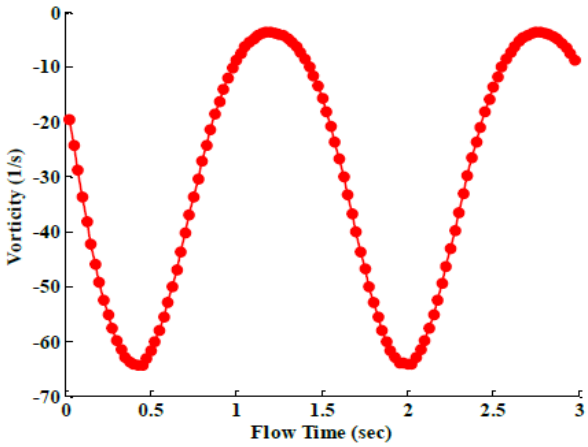

(b)

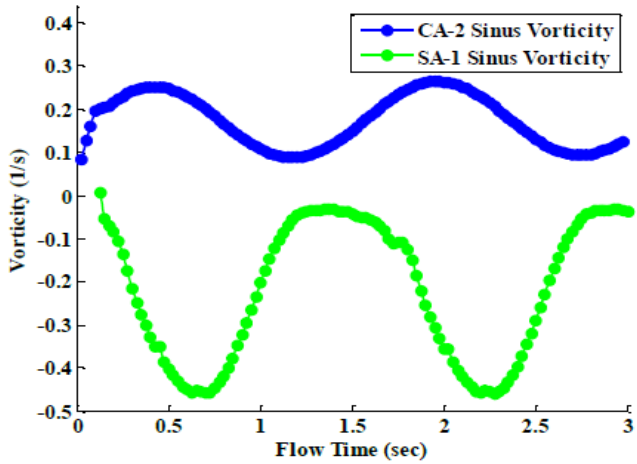

(c)

Figure 4.23. Plot of sinus vorticity vs. time for the CA-2 patient-specific geometry and the simplified arterial geometry SA-1.

Figure 4.24 shows the axial velocity contours of the sinus at time 0.5s (systole), and Figure 4.25 shows the axial velocity contours of the sinus at time 1.0s (diastole).

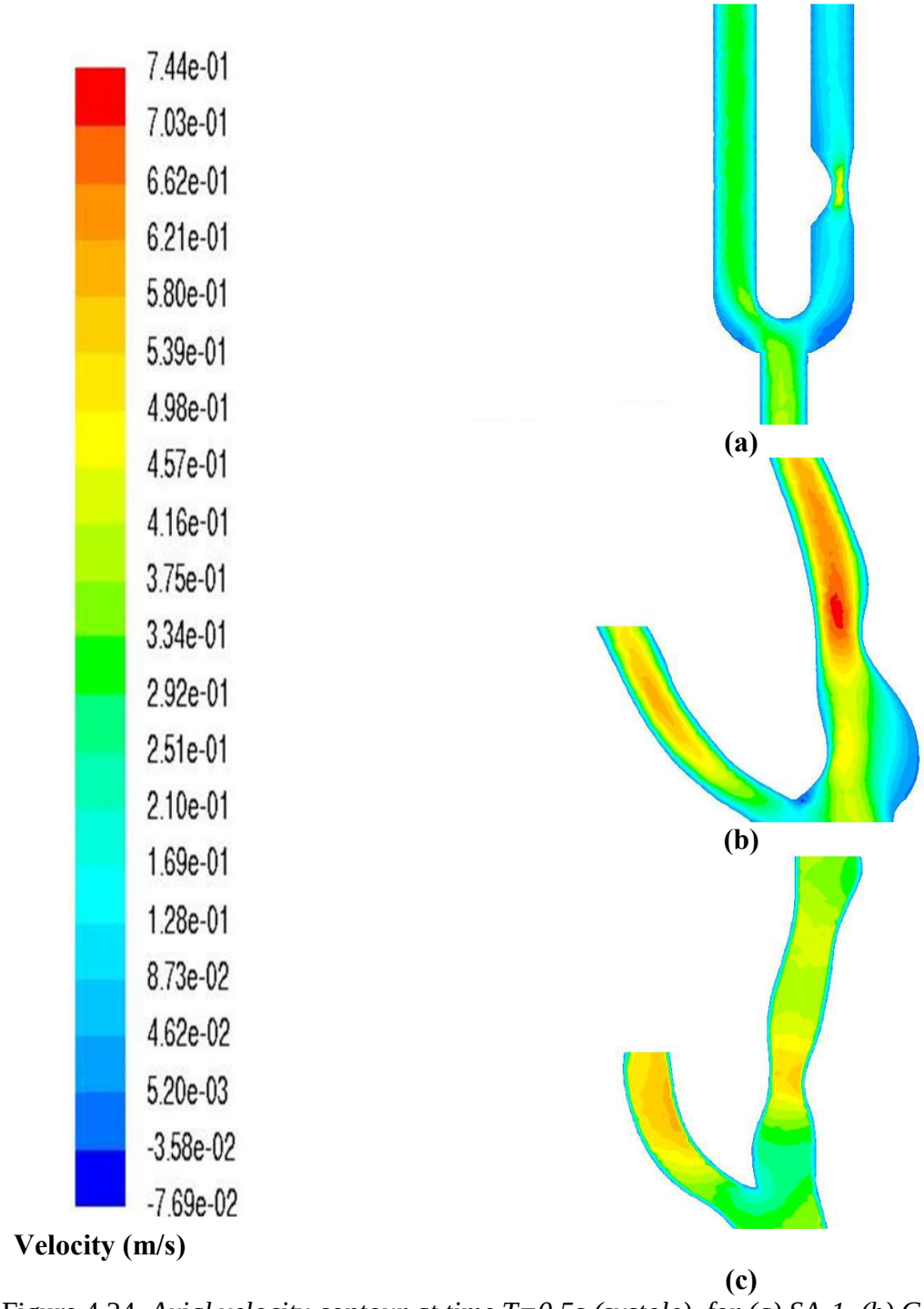

Figure 4.24. *Axial velocity contour at time T=0.5s (systole), for (a) SA-1, (b) CA-1, and (c) CA-2.*

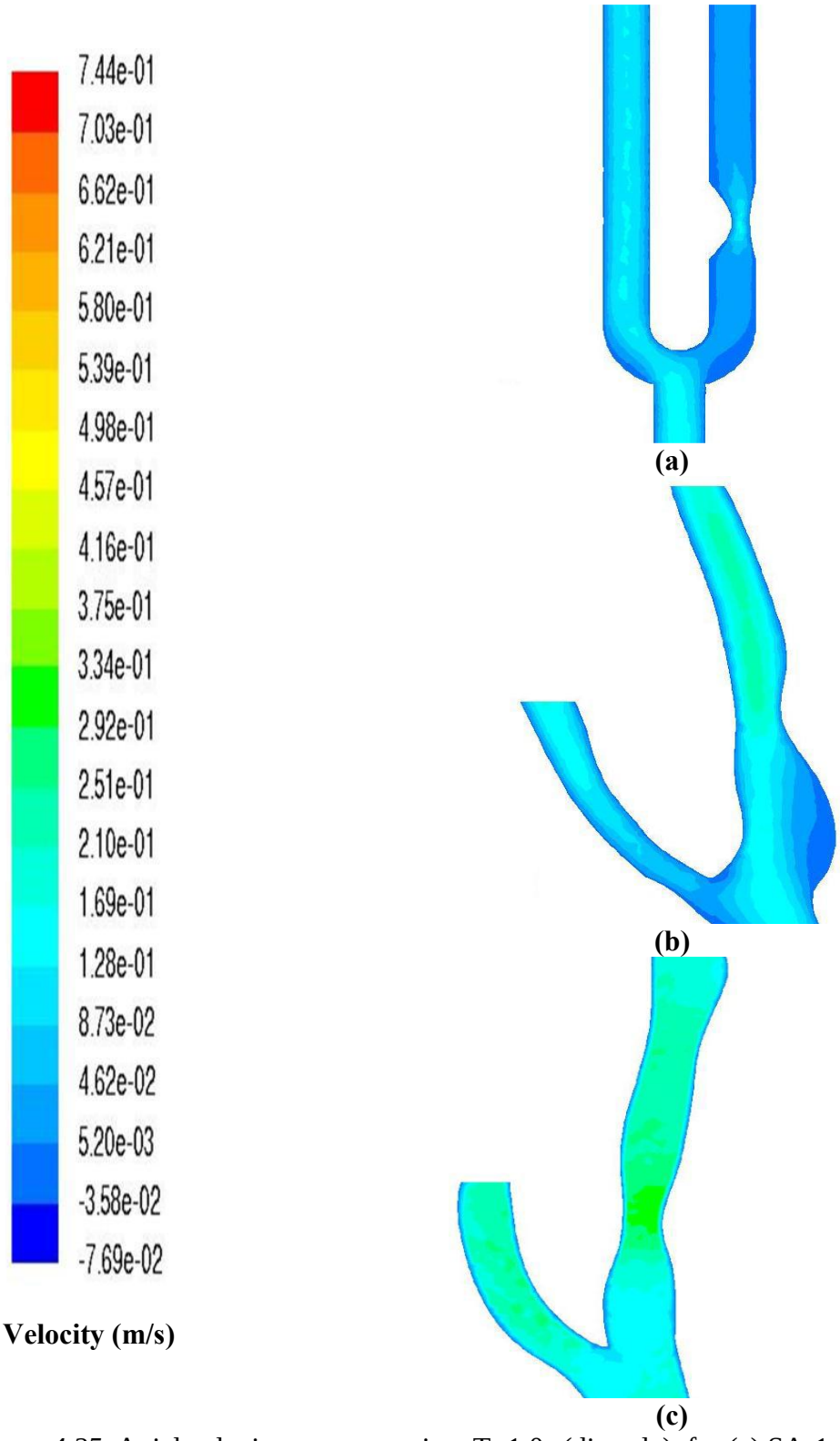

Figure 4.25. Axial velocity contour at time T=1.0s (diastole), for (a) SA-1, (b) CA-1, and (c) CA-2.

The negative velocity indicates flow reversal zones. As shown in Figures 4.24 and 4.25, the maximum flow reversal is observed in the patient-specific geometry models. For the patient-specific geometries, it was also observed that the axial velocity is the highest at the region upstream of the ICA and downstream of the sinus near the CCA. Regions of flow reversal formed near the sinus wall are due to the rapid changes in the flow rate, flow viscosity and the curvature of the sinus. Within these zones, blood flows in the direction opposite to the mean flow increasing the probability of plaque deposition.

For the patient-specific geometries, the velocity gradients near the stenosis are much higher than those near the sinus. The velocity at the sinus becomes negative and indicates flow reversal and very low WSS. WSS is an important factor in the progression and initiation of atherosclerosis. For the simplified geometry, there is a small region of velocity increase at the stenosis, and very little flow downstream of the stenosis to the ICA outlet. The major increase of velocity in the simplified geometry is experienced in the ECA branch of the artery. Figure 4.24 shows the WSS contour for systole (peak velocity) for the simplified arterial model and patient-specific geometries. Regions with WSS less than 0.4 Pa are susceptible to atherosclerosis. In the wall shear stress contours provided in Figure 4.24, it is shown that the maximum WSS experienced is 16.3 Pa. The maximum WSS is shown at the ICA stenosed region of SA-1 and at the stenosis and bifurcating region of CA-1.

A general conclusion from these WSS patterns is that the sinus bulb is the most atheroprone site where higher values of WSS appear at the bifurcation apex and final ends of the ECA and ICA, which have a smaller diameter. There is a stagnation point at the apex because shear directions at its sides are different (granting that the magnitude of the shear would be

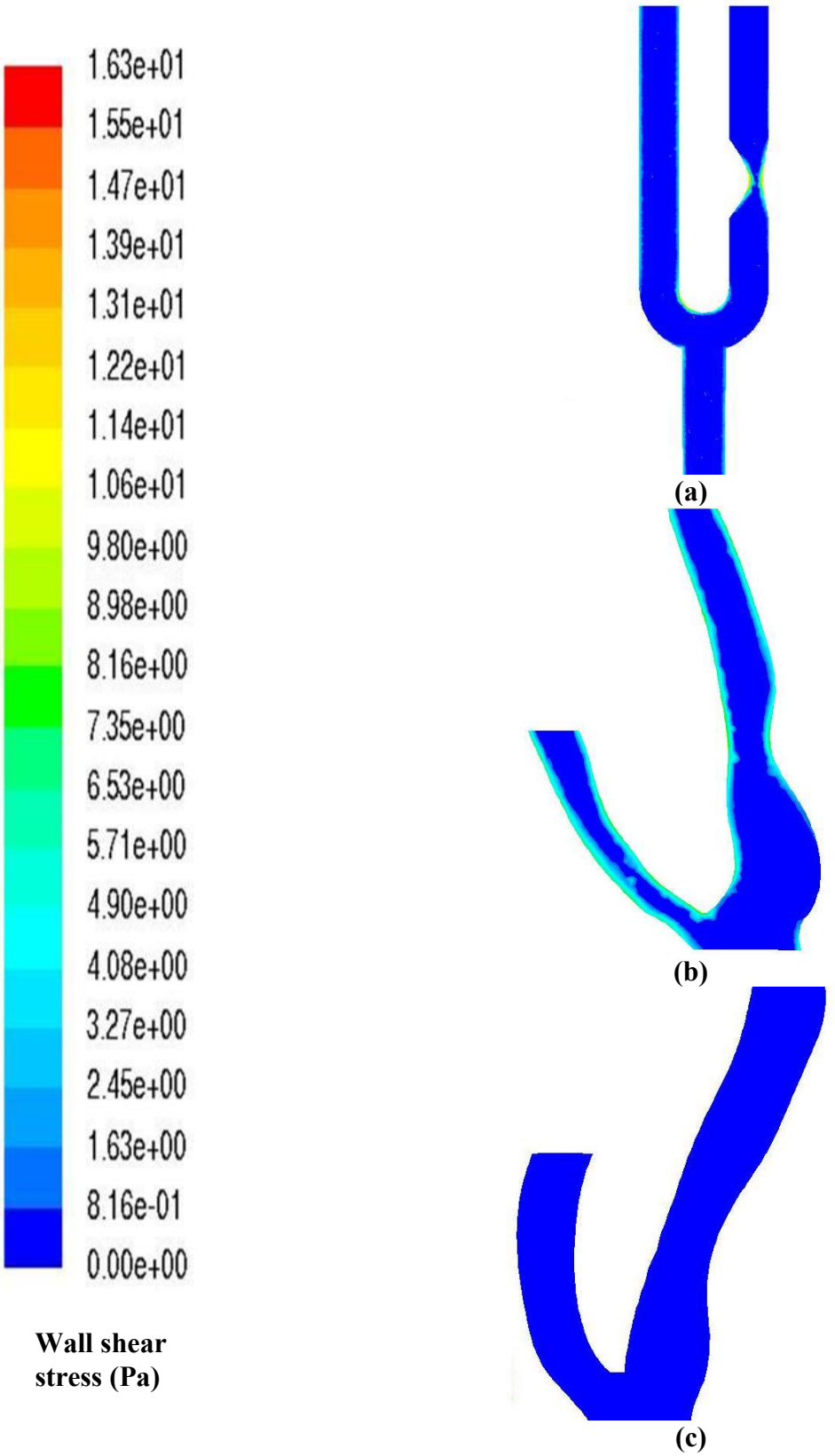

Figure 4.26. WSS contour at time T=0.5s (systole), for (a) SA-1, (b) CA-1, and (c) CA-2.

relatively high). The stagnation point is the place of plaque buildup. Another point is that, in general, realistic geometries have higher values of WSS and the atheroprone site in the sinus bulb is smaller. When considering WSS, the magnitude of the wall shear is a function of the geometry of the arterial vessel. This works proves that when studying hemodynamics of the arterial vasculature, specifically the carotid bifurcation artery for diagnostic purposes, it is important to have patient-specific parametric data for the carotid bifurcation vessel to be analyzed. In addition to geometry comparisons in the efforts of comparing hemodynamic parametric magnitudes, a comparison was also made in studying the effect of patient-specific waveform on hemodynamic parameters.

Pulsatile blood flow during rest-state and exercise were simulated for the three carotid bifurcation arterial geometries, the simplified carotid bifurcation arterial geometry and two patient-specific arterial geometries (CA-1) and (CA-2). As mentioned earlier, SA-1 is replaced with a more realistic geometry. The new SA-1 contains a constant diameter along the centerline of each branch of the artery. From this point, the simplified carotid artery will be referred to as artery "S", the patient specific artery CA-1 will be referred to as artery "A", and CA-2 as artery "B". The volumetric flow rate waveforms used in the present study are aortic artery blood flow rate waveforms during rest-state and exercise. For each case evaluation, fully-developed velocity boundary conditions were imposed at the inlet during steady-state calculations and were iterated until the solution converged and a feasible hemodynamic solution was obtained. After the steady-state calculation converged and feasible hemodynamic solutions were observed, the solver was then switched to transient solver for rest-state and exercise calculations. Volumetric flow rate were calculated throughout the ECA and ICA of the simplified arterial geometry and

patient-specific geometries for two cardiac cycles. Figure 4.27 presents the volumetric flow waveform monitored for two cardiac cycles.

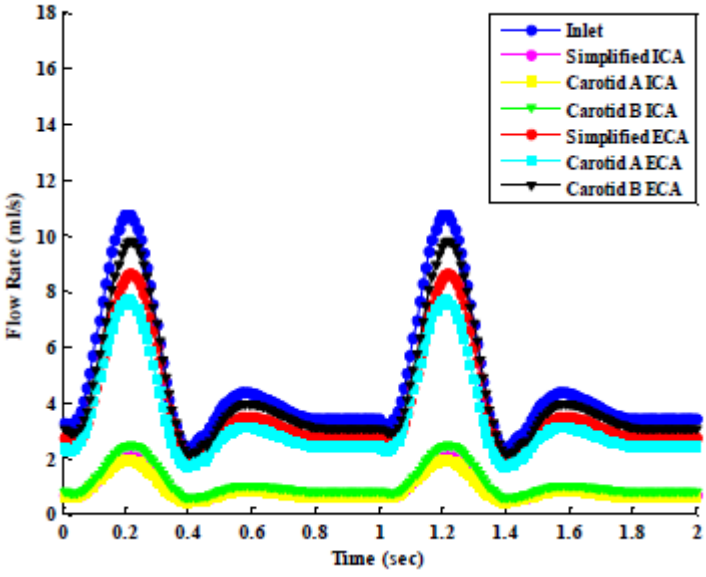

(a)

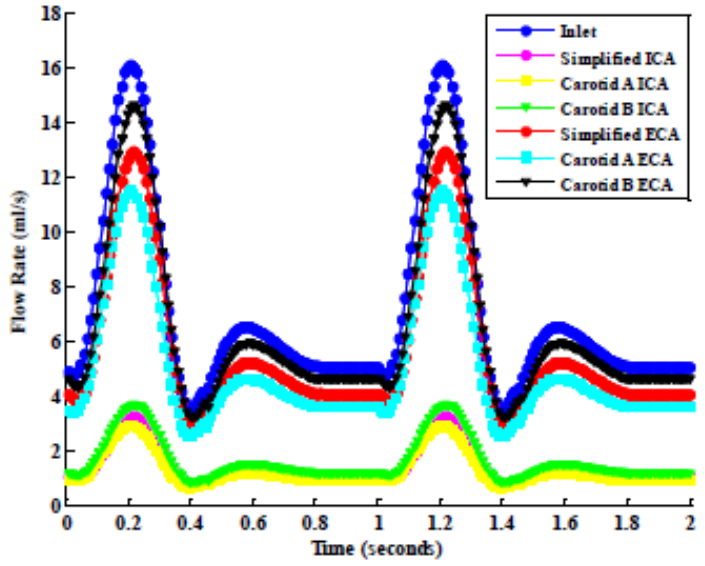

(b)

Figure 4.27. *Volumetric flow rate waveform during: (a) rest-state, and (b) during exercise.*

As shown in Figure 4.27a during the rest cycle, at the beginning of the cycle, the blood volumetric flow rate accelerates and reaches a maximum level around 11.2 ml/s and then decreases and to 1.7 ml/s and then accelerates to 4.2 ml/s decelerates again and remains constant at 3.8 ml/s until the cycles starts over again at 1s. When comparing hemodynamics during the rest-state cycle, for Carotid Artery A, the ICA branch which supplies blood to the brain reaches a maximum blood flow rate of 2 ml/s while the ECA reaches a maximum flow rate of 7.8 ml/s. Similarly, for Carotid Artery B, the ICA branch reaches a maximum blood flow rate of 2.2 ml/s while the ECA reaches a maximum flow rate of 9.8 ml/s. As shown in Figure 4.27b, during exercise, for Carotid Artery A, the ICA branch which supplies blood to the brain reaches a maximum blood flow rate of 3 ml/s while the ECA reaches a maximum flow rate of 11.8 ml/s. Correspondingly, for Carotid Artery B, the ICA branch reaches a maximum blood flow rate of 4 ml/s while the ECA reaches a maximum flow rate of 14.8 ml/s. When analyzing volumetric flow rate for rest-state and exercise, the volumetric flow rate on all outlets for all three arteries increases by a magnitude of 1.5 when switching from rest-state to exercise.

Figure 4.28 presents the average weighted WSS contours during rest-state and exercise. The normal range of WSS in the arteries of a healthy human being is 7-12 Pa during normal activity. The WSS contour snapshots are taken at the highest volumetric flow peak during the cardiac cycle (systole). As shown in Figure 4.28, the simplified carotid bifurcation arterial geometry, denoted at the top of the snapshot by the bold red “s” in a square bracket, appears to have 0 WSS on the ICA branch during systole of the rest-state cycle. However, during exercise, the average weighted WSS on the ICA branch increases to 0.65 Pa. The highest WSS occurs on the CCA branch and ECA branch of the simplified artery. During rest-state the average

weighted WSS on the CCA and ICA is 1.95 Pa, while during exercise on the ECA branch the WSS increases to 9.75 Pa.

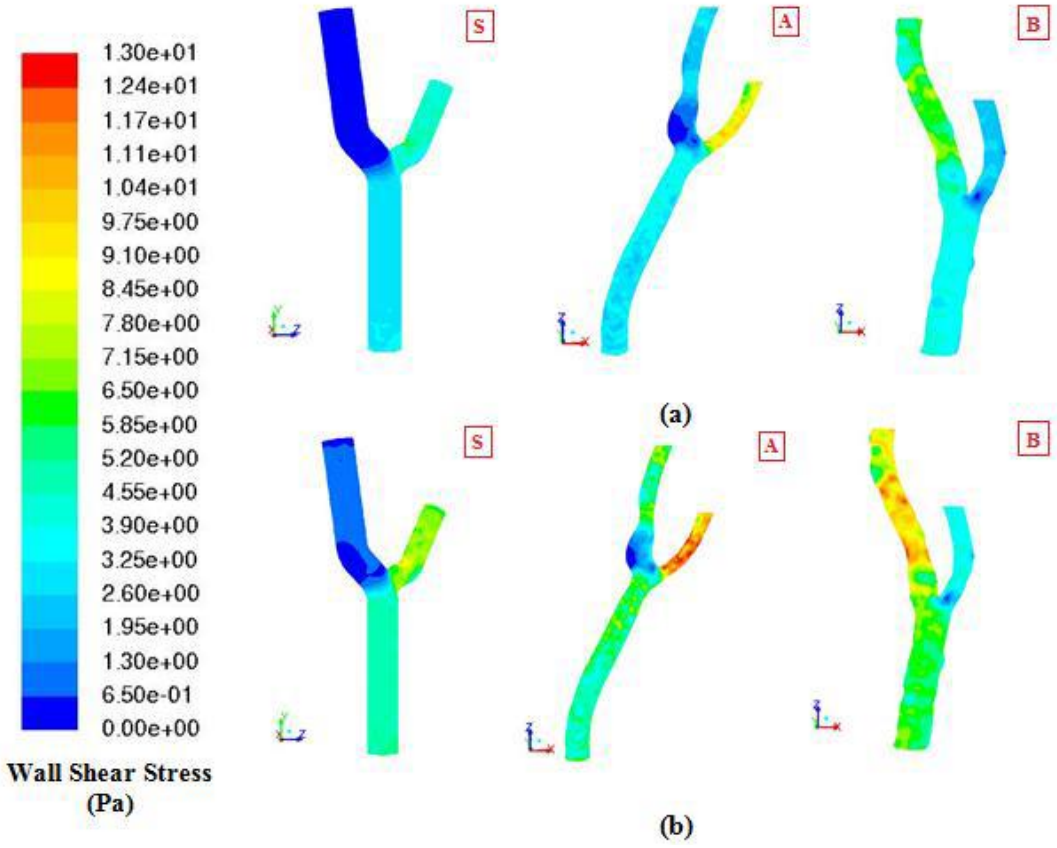

Figure 4.28. WSS contours at systole during: (a) rest-state and exercise.

However for the patient-specific carotid bifurcation arterial geometry A, there is 0 WSS on the sinus bulb during rest-state and exercise. The value of 0 WSS on the sinus bulb indicates that there is no mass transport of blood on the sinus bulb region which also indicates that the sinus bulb will experience endothelial cell death and rupture if there is no transport of blood in that region. From Figure 4.28, the highest WSS that occurs in the patient-specific geometry A during both cycles is 13 Pa and occurs on the ECA branch which feeds blood to the face. For patient-

specific geometry B, the sinus bulb experiences a WSS magnitude of 3.32 Pa during rest and an average of 5.2 Pa during exercise.

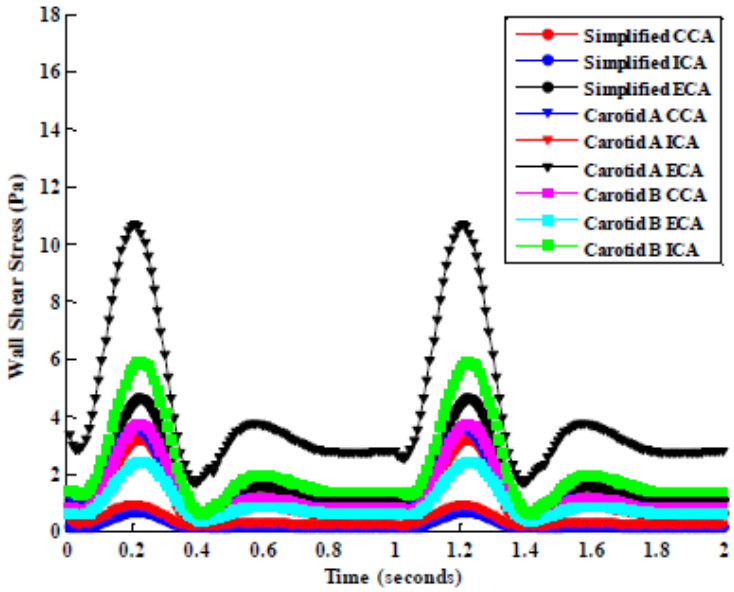

(a)

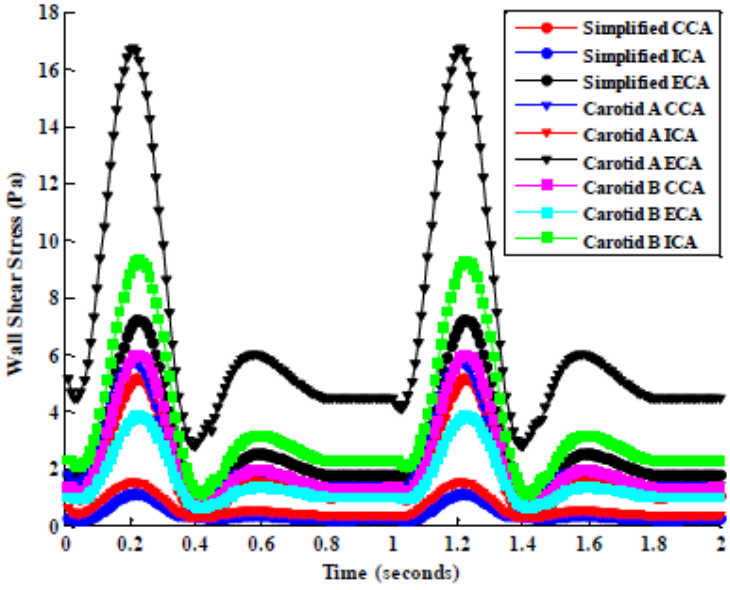

(b)

Figure 4.29. Plot of WSS vs. time systole during: (a) rest-state and exercise.

However as shown in Figure 4.29, the ECA branch of Carotid B reaches a maximum average weighted WSS of 4 Pa during exercise, while the ICA reaches a maximum of 9 Pa. Figure 4.29 also shows that Geometry A experiences the highest peak of WSS of 17 Pa on the ECA branch. This is due to the highest magnitude of flow taking place on the ECA branch. The cross-sectional area of the ICA branch on geometry A is much smaller than the ECA, and due to continuity, the flow is accelerated on the ECA branch which has a larger cross-sectional area. Figure 4.30 presents the average weighted NS contours during rest-state and exercise.

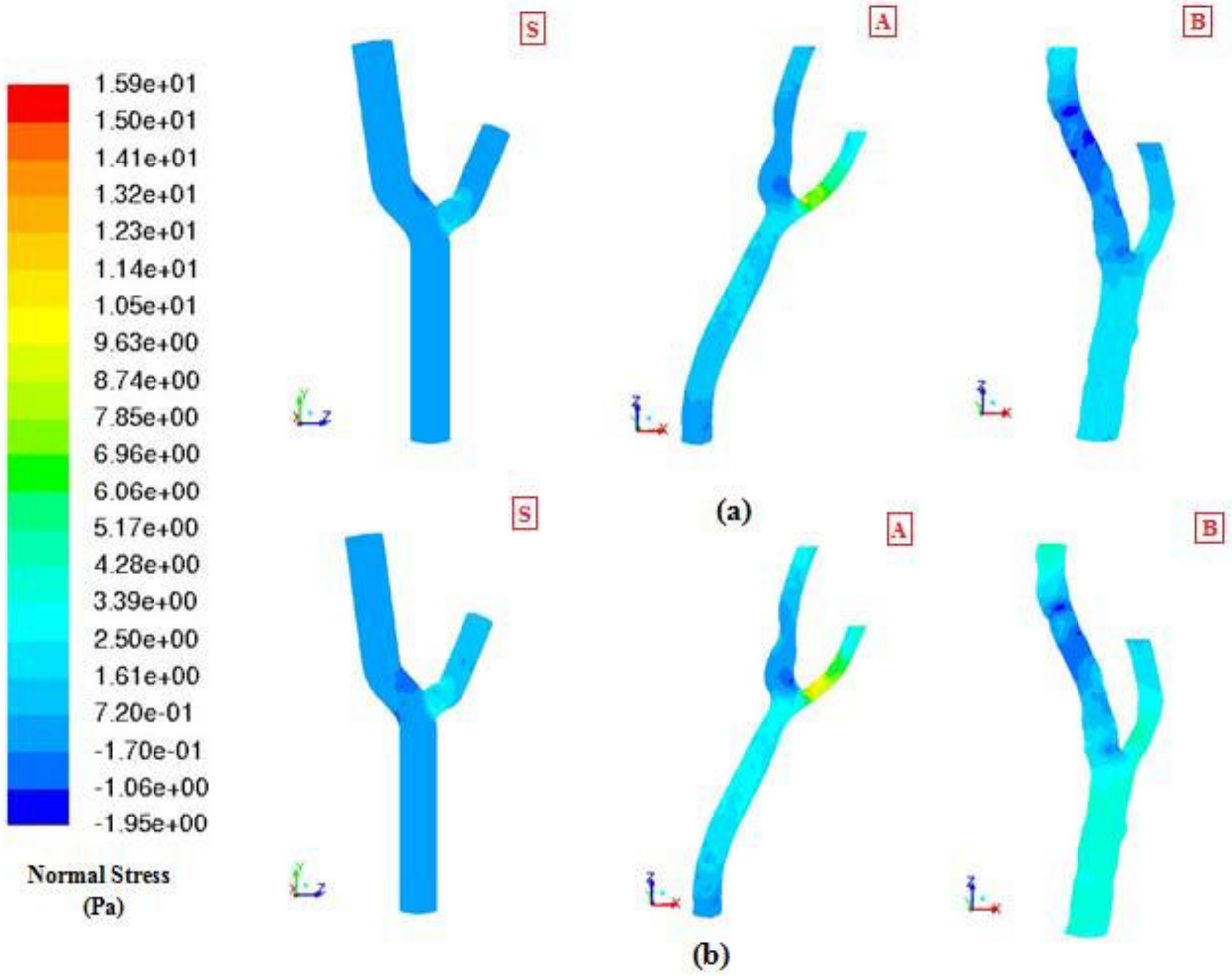

Figure 4.30. NS contours at systole during: (a) rest-state and exercise.

The NS contour snapshots are also taken at systole. As shown in Figure 4.30, the simplified carotid bifurcation arterial geometry, experiences an equalized balance of NS on all branches of the artery during rest-state. The average weighted NS is 0.72 Pa on the CCA, ECA, and ICA. However on the bifurcation region near the ECA, a small region experiences a slightly high NS of 1.61 Pa. However, during exercise, the average weighted NS increases from the bifurcation region throughout the ECA on the simplified geometry during exercise. The same trend occurs on Geometry B; however the magnitude on the ICA and CCA is 2.5 Pa with a small region on the sinus of –1.95 Pa. The negative sign indicates a compressive force, whereas the positive NS values indicate tensile. The magnitude of NS on the ECA has a concentrated region of NS of around 8.74 Pa and diminished to 4.28 Pa throughout the ECA. The same can be found true on Geometry B, the magnitude. The average NS on all branches of Geometry B is 2.5 with a small region on the ICA branch experiencing a compressive force of -1.95 Pa. The NS forces are important in analyzing the forces that may produce rupture in atheroprone areas or in a more generalized sense, areas that are experiencing endothelial cell death and thinning of the vessel lining.

As shown in Figure 4.31, vorticity in the arteries has the same trend as WSS. For the simplified case minimum vorticity (7.49 s^{-1}) takes place on the ICA, whereas on the CCA and ICA branch a magnitude of 1030 s^{-1} is experienced. For Geometry B, the least amount of vorticity is seen on the sinus bulb region whereas the highest magnitude takes place on the ECA branch. The least amount of vorticity occurring on the sinus bulb region is due to the lack of mass transport on the wall of the sinus. The maximum vorticity is due to continuity, the restriction of flow taking place on the ICA branch causes an acceleration of blood flow on the ECA branch and increase of vorticity. However for Geometry B, there is equalized vorticity on

the CCA branch throughout the ECA; however the highest magnitude of voracity is experience on the ICA branch. WSS, NS, and vorticity are vital measurements for assessing hemodynamic factors. In the present study, these three measures have been used to verify the role of age,

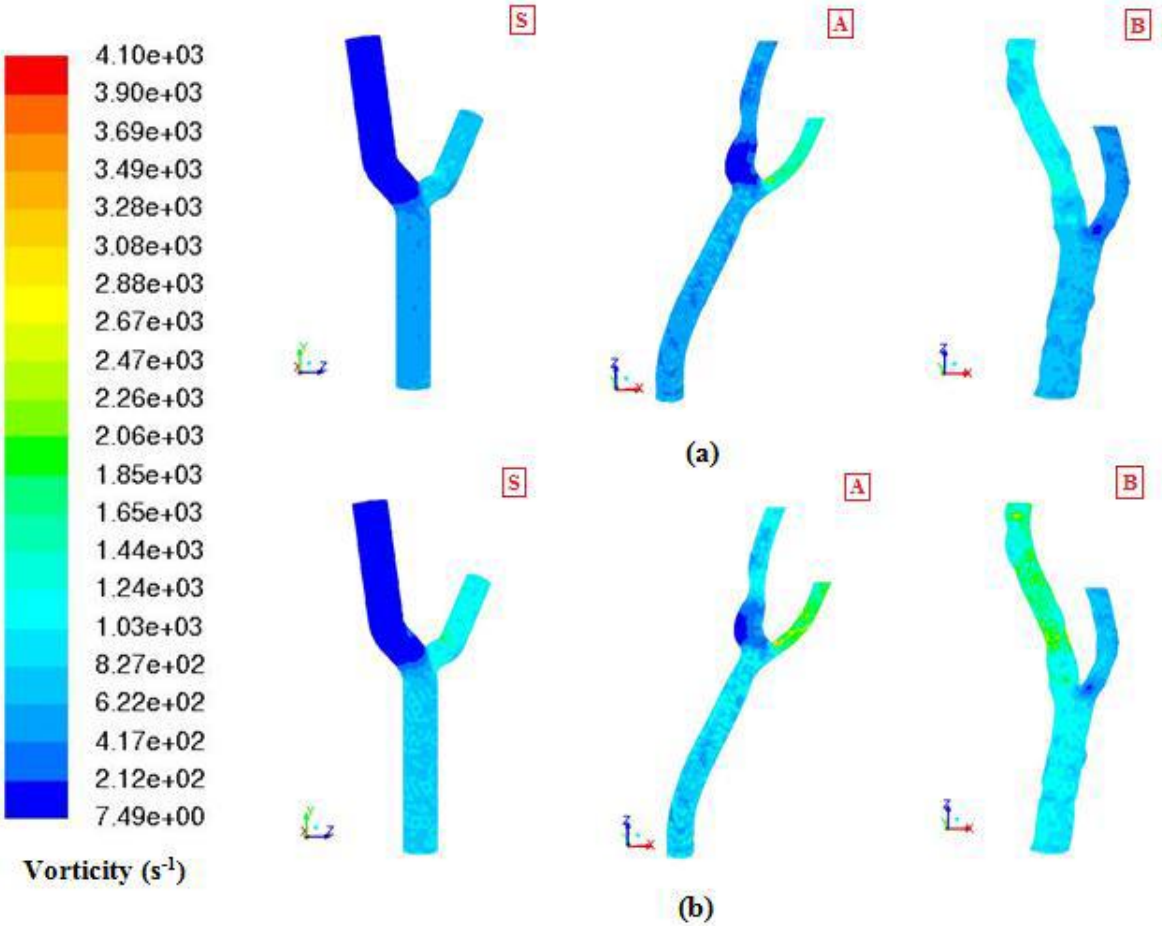

Figure 4.31. Vorticity contours at systole during: (a) rest-state and exercise.

gender, and geometry on hemodynamic flow patterns. The simplified geometry in the present study has proven to provide an exaggeration of hemodynamic parameters during analyses. The simplification of arterial vessel geometry yields hemodynamic results that cannot be substituted and relied on for real life measurements for male and female patients. For instance, for all cases of WSS, NS, and vorticity, the simplified geometry provided 0 WSS measurements on the ICA

branch which indicates no mass transport and for NS, equalized magnitudes of NS measurements on all branches with the exception of the bifurcation region. Geometry A and B yields meaningful results in the sense that the hemodynamic results are different in the case of age, gender, and arterial vessel geometry. The hemodynamic trends are different in the case of evaluating patient-specific geometry, thus confirming the effect of age, gender, and geometry on hemodynamics. Also the case of evaluating hemodynamics during rest-state and exercise has provided meaningful results in the sense that the magnitude of WSS during exercise provides a measure of the risk of WSS licensing of red blood cells, and NS provides a magnitude range for the risk of vessel rupture.

4.6 Evaluation of the Effect of Stent Design on Hemodynamic Flow

In the present study, the hemodynamic features of a simplified vs. patient-specific stented arteries are compared. In addition to simplified and patient-specific stented arteries, three different stent designs are assessed. Differences in WSS, normal (radial) stresses, and vorticity (de-mixing) are reported which confirms the effect of stent design, specifically strut positioning bridge pattern design on hemodynamics. Eqn. 4.13 is used to calculate the normal stresses. Physiological WSS in an artery is normally within a range from 1 Pa to 7 Pa (Malek 1999). However, WSS that exceed this range and occur at localizes sites can influence dislodging and/or migration of the stent. Figure 4.32 present the WSS contour plots of the simplified stented cores for stent designs A, B, and C. The highest WSS values were found to occur over the center of the curved region within the surface of the stent struts as shown in Figure 4.32.

$$\tau_{xx} = 2\mu \frac{\partial u}{\partial x} \qquad \text{Eqn. 4.13}$$

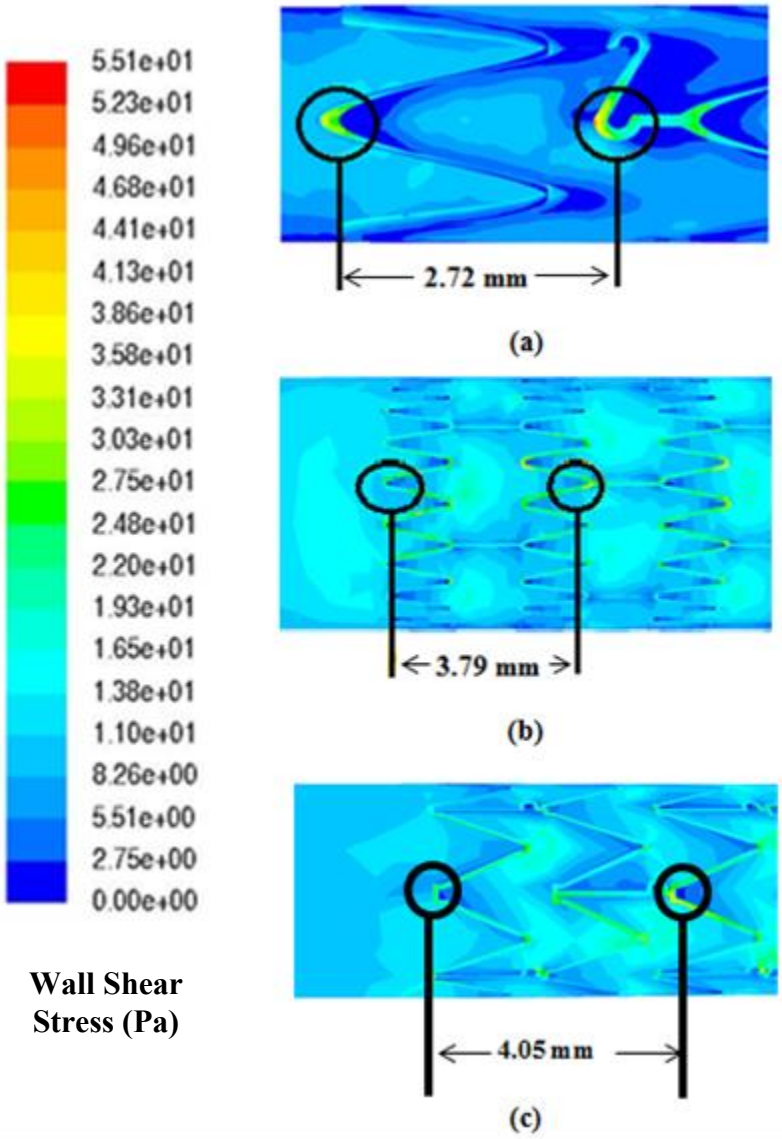

Figure 4.32. Wall shear stress contour for stent designs A,B, and C.

Also Figure 4.32 shows the regions of low WSS before and after each strut. For the simplified stented core and patient-specific stented core CFD analyses, WSS follows a trend for all stents except for regions between the strut and bridge, as shown in Figure 4.32. For stent designs A and C, a larger area of arterial tissue is exposed to relatively low WSS (light blue area in Figure 4.32 between stent struts), compared to Stent Design B. For Stent Design B, the arterial tissue

wall area within the first unit cell experiences a relatively high WSS compared to the area around the stent struts. For Stent Designs A and C, areas of low WSS occur at transitions between the core and stent and were most pronounced where the strut orientation was orthogonal to the direction of blood flow. For all three stents, WSS had a high value proximal to the stent struts and a relatively lower value in the area occupied or exposed to neighboring arterial wall tissue.

Figure 4.33a shows the point averaged normalized WSS patterns for all stents averaged over the entire stent wall core impression for the simplified stented cores and the patient-specific arterial stented cores. Figures 4.33a and 4.33b show the scaled WSS and radial stress results of the incoming fluid. The stresses are scaled with the dynamic pressure "ρV^2 "and the cycle time is scaled with the total time, t=3 sec. As shown in Figure 4.33a, the maximum normalized WSS for all stents occur at the point of maximum inlet velocity (systole) and the minimum normalized WSS occurs at the minimum inlet velocity (diastole). When comparing the normalized WSS results for the simplified arterial stented core results compared to the patient-specific stented core results, the percent difference of the point averaged normalized WSS for Stent Design A is 44.7%, 44.4% for Stent Design B, 55.8% for Stent Design C, and 25.65% for the Simplified Stent Design.

Maximum WSS within the stented region for all stent designs are localized within the curved regions of the struts. Figure 4.33b shows the normalized point averaged radial stress trend for all stents averaged over the entire stent wall impression for the simplified stented cores and the patient-specific arterial stented cores. When comparing the normalized radial stress results for the patient-specific arterial stented cores compared to the simplified arterial stented cores, the percent difference in results for all stent designs exceed 98.3%. Figure 4.34 present

plots of the distributions of normalized WSS as a function of normalized strut distance within the unit cell of each stent design.

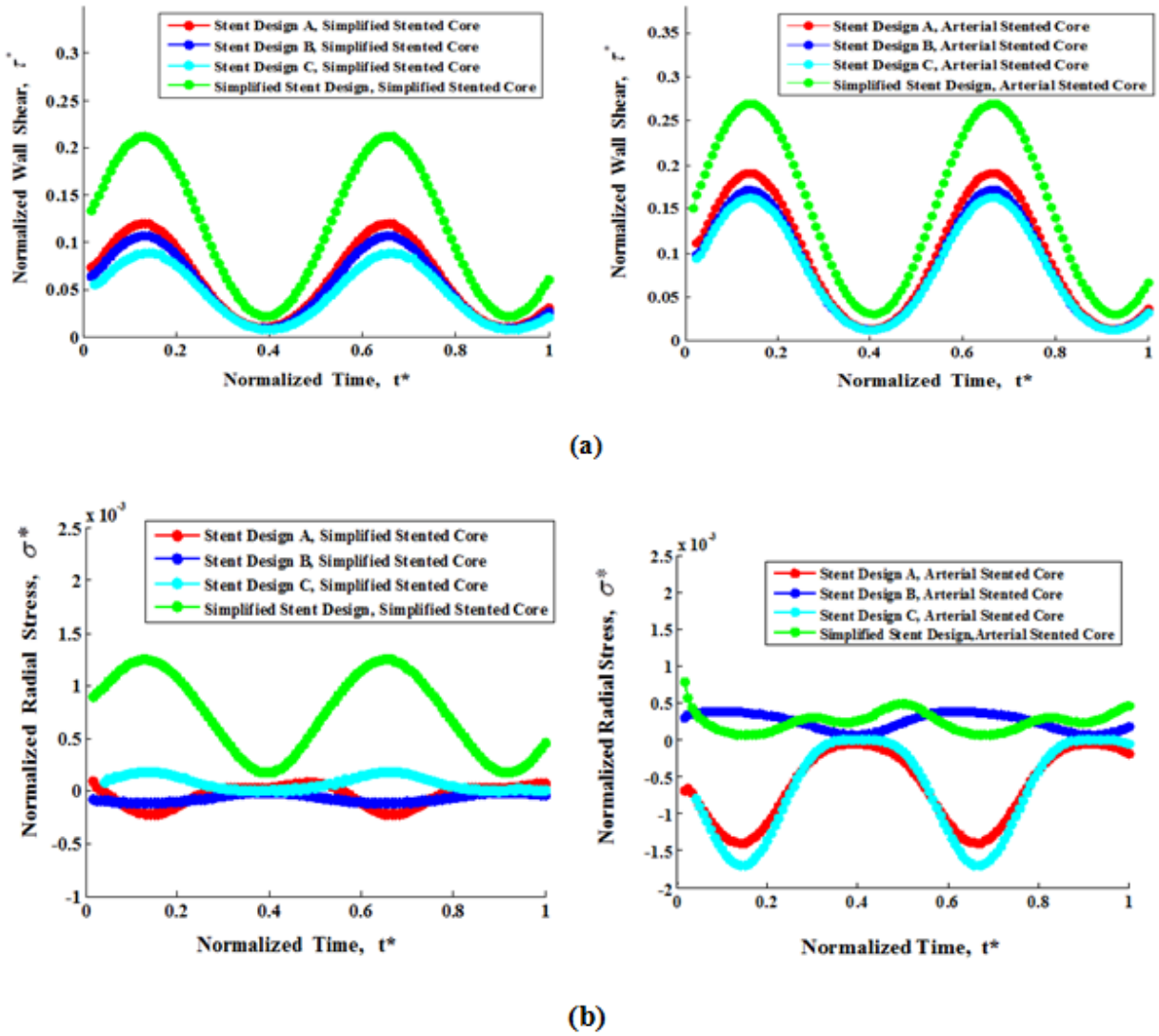

Figure 4.33. Plot of: (a) normalized wall shear stress vs. normalized time and (b) normalized radial stress vs. normalized time.

The distance is scaled with the total distance from strut to strut (x*=x/L). From Figure 4.34a and 4.34b, the trend of WSS within the area where the tissue is exposed to the blood has a threshold region of minimum WSS. The threshold of minimum WSS may be attributed to the

large area of tissue exposure which minimizes flow disturbance and also minimizes flow resistance. In Figure 4.34c, the maximum WSS occurs in the unit cell area where the tissue is exposed to blood flow which is due to the minimum area that exists between struts for stent design C. Also stent design C has more struts compared to stent designs A and B, which influence flow disturbance and WSS. A general conclusion that can be drawn from these analyses is that large arterial tissue exposure within the stent unit cell experiences a lower WSS compared to stents with small arterial tissue exposure.

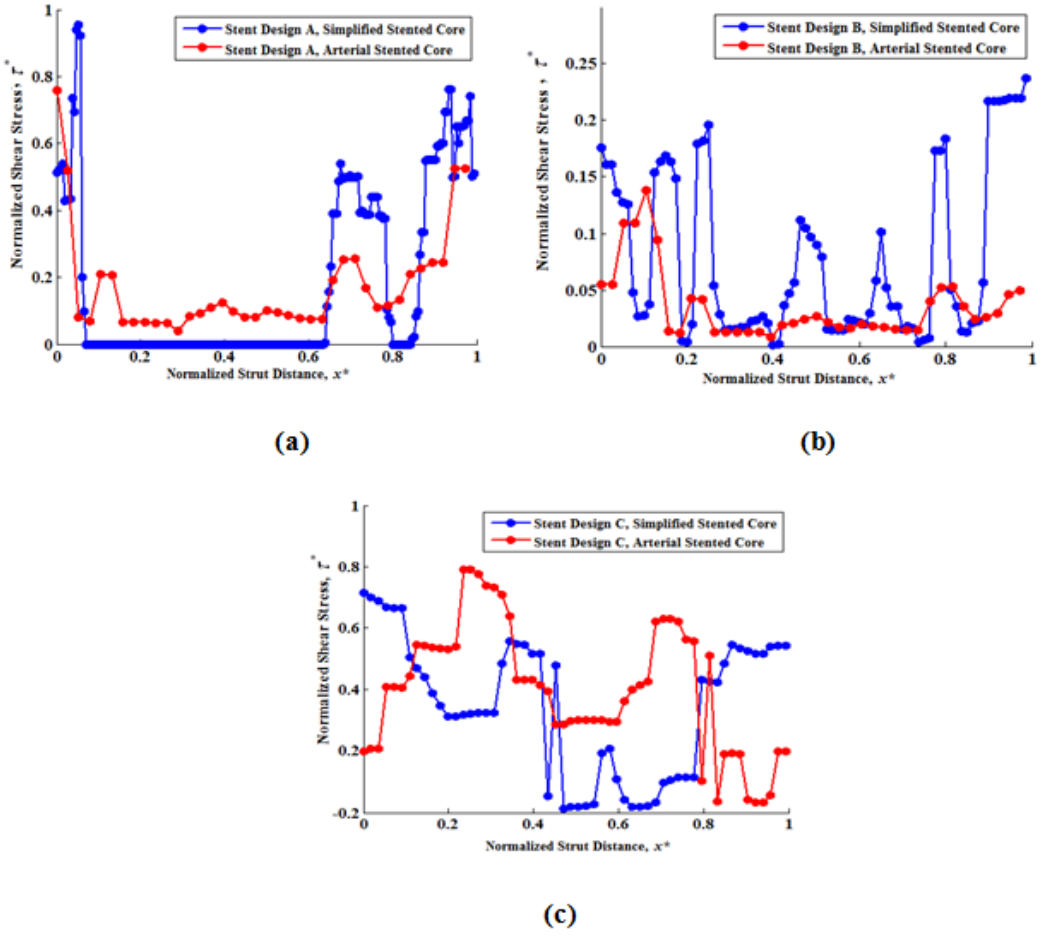

Figure 4.34. Plot of normalized wall shear stress vs. normalized strut distance for (a) stent design A and simplified stented core, (b) stent design B and simplified stented core, and stent design C and simplified stented core.

The flow distributions and WSS in larger arterial tissue exposure minimize due to the absence of stent struts. Figure 4.35 present plots of distributions of normalized radial stress as a function of normalized strut distance within the unit cell of each stent design. The trend of increasing stress with smaller arterial tissue exposure is observed in the results presented in Figure 4.35.

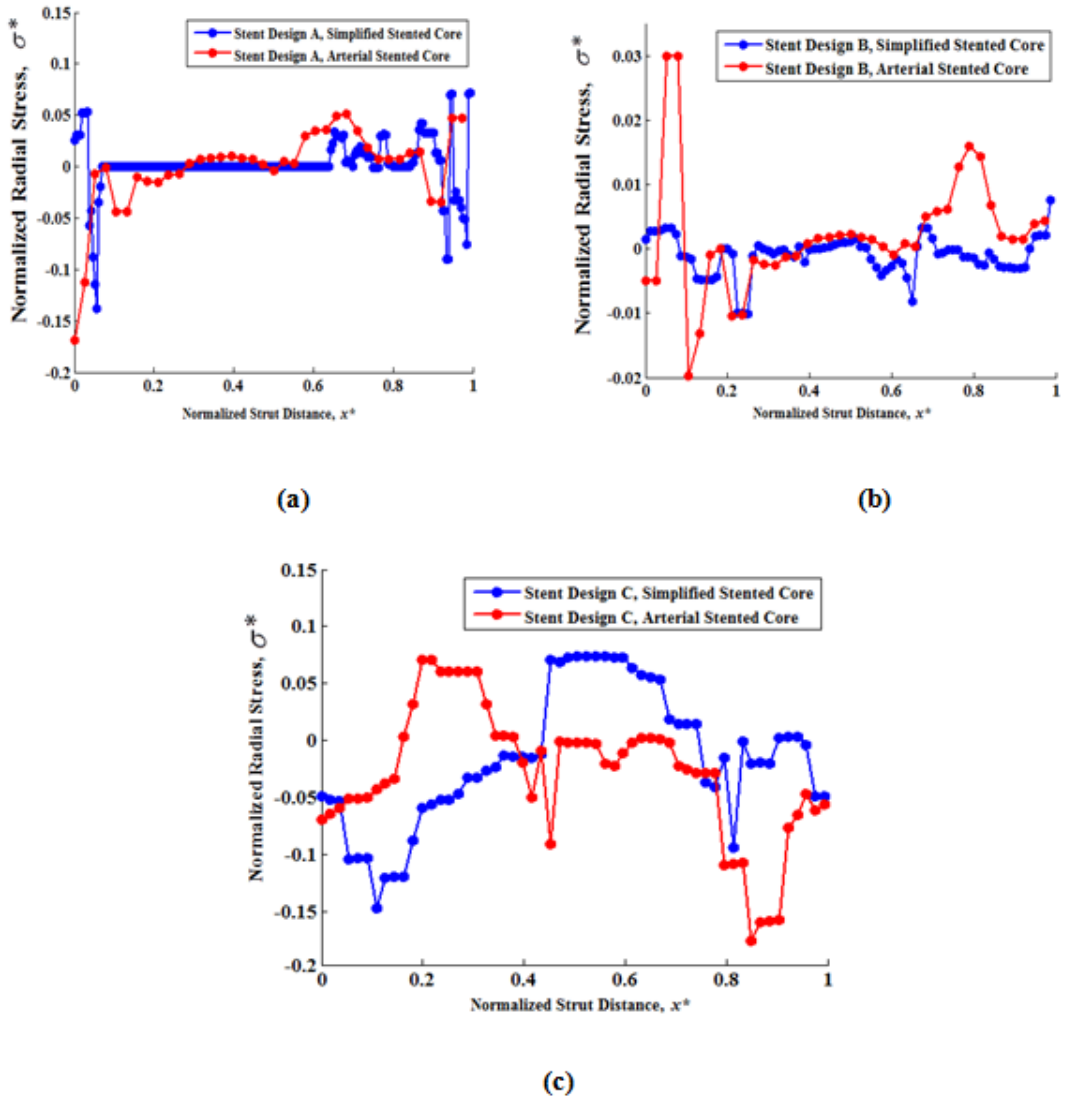

Figure 4.35. Plot of normalized radial stress vs. normalized strut distance for: (a) stent design A, (b) stent design B, and (c) stent design C.

When comparing the magnitudes of WSS and radial stress, the radial stresses that occur in both the simplified stent arterial cores and patient-specific arterial stented cores are much smaller compared to WSS and can be neglected. As shown previously in Figures 4.34 and 4.35, the presence of a stent inside the arterial vessel gives rise to flow resistance and flow recirculation (vorticity). Vorticity is defined as the spin or rotation of a fluid. Vorticity is an important parameter in accessing hemodynamic factors because the magnitude of vorticity influences the separation of blood constituents. Vorticity can be defined as the magnitude of de-mixing as it pertains to hemodynamics. Blood is a heterogeneous mixture of various substances and the magnitude of vorticity in stented arteries influences flow alteration and may cause acute pathobiological responses. As mentioned previously, vorticity has been a major predictor of wall shear disturbance and vessel rupture.

Figure 4.36 shows plots of the point averaged axial vorticity patterns for all stents averaged over the entire stent wall core impression for the simplified stented cores and the patient-specific arterial stented cores for the entire cardiac cycle. Figure 4.36a shows that the highest magnitude of flow reversal (de-mixing) exists in Stent Design C, followed by Stent Design A, the Simplified Stent Design, and Stent Design B. Figure 4.36b shows that the highest magnitude of flow reversal exists in Stent Design A, followed by the Simplified Stent Design, Stent Design C, and lastly Stent Design B. Figures 4.36a and 4.36b, show that the hemodynamic behavior of the flow of a stented vessel is not only a function of the stent geometry, but the upstream geometry before the entrance of the stent is important in modeling blood flow in a stented vessel.

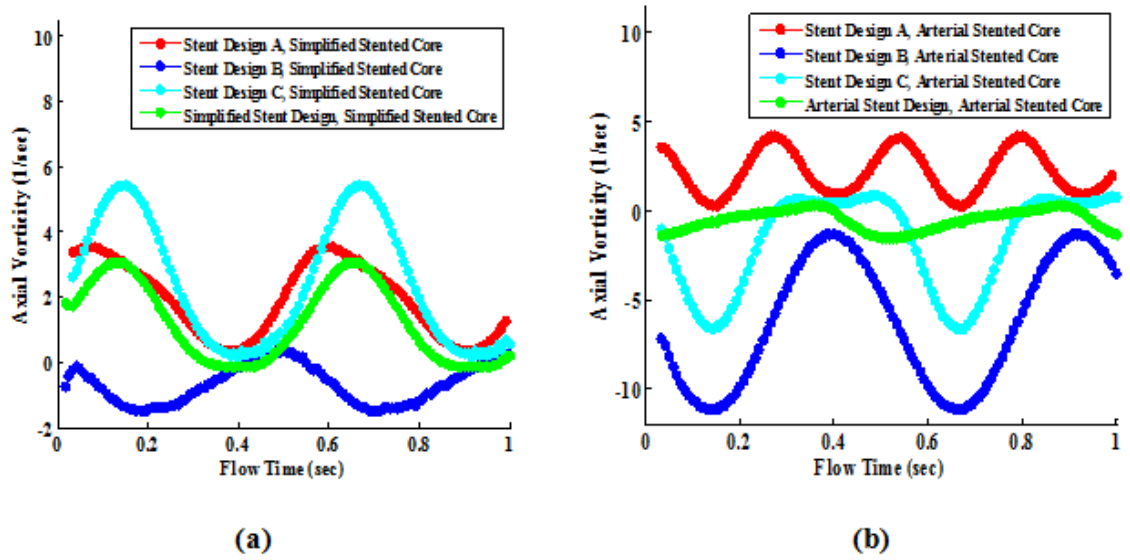

Figure 4.36. Plot of axial vorticity vs. flow time.

Figure 4.37 shows the magnitude of recirculation that occurs between the struts of all stented cores. The magnitude of recirculation varies with distance from strut to strut. For example, in Figure 4.37a, Stent Design A has a vorticity magnitude of 650 s^{-1} which then changes direction and magnitude to 620 s^{-1} and then minimizes to 198 s^{-1} before stabilizing to a vorticity magnitude around 90 s^{-1}. Recirculation zones in the cross-flow direction are observed for all stent designs close to the arterial wall. Recirculating flow may be caused by the bridge connectors that protrude into the space between the struts. It is important to note that the magnitude of vorticity is different for each stent design. Also as shown in Figure 4.37, the magnitude of vorticity varies with the geometry of the arterial core upstream of the stented region entrance. WSS and radial stresses is a function of stent design, and vorticity is also a function of both stent design and the stented core geometry.

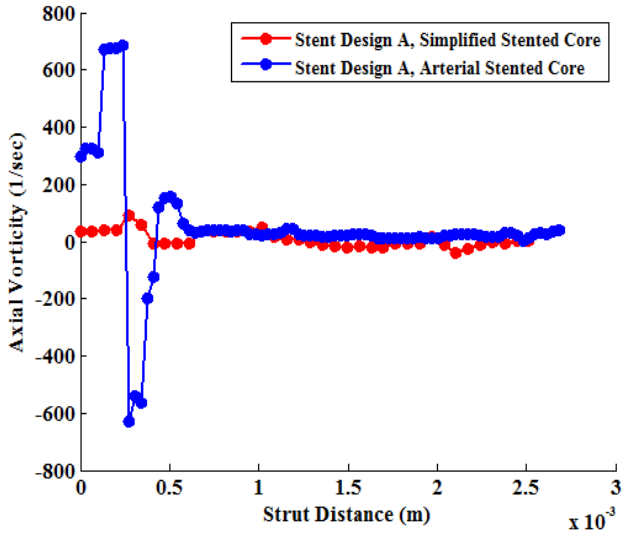

(a)

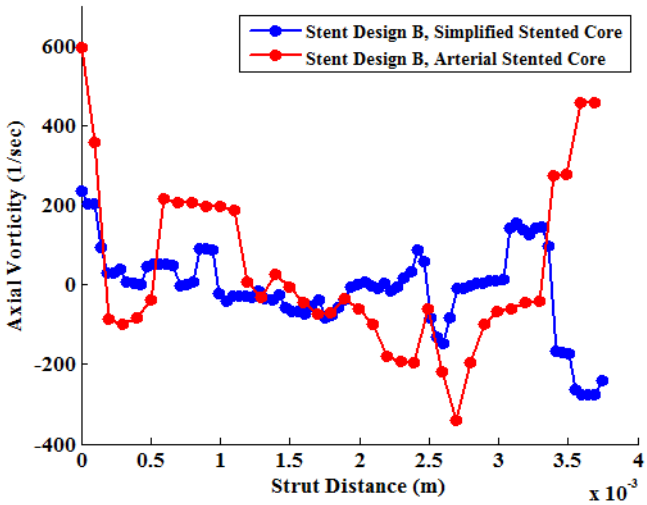

(b)

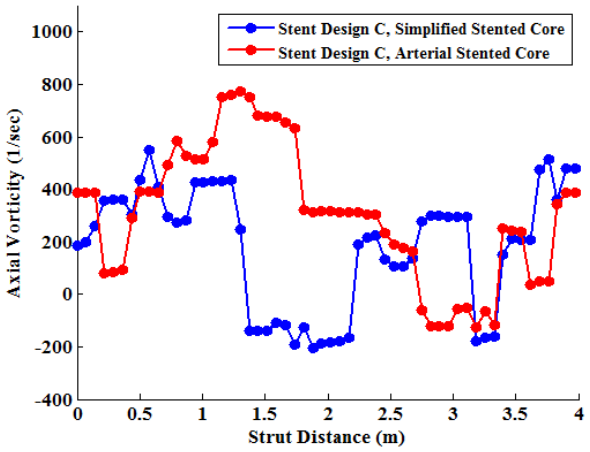

(c)

Figure 4.37. Axial vorticity vs. strut distance.

4.7 Digital Cardiovascular Phantom Hemodynamic Results

In the present study a simple analysis was conducted to analyze the levels of wall shear stress and normal stress that are present in the arteries of the full digital cardiovascular system. Thus far, all of the hemodynamic parameters analyzed such as normal stress, wall shear stress, and vorticity in the arteries via CFD have been analyzed in systems whereby the artery analyzed is a single unit (an artery that is not connected with its neighboring constituent arteries). The present study addresses the magnitude of stresses found in the arterial system during a normal cardiac cycle. The digital cardiovascular system is the same model that was used earlier in the dye concentration analyses. The analysis discussed here consists of a rest state cycle analysis and static posture study.

Figure 4.38 present the wall shear stress contours for the digital cardiovascular phantom. The contours present the wall shear magnitudes at different times during the cardiac cycle. Figure 4.38a present the wall shear stress contour at diastole and Figure 4.38b present the wall shear stress contour at systole. The contours are broken into sections due to regions of varying wall shear stress in the digital cardiovascular system. The magnitude of the wall shear stress is higher in the mid-section of the phantom (aortic section) as appose to the upper level (cerebral). The same is true for normal stress. As mentioned earlier in the preceding sections, the range of wall shear stress in the arterial system ranges from 1-12 Pa during normal cardiac cycle.

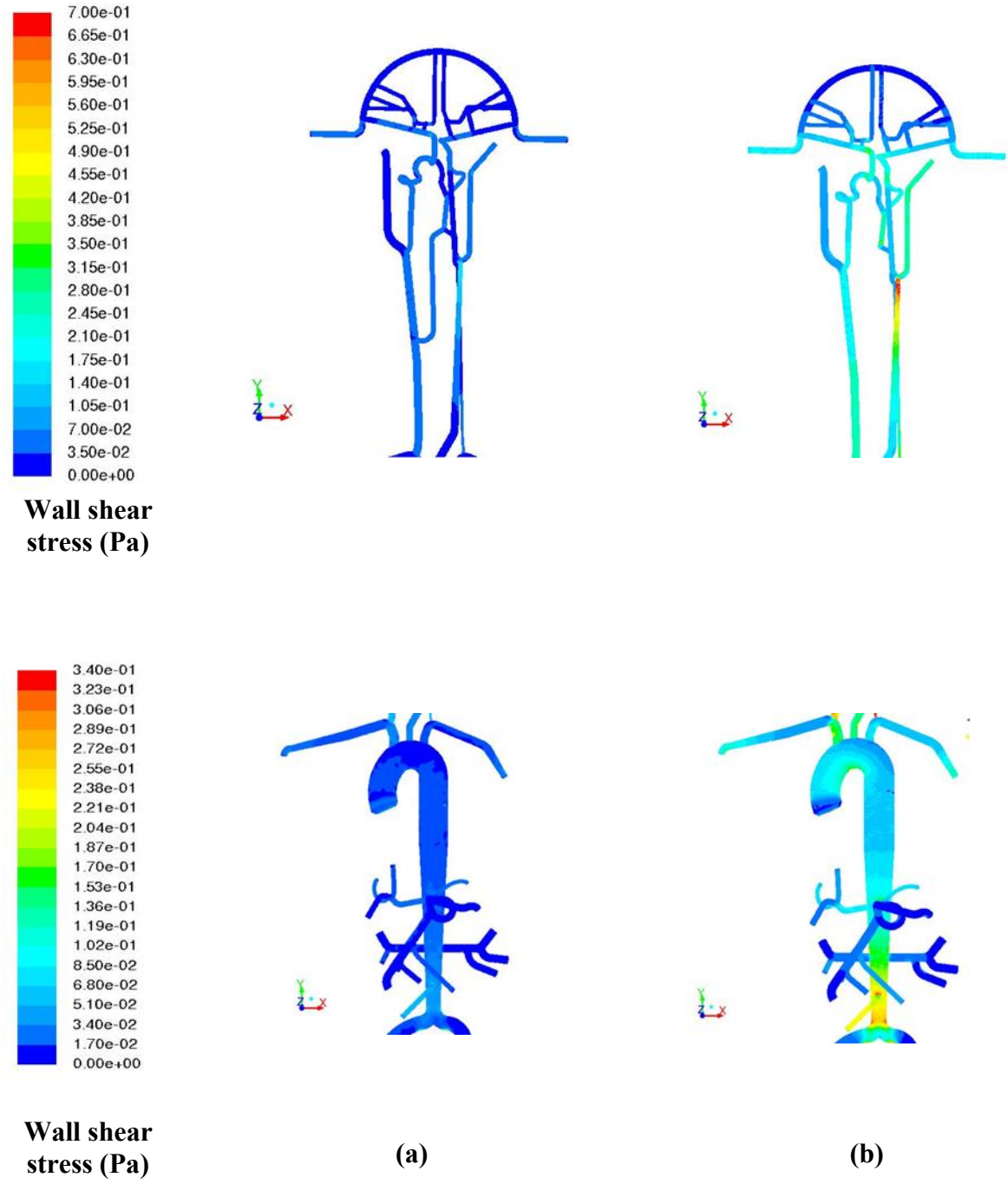

Figure 4.38. Wall shear stress contours during (a) diastole and (b) systole.

From Figure 4.33 the wall shear stress magnitude scale ranges from 0 to 0.7 Pa. The cardiovascular phantom represents a healthy male. From Figure 4.38, the highest wall shear stress during diastole at rest state cycle is observed in femoral section around 0.170 Pa. The

highest wall shear stress during systole is in the CCA and the femoral section at 0.7 Pa. Also observed in the Figure 4.38b is that the highest wall shear stress is observed in sections where there are bends, curves, and branching.

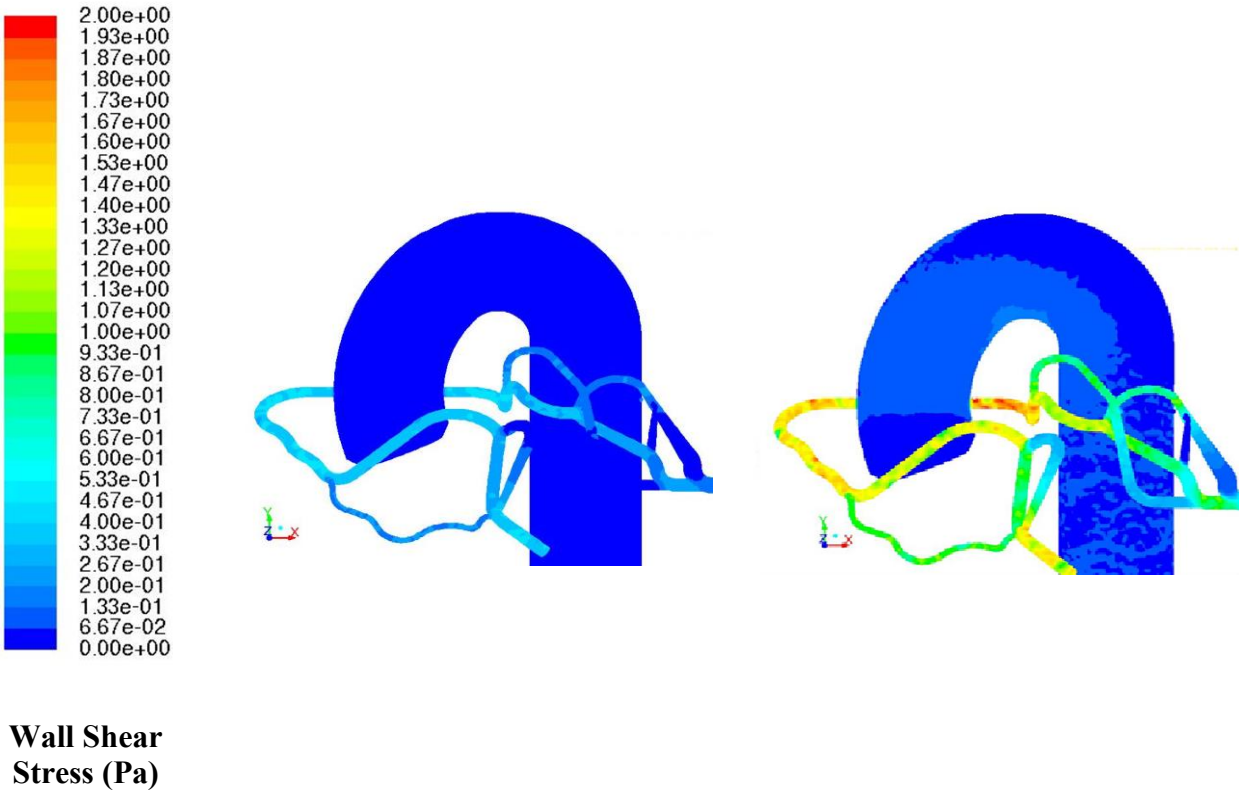

Figure 4.39. Wall shear stress contour for the coronary arteries.

Figure 4.39 presents the wall shear stress contours for the coronary arteries which are attached to the aortic valve section. The scale of the wall shear stress for the coronary arteries ranges from 0 to 2 Pa. Similar to the wall shear stress in the neighboring arteries, the highest wall shear stress occurs around curves and bends. The highest wall shear observed in the coronary arteries is 2 Pa which is at systole. The reason for the highest wall shear being present in the coronary is because the coronary arteries have a much smaller diameter than the aorta. The Venturi effect causes a higher wall shear stress magnitude. Due to continuity, the Venturi effect describes the

nature of acceleration in flow due to a reduction in area. Continuity states that mass must be conserved regardless of the increase or decrease in area. The highest wall shear indicated regions where there is accelerated transport of blood. Previous studies have indicated that wall shear stress promotes cell growth. It is hypothesized in the present study that the transport of blood and nutrients promotes cell growth and that wall shear stress is a mere indication of transport. The most significant take away is that in a normal situation for rest state cycle is that the range of wall shear stress is from 0 to 2 Pa and that the highest magnitude of wall shear is present in sections where there are curves, bends, and branching into constituent arteries.

Figure 4.40 present the normal stress contours for the digital cardiovascular phantom. The contours present the normal stress magnitudes at different times during the cardiac cycle. Figure 4.40a present the normal stress contour at diastole and Figure 4.35b present the normal stress contour at systole. Similar to Figure 4.40, the contours are broken into sections due to regions of varying normal stress in the digital cardiovascular system. The magnitude of the normal stress is higher in the mid-section of the phantom (aortic section) as appose to the upper level (cerebral). From Figure 4.40 the normal stress magnitude scale ranges from -0.1 to 0.275 Pa. From Figure 4.40, the highest normal stress during diastole at rest state cycle is observed in femoral section around 0.0253 Pa. The highest normal stress during systole is in the CCA and the femoral section at 0.275 Pa. The normal stress is useful because it provides insight on the level of forces normal to the direction of flow is present. High normal forces can promote restenosis, penetration/rupture, and dislodging/movement of medical implants. Figure 4.41 presents the normal stress contours for the coronary arteries. The scale of the normal stress for the coronary arteries ranges from -0.5 to 1.40 Pa.

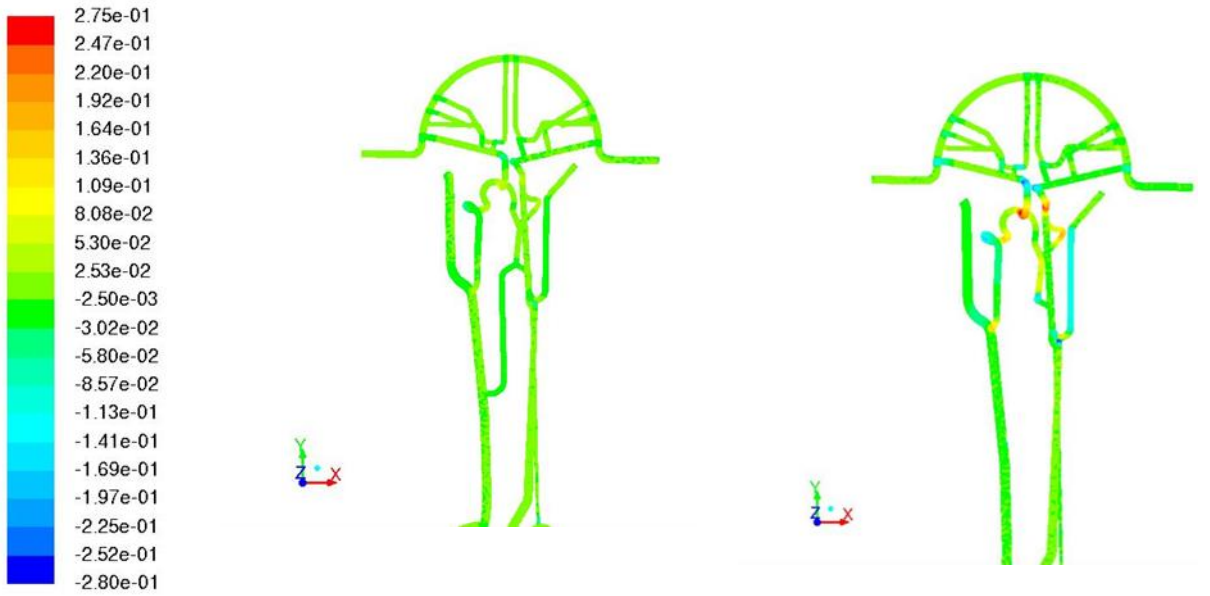

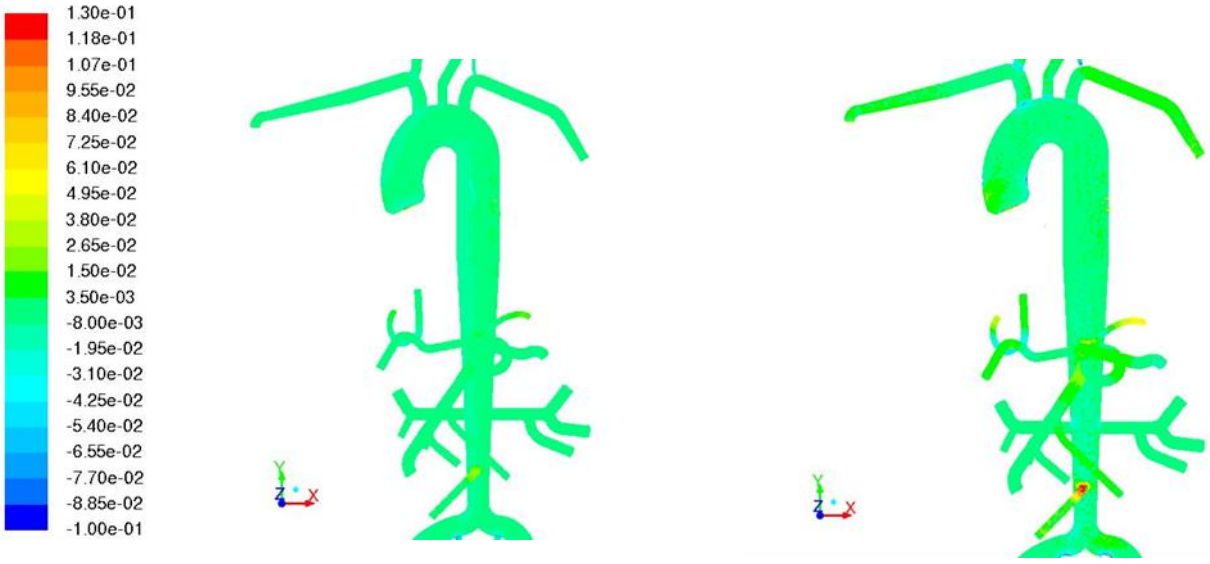

Figure 4.40. Normal stress contours during (a) diastole and (b) systole.

Similar to the normal stress in the neighboring arteries, the highest wall shear stress occurs around curves and bends. The highest normal stress observed in the coronary arteries is 1.40 Pa which is at systole.

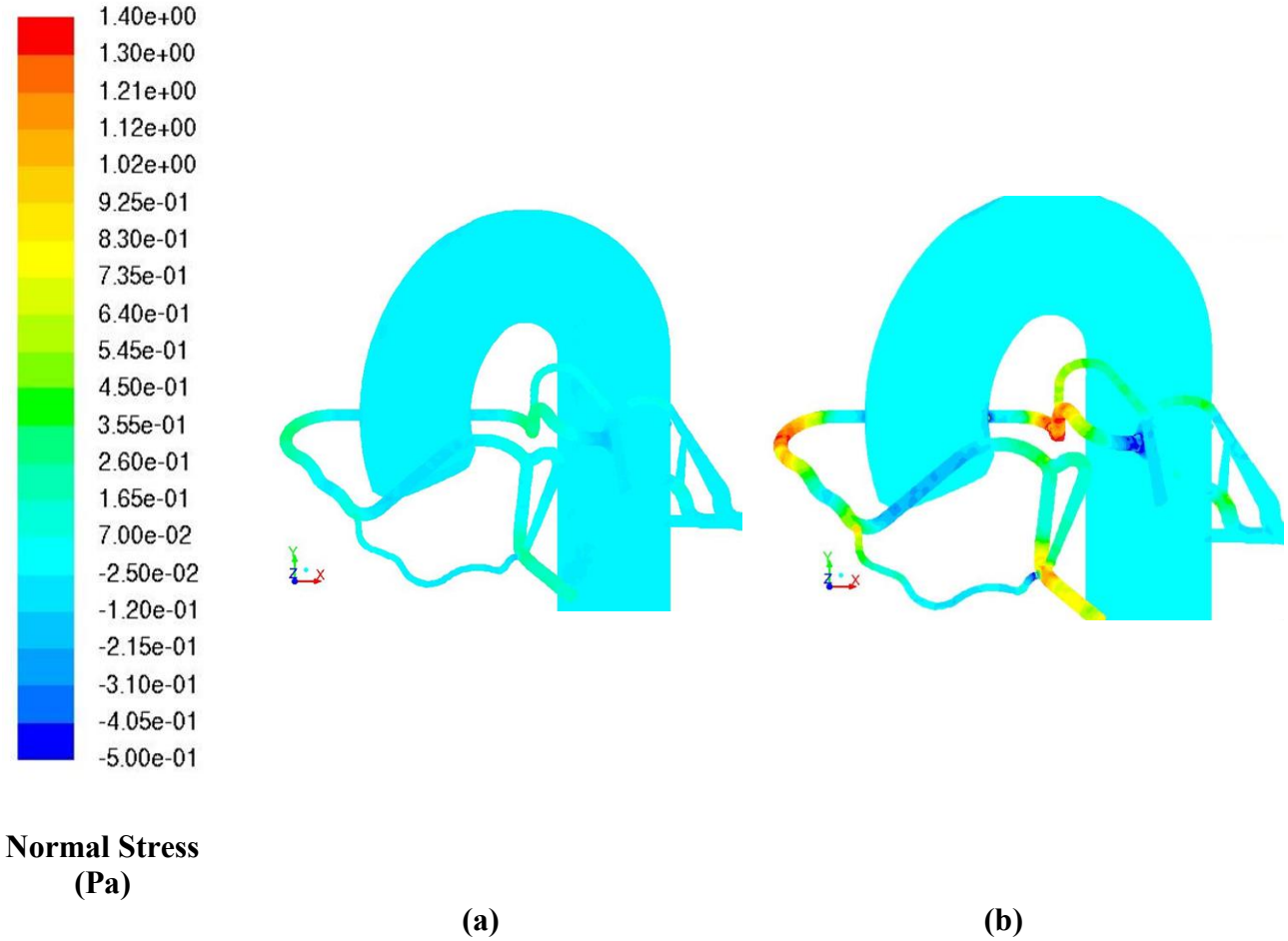

Figure 4.41. Normal stress contours for the coronary arteries during (a) diastole and (b) systole.

Similar to the wall shear contours, the highest stress is observed in regions where there are curves and bends. Future studies are needed to confirm the magnitude of stress for healthy and diseased arteries in full cardiovascular models to determine the effects of local hemodynamics on global hemodynamics.

CHAPTER 5

Discussion and Future Research

The ultimate goal of the present study was to aid in the development of tools to assist in the treatment of cardiovascular disease and atherosclerosis. In the present study a full cardiovascular experimental phantom and digital phantom (CFD model) was fabricated to study: (1) the effects of local hemodynamics on global hemodynamics, (2) the effects of transition from bed-rest to upright position, and (3) transport of dye (drug delivery) in the arterial system. Computational three dimensional (3-D) models of drug eluting stents implanted into the arterial wall were studied in addition to patient-specific arterial hemodynamic models and stents design flow studies. In the case of the drug eluting stent studies, the main conclusion is that using the diffusivity for the drug analyzed in the present study, the time that it takes for the drug to diffuse through the entire wall for the implanted stent is approximately 3.5 months. Future studies will involve implementing internalized reversible binding of the drug to study the effect of unbound on bound drug diffusion through the artery wall. Future studies will also involve implementing porosity parametric studies on stent design to evaluate the effect of stent design on drug diffusion. For postural change studies, future studies will involve implementing coding to simulate baro-regulation to incorporate the full effect of orthostatic pressure changes and systematic responses.

For arterial CFD studies, patient-specific CA models were generated from computed tomography angiography (CTA) scans and modeled for CFD. The simulated flow profiles in the patient-specific geometries were compared against a simplified carotid bifurcation geometry to evaluate the efficacy of modeling patient-specific geometries against an alternate simplified geometry. Models were also evaluated by comparing hemodynamic parametric magnitudes via

patient-specific and simplified velocity waveforms. The main conclusion in this work is that dynamic behaviors of blood through the patient-specific carotid bifurcation arterial geometries based on numerical approaches showed differences when compared to a simplified carotid artery bifurcation geometry. For the patient-specific geometries, the velocity gradients near the stenosis were much higher than those near the sinus. Flow reversal and low WSS was observed in the sinus region of the patient-specific models. Also, for the simplified geometry, there was a small region of velocity increase at the stenosis, and very little flow downstream of the stenosis to the ICA outlet. The major increase of velocity in the simplified geometry was experienced in the ECA branch of the artery, while in the patient-specific geometries, the reverse is true. The present study has proven that using simplified arterial geometries results in an exaggeration of hemodynamic parameters thus confirming the effect of age, gender, and arterial vessel geometry on hemodynamics.

Future studies will incorporate the moving boundary of the arterial wall, instead of using rigid wall boundary conditions. A future study consisting of a broad statistical study on the effect of patient-specific arterial geometry on hemodynamic flow will be conducted. For dye concentration studies using the cardiovascular phantom, a more accurate study will be conducted using photo-diodes to measure the dye concentration as function of time non-invasively. In the case of evaluating the effect of stent design on hemodynamic flow, future studies will also involve studying the effect of drug deposition into the blood stream.

References

Aboamer, M. A., A. T. Azar, et al. (2014). "Linear Model-Based Estimation of Blood Pressure and Cardiac Output for Normal and Paranoid Cases." *Neural Computing & Applications* 25(6): 1223-1240.

Aquino, K. M., P. A. Robinson, et al. (2014). "Spatiotemporal Hemodynamic Response Functions Derived from Physiology." *Journal of Theoretical Biology* 347: 118-136.

Arai, M., N. R. Alpert, et al. (1993). "Alterations in Sarcoplasmic-Reticulum Gene-expression In Human Heart-Failure - A Possible Mechanism for Alterations in Systolic And Diastolic Properties of the Failing Myocardium." *Circulation Research* 72(2): 463-469.

Aroney, C. N., H. C. Herrmann, et al. (1989). "Linearity of the Left-Ventricular End-Systolic Pressure-Volume Relation in Patients with Severe Heart-Failure." *Journal of the American College of Cardiology* 14(1): 127-134.

Arts, T., P. H. M. Bovendeerd, et al. (1991). "Relation Between Left-Ventricular Cavity Pressure and Volume and Systolic Fiber Stress and Strain in the Wall." *Biophysical Journal* 59(1): 93-102.

Atar, D., W. D. Gao, et al. (1995). "Alterations of Excitation-Contraction Coupling in Stunned Myocardium and in Failing Myocardium." *Journal of Molecular and Cellular Cardiology* 27(2): 783-791.

Bale-Glickman, J., K. Selby, et al. (2003). "Experimental Flow Studies in Exact-Replica Phantoms of Atherosclerotic Carotid Bifurcations Under Steady Input Conditions." *Journal of Biomechanical Engineering-Transactions of the ASME* 125(1): 38-48.

Bao, X. P., C. Y. Lu, et al. (1999). "Temporal Gradient in Shear but Not Steady Shear Stress Induces PDGF-A and MCP-1 Expression In Endothelial cells - Role of NO, NF kappa B, and egr-1." *Arteriosclerosis Thrombosis and Vascular Biology* 19(4): 996-1003.

Baran, D., K. Ogino, et al. (1997). "Interrelating of Ventricular Pressure and Intracellular Calcium In Intact Hearts." *American Journal of Physiology-Heart and Circulatory Physiology* 273(3): H1509-H1522.

Bascom, P. A. J., K. W. Johnston, et al. (1997). "Relation of the Flow Field Distal to a Moderate Stenosis to The Doppler Power." *Ultrasound in Medicine and Biology* 23(1): 25-39.

Batchelor, G. K., et al., (2002). "Blood Flow in Arteries and Veins, in Perspectives in Fluid Dynamics: A Collective Introduction to Current Research." *Cambridge University Press. chap.* 3 105-158.

Beltrami, C. A., N. Finato, et al. (1994). "Structural Basis Of End-Stage Failure In Ischemic Cardiomyopathy In Humans." *Circulation* 89(1): 151-163.

Benard, N., D. Coisne, et al. (2003). "Experimental Study of Laminar Blood Flow Through an Artery Treated by a Stent Implantation: Characterization of Intra-stent Wall Shear Stress." *Journal of Biomechanics* 36(7): 991-998.

Berry, J. L., A. Santamarina, et al. (2000). "Experimental and Computational Flow Evaluation of Coronary Stents." *Annals of Biomedical Engineering* 28(4): 386-398.

Beuckelmann, D. J., M. Nabauer, et al. (1992). "Intracellular Calcium Handling in Isolated Ventricular Myocytes from Patients with Terminal Heart-Failure." *Circulation* 85(3): 1046-1055.

Bharadvaj, B. K., R. F. Mabon, et al. (1982). "Steady Flow in a Model of The Human Carotid Bifurcation " *Journal of Biomechanics* 15(5): 349-362.

Bharadvaj, B. K., R. F. Mabon, et al. (1982). "Steady Flow in a Model of The Human Carotid Bifurcation Part 2. Laser Doppler Anemometer Measurements." *Journal of Biomechanics* 15(5): 363-378.

Bhattacharya-Ghosh, B., S. Bozkurt, et al. (2014). "An In-Silico Case Study of Idiopathic Dilated Cardiomyopathy Via a Multi-scale Model of the Cardiovascular System." *Computers in Biology and Medicine* 53: 141-153.

Bhattacharya-Ghosh, B., S. Schievano, et al. (2012). "A Multi-physics and Multi-scale Lumped Parameter Model of Cardiac Contraction of the Left Ventricle: A Conceptual Model from the Protein to the Organ Scale." *Computers in Biology and Medicine* 42(10): 982-992.

Blake, J. R., W. J. Easson, et al. (2009). "A Dual-Phantom System for Validation of Velocity Measurements In Stenosis Models Under Steady Flow." *Ultrasound in Medicine and Biology* 35(9): 1510-1524.

Blake, J. R., S. Meagher, et al. (2008). "A Method to Estimate Wall Shear Rate with a Clinical Ultrasound Scanner." *Ultrasound in Medicine and Biology* 34(5): 760-774.

Bohs, L. N., B. H. Friemel, et al. (1995). "Experimental Velocity Profiles and Volumetric Flow Via 2-Dimensional Speckle Tracking." *Ultrasound in Medicine and Biology* 21(7): 885-898.

Bonithon Kopp, C., P. J. Touboul, et al. (1996). "Factors of Carotid Arterial Enlargement in a population aged 59 to 71 years - The EVA study." *Stroke* 27(4): 654-660.

Brands, P. J., A. P. G. Hoeks, et al. (1995). "A Non-Invasive Method to Estimate Wall Shear Rate Using Ultrasound." *Ultrasound in Medicine and Biology* 21(2): 171-185.

Cao, J. and S. E. Rittgers (1998). "Particle Motion Within In Vitro Models of Stenosed Internal Carotid and Left Anterior Descending Coronary Arteries." *Annals of Biomedical Engineerin*g 26(2): 190-199.

Charonko, J., S. Karri, et al. (2010). "In Vitro Comparison of the Effect of Stent Configuration on Wall Shear Stress Using Time-Resolved Particle Image Velocimetry." *Annals of Biomedical Engineering* 38(3): 889-902.

Cheung, S. C. P., K. K. L. Wong, et al. (2010). "Experimental and Numerical Study on the Hemodynamics of Stenosed Carotid Bifurcation." *Australasian Physical & Engineering Sciences in Medicine* 33(4): 319-328.

Colombo, A., J. W. Moses, et al. (2004). "Randomized Study to Evaluate Sirolimus-Eluting Stents Implanted at Coronary Bifurcation Lesions." *Circulation* 109(10): 1244-1249.

Cox, L. G. E., S. Loerakker, et al. (2009). "A Mathematical Model to Evaluate Control Strategies for Mechanical Circulatory Support." *Artificial Organs* 33(8): 593-603.

DePaola, N., P. F. Davies, et al. (1999). "Spatial and Temporal Regulation of Gap Junction Connexin43 in Vascular Endothelial Cells Exposed to Controlled Disturbed Flows In Vitro." *Proceedings of the National Academy of Sciences of the United States of America* 96(6): 3154-3159.

Depaola, N., M. A. Gimbrone, et al. (1992). "Vascular Endothelium Responds To Fluid Shear-Stress Gradients." *Arteriosclerosis and Thrombosis* 12(11): 1254-1257.

Desouza, N. M., D. H. King, et al. (1991). "Quickscan - Doppler Ultrasound Emulation of Angiography - Its Value Prior To Arteriography In Peripheral Vascular-Disease." *British Journal of Radiology* 64(762): 479-484.

Diaz-Zuccarini, V. and J. LeFevre (2007). "An Energetically Coherent Lumped Parameter Model of the Left Ventricle Specially Developed for Educational Purposes." *Computers in Biology and Medicine* 37(6): 774-784.

Dobrin, P. B. (1978). "Mechanical-Properties of Arteries." *Physiological Reviews* 58(2): 397-460.

Drangova, M., D. W. Holdsworth, et al. (1993). "Elasticity And Geometry Measurements of Vascular Specimens Using A High-Resolution Laboratory CT Scanner." *Physiological Measurement* 14(3): 277-290.

Duraiswamy, N., R. T. Schoephoerster, et al. (2007). Stented Artery Flow Patterns and Their Effects On The Artery Wall. *Annual Review of Fluid Mechanics. Palo Alto, Annual Reviews*. 39: 357-382.

Farmakis, T. M., J. V. Soulis, et al. (2004). "Wall Shear Stress Gradient Topography in the Normal Left Coronary Arterial Tree: Possible Implications for Atherogenesis." *Current Medical Research and Opinion* 20(5): 587-596.

Folsom, A. R., J. H. Eckfeldt, et al. (1994). "Relation of Carotid-Artery Wall Thickness to Diabetes-Mellitus, Fasting Glucose and Insulin, Body-Size, and Physical-Activity." *Stroke* 25(1): 66-73.

Forsberg, F., Z. Morvay, et al. (2000). "Shear Rate Estimation Using a Clinical Ultrasound Scanner." *Journal of Ultrasound in Medicine* 19(5): 323-327.

Fredenberg, S., M. Wahlgren, et al. (2011). "The Mechanisms of Drug Release in Poly(lactic-co-glycolic acid)-Based Drug Delivery Systems-A Review." *International Journal of Pharmaceutics* 415(1-2): 34-52.

Fung, Y. C. (1993). "Biomechanics: Mechanical Properties of Living Tissues, 2nd Edition." *Springer*.

Gambillara, V., G. Montorzi, et al. (2005). "Arterial Wall Response to Ex Vivo Exposure to Oscillatory Shear Stress." *Journal of Vascular Research* 42(6): 535-544.

Garcia-Canadilla, P., P. A. Rudenick, et al. (2014). "A Computational Model of the Fetal Circulation to Quantify Blood Redistribution in Intrauterine Growth Restriction." Journal of Computational Biology 10(6): 14.

George, B. S., Meyer, R.K., Stertzer, S.H. (1986). "Balloon Angioplasty of Coronary Bifurcation Lesions: The Kissing Balloon Technique." *Catheter Cardiovascular Diagn*. 12: 124-138.

Giannoglou, G. D., J. V. Soulis, et al. (2005). "Wall Pressure Gradient in Normal Left Coronary Artery Tree." *Medical Engineering & Physics* 27(6): 455-464.

Gijsen, F. J. H., D. E. M. Palmen, et al. (1996). "Analysis of The Axial Flow Field in Stenosed Carotid Artery Bifurcation Models - LDA Experiments." *Journal of Biomechanics* 29(11): 1483-1489.

Giulioni, M. and M. Ursino (2003). "Head Injury and Autoregulation." *Journal of Neurosurgery* 99(2): 437-438.

Glagov, S., C. Zarins, et al. (1988). "Hemodynamics And Atherosclerosis - Insights And Perspectives Gained From Studies Of Human Arteries." *Archives of Pathology & Laboratory Medicine* 112(10): 1018-1031.

Gorelick, P. B. (1995). "Stroke Prevention." *Archives of Neurology [Review]* 52: pp. 347-355.

Guo, Z. Y. and A. Fenster (1996). "Three-Dimensional Power Doppler Imaging: A Phantom Study to Quantify Vessel Stenosis." *Ultrasound in Medicine and Biology* 22(8): 1059-1069.

Haidekker, M. A., C. R. White, et al. (2001). "Analysis of Temporal Shear Stress Gradients During The Onset Phase of Flow Over a Backward-facing Step." *Journal of Biomechanical Engineering-Transactions of the ASME* 123(5): 455-463.

Helde, T. a. S., E. (2002). "Modeling of Cardiovascular Response to Orthostatic Stress." *Journal of Applied Physiology* 92: 1239-1254.

Hewlin, Jr., R.L., and Kizito, J.P. (2011). "Evaluation of the Effect of Simplified and Patient-Specific Arterial Geometry On Hemodynamic Flow In Stenosed Carotid Bifurcation Arteries." *ASME Early Career Technical Journal* 10: 39-44.

Hill, T. L. (1983). "2 Elementary Models for the Regulation of Skeletal-Muscle Contraction by Calcium." *Biophysical Journal* 44(3): 383-396.

Hoskins, P. R. (1997). "Peak Velocity Estimation in Arterial Stenosis Models Using Color Vector Doppler." *Ultrasound in Medicine and Biology* 23(6): 889-897.

Hoskins, P. R. (2008). "Simulation and Validation of Arterial Ultrasound Imaging and Blood Flow." *Ultrasound in Medicine and Biology* 34(5): 693-717.

Hoskins, P. R. and W. N. McDicken (1991). "Velocity Estimation Using Duplex Scanners." *Ultrasound in Medicine and Biology* 17(2): 195-198.

Hossainy, S. and S. Prabhu (2008). "A Mathematical Model for Predicting Drug Release From a Biodurable Drug-Eluting Stent Coating." *Journal of Biomedical Materials Research Part A* 87A(2): 487-493.

Joshi, A. and K. J. Himmelstein (1991). "Dynamics of Controlled Release From Bioerodible Matrices." *Journal of Controlled Release* 15(2): 95-104.

Karvouni, E., C. Di Mario, et al. (2001). "Directional Atherectomy Prior to Stenting in Bifurcation Lesions: A Matched Comparison Study with Stenting Alone." *Catheterization and Cardiovascular Interventions* 53(1): 12-20.

Kastrati, A., J. Mehilli, et al. (2001). "Restenosis After Coronary Placement of Various Stent Types." *American Journal of Cardiology* 87(1): 34-39.

Korakianitis, T. and Y. Shi (2006). "A Concentrated Parameter Model for the Human Cardiovascular System Including Heart Valve Dynamics and Atrioventricular Interaction." *Medical Engineering & Physics* 28(7): 613-628.

Ku, D. N. and D. P. Giddens (1987). "Laser Doppler Anemometer Measurements Of Pulsatile Flow In a Model Carotid Bifurcation." *Journal of Biomechanics* 20(4): 407-421.

Ku, D. N., D. P. Giddens, et al. (1985). "Pulsatile Flow and Atherosclerosis in the Human Carotid Bifurcation - Positive Correlation Between Plaque Location And Low And Oscillating Shear-Stress." *Arteriosclerosis* 5(3): 293-302.

Latib, A., A. Colombo, et al. (2009). "Bifurcation Stenting: Current Strategies and New Devices." *Heart* 95(6): 495-504.

Law, Y. F., K. W. Johnston, et al. (1989). "On The Design and Evaluation of a Steady Flow Model For Doppler Ultrasound Studies." *Ultrasound in Medicine and Biology* 15(5): 505-516.

Lee, P. I. (1980). "Diffusional Release of a Solute from a Polymeric Matrix - Approximate Analytical Solutions." *Abstracts of Papers of the American Chemical Society* 179(MAR): 35-INDE.

Lefevre, T., Y. Louvard, et al. (2000). "Stenting of Bifurcation Lesions: Classification, Treatments, and Results." *Catheterization and Cardiovascular Interventions* 49(3): 274-283.

Lei, M., D. P. Giddens, et al. (2001). "Pulsatile Flow in an End-to-side Vascular Graft Model: Comparison of Computations With Experimental data." *Journal of Biomechanical Engineering-Transactions of the ASME* 123(1): 80-87.

Lewis, G. (2008). "Materials, Fluid Dynamics, and Solid Mechanics Aspects of Coronary Artery Stents: A State-of-the-art Review." *Journal of Biomedical Materials Research Part B-Applied Biomaterial*s 86B(2): 569-590.

Livshitz, L. and Y. Rudy (2009). "Uniqueness and Stability of Action Potential Models During Rest, Pacing, and Conduction Using Problem-Solving Environment." *Biophysical Journal* 97(5): 1265-1276.

Lu, K., J. W. Clark, et al. (2001). "A Human Cardiopulmonary System Model Applied to the Analysis of The Valsalva Maneuver." *American Journal of Physiology-Heart and Circulatory Physiology* 281(6): H2661-H2679.

Luo, C. H. and Y. Rudy (1994). "A Dynamic-Model of the Cardiac Ventricular Action-Potential Part 1. Simulations of Ionic Currents and Concentration Changes." *Circulation Research* 74(6): 1071-1096.

M. Horner., S. I., V.Dheuva et al. (2010). "A Two-Species Drug Delivery Model is Required to Predict Deposition From Drug-Eluting Stents." *Journal of Cardiovascular Engineering Technology* 1(3): 225-234.

Malek, A. M., Alper, S.L., Izumo, S., (1999). "Hemodynamic Shear Stress and Its Role In Atherosclerosis." *Journal of the American Medical Association* 282: 2035-2042.

McDonald, D. A. (1974). "Blood Flow in Arteries, 2nd Ed." *Edward Arnold.*

Melbin, J., R. Gopalakrishnan, et al. (1982). "Construction and Characterization of Branched, Elastic, Transparent Vessel Models." *American Journal of Physiology* 242(1): H122-H126.

Menasche, P. (2010). "Cell Therapy For Peripheral Arterial Disease." *Current Opinion in Molecular Therapeutic*s 12(5): 538-545.

Motomiya, M. and T. Karino (1984). "Flow Patterns in The Human Carotid-Artery Bifurcation." *Stroke* 15(1): 50-56.

Nagel, T., N. Resnick, et al. (1999). "Vascular Endothelial Cells Respond To Spatial Gradients in Fluid Shear Stress By Enhanced Activation of Transcription Factors." *Arteriosclerosis Thrombosis and Vascular Biology* 19(8): 1825-1834.

Natarajan, S. and M. R. Mokhtarzadeh-Dehghan (2000). "A Numerical and Experimental Study of Periodic Flow in a Model of a Corrugated Vessel With Application to Stented Arteries." *Medical Engineering & Physics* 22(8): 555-566.

Oshinski, J. N., D. N. Ku, et al. (1995). "Determination of Wall Shear Stress in the Aorta with the Use of MR Phase Velocity Mapping." *JMRI-Journal of Magnetic Resonance Imaging* 5(6): 640-647.

Palmen, D. E. M., F. N. Vandevosse, et al. (1994). "Analysis of the Flow in Stenosed Carotid-Artery Bifurcation Models - Hydrogen-Bubble Visualization." *Journal of Biomechanics* 27(5): 581-590.

Panerai, R. B. (1980). "A Model of Cardiac-Muscle Mechanics and Energetics." *Journal of Biomechanics* 13(11): 929-940.

Patterson, M. S. and F. S. Foster (1983). "The Improvement and Quantitative Assessment of B-Mode Images Produces By An Annular Array Cone Hybrid." *Ultrasonic Imaging* 5(3): 195-213.

Pedersen, E. M., S. Oyre, et al. (1999). "Distribution of Early Atherosclerotic Lesions in the Human Abdominal Aorta Correlates With Wall Shear Stresses Measured In Vivo." European *Journal of Vascular and Endovascular Surgery* 18(4): 328-333.

Pedley, T. J. (2000). "Blood Flow in Arteries and Veins. In Perspectives in Fluid Dynamics: A Collective Introduction to Current Research (ed. G. K. Batchelor, H.K. Moffatt & M.G. Worster)." *Cambridge University Press*: pp. 105-158.

Pennati, G., M. Bellotti, et al. (1997). "Mathematical Modeling of the Human Foetal Cardiovascular System Based on Doppler Ultrasound Data." *Medical Engineering & Physics* 19(4): 327-335.

Picot, P. A. and P. M. Embree (1994). "Quantitative Volume Flow Estimation Using Velocity Profiles." *IEEE Transactions on Ultrasonics Ferroelectrics and Frequency Control* 41(3): 340-345.

Picot, P. A., M. Fruitman, et al. (1995). "Rapid Volume Flow-Rate Estimation Using Transverse Color Doppler Imaging." *Ultrasound in Medicine and Biology* 21(9): 1199-1209.

Poepping, T. L., H. N. Nikolov, et al. (2002). "An In Vitro System for Doppler Ultrasound Flow Studies in the Stenosed Carotid Artery Bifurcation." *Ultrasound in Medicine and Biology* 28(4): 495-506.

Polak, J. F., D. H. Oleary, et al. (1990). "Pulsed and Color Doppler Analysis of Normal Carotid Bifurcation Flow Dynamics Using An Invitro Model." *Angiology* 41(3): 241-247.

Pontrelli G, Rossoni E: "Numerical Modeling of the Pressure Wave Propagation in the Arterial Flow." *International Journal for Numerical Methods in Fluids 2003*, 43:651-671.

Prabhu, S. and S. Hossainy (2007). "Modeling of Degradation and Drug Release From a Biodegradable Stent Coating." *Journal of Biomedical Materials Research Part A* 80A(3): 732-741.

Pythoud, F., N. Stergiopulos, et al. (1994). "Modeling of the Wave Transmission Properties of Large Arteries Using Non-Linear Elastic Tubes." *Journal of Biomechanics* 27(11): 1379-1381.

Qiu, X. N., Z. M. Fei, et al. (2013). "Influence of High-Porosity Mesh Stent on Hemodynamics of Intracranial Aneurysm: A Computational Study." *Journal of Hydrodynamics* 25(6): 848-855.

Qiu, Y. C. and J. M. Tarbell (2000). "Numerical Simulation of Pulsatile Flow In a Compliant Curved Tube Model of a Coronary Artery." *Journal of Biomechanical Engineering-Transactions of the ASME* 122(1): 77-85.

Ramnarine, K. V., T. Anderson, et al. (2001). "Construction and Geometric Stability of Physiological Flow Rate Wall-less Stenosis Phantoms." *Ultrasound in Medicine and Biology* 27(2): 245-250.

Rhodes, S. S., K. M. Ropella, et al. (2003). "Cross-Bridge Kinetics Modeled From Myoplasmic Ca2+ and LV Pressure at 17 degrees C and after 37 degrees C and 17 degrees C Ischemia." *American Journal of Physiology-Heart and Circulatory Physiology* 284(4): H1217-H1229.

Rickey, D. W., P. A. Picot, et al. (1995). "A Wall-less Vessel Phantom For Doppler Ultrasound Studies." *Ultrasound in Medicine and Biology* 21(9): 1163-1176.

Ricotta, J., J. Pagan, et al. (2008). "Cardiovascular Disease Management: The Need For Better Diagnostics." *Medical & Biological Engineering & Computing* 46(11): 1059-1068.

Rideout, V. C. (1991). ""Mathematical and Computer Modeling of Physiological Systems." New York: *Prentice Hall.*

Riley, W. A., R. W. Barnes, et al. (1992). "Ultrasonic Measurement of the Elastic-Modulus of The Common Carotid-Artery - The Atherosclerosis Risk In Communities (ARIC) Study." *Stroke* 23(7): 952-956.

Rindt, C. C. M. and A. A. Von Steenhoven (1996). "Unsteady Flow in a Rigid 3-D Model of the Carotid Artery Bifurcation." *Journal of Biomechanical Engineering-Transactions of the ASME* 118(1): 90-96.

Roach, M. R. and A. C. Burton (1957). "The Reason for the Shape of The Distensibility Curves of Arteries." *Canadian Journal of Biochemistry and Physiology* 35(8): 681-690.

Rothstein, S. N., W. J. Federspiel, et al. (2009). "A Unified Mathematical Model for the Prediction of Controlled Release from Surface and Bulk Eroding Polymer Matrices." *Journal of Biomaterials* 30(8): 1657-1664.

Rupnic, M. a. R., F. (2002). "Simulation of Steady State and Transient Phenomena by Using the Equivalent Electronic Circuit." *Journal of Computer Methods and Programs in Biomedics* (67): 1-12.

Ryan, L. K. and F. S. Foster (1997). "Tissue Equivalent Vessel Phantoms for Intravascular Ultrasound." *Ultrasound in Medicine and Biology* 23(2): 261-273.

Samuel, K. C. (1956). "Atherosclerosis and Occlusion of the Internal Carotid Artery." *Journal of Pathology and Bacteriology* 71(2): 391-&.

Secomski, W., A. Nowicki, et al. (2003). "Noninvasive In Vivo Measurements of Hematocrit." *Journal of Ultrasound in Medicine* 22(4): 375-384.

Selvarasu, N. K. C., D. K. Tafti, et al. (2011). "Hydrodynamic Effects of Compliance Mismatch in Stented Arteries." *Journal of Biomechanical Engineering-Transactions of the ASME* 133(2).

Shaw, B. H., T. M. Loughin, et al. (2014). "The Effect of Orthostatic Stress Type on Cardiovascular Control." *Blood Pressure Monitoring* 19(6): 327-338.

Sheiban, I., R. Albiero, et al. (2000). "Immediate and Long-term Results of "T" Stenting For Bifurcation Coronary Lesions." *American Journal of Cardiology* 85(9): 1141-+.

Sherwin S.J., Formaggia L, Peir , Franke V: "Computational Modeling of 1D Blood Flow with Variable Mechanical Properties and Application to the Simulation of Wave Propagation in the Human Arterial System." *International Journal for Numerical Methods in Fluids 2003*, 43:673-700.

Shi, Y., T. Korakianitis, et al. (2007). "Numerical Simulation of Cardiovascular Dynamics with Different Types of VAD assistance." *Journal of Biomechanics* 40(13): 2919-2933.

Shi, Y. B., P. Lawford, et al. (2011). "Review of Zero-D and 1-D Models of Blood Flow in the Cardiovascular System." *Biomedical Engineering Online* 10: 38.

Shuib, A., P. Hoskins, et al. (2011). "Experimental Investigation of Particle Distribution in a Flow Through a Stenosed Artery." *Journal of Mechanical Science and Technology* 25(2): 357-364.

Siauw, W. L., E. Y. K. Ng, et al. (2000). "Unsteady Stenosis Flow Prediction: A Comparative Study of Non-Newtonian Models with Operator Splitting Scheme." *Medical Engineering & Physics* 22(4): 265-277.

Siebes, M. and Y. Ventikos (2010). "The Role of Biofluid Mechanics in the Assessment of Clinical and Pathological Observations." *Annals of Biomedical Engineering* 38(3): 1216-1224.

Siepmann, J. and A. Gopferich (2001). "Mathematical Modeling of Bioerodible, Polymeric Drug Delivery Systems." *Advanced Drug Delivery Reviews* 48(2-3): 229-247.

Siepmann, J. and F. Siepmann (2008). "Mathematical Modeling of Drug Delivery." International *Journal of Pharmaceutics* 364(2): 328-343.

Slager, C. J., J. K. Wentzel, et al. (2005). "The Role of Shear Stress in the Generation of Rupture-Prone Vulnerable Plaques." *Nature Clinical Practice Cardiovascular Medicine* 2(8): 401-407.

Smith, R. F., B. K. Rutt, et al. (1996). "Geometric Characterization of Stenosed Human Carotid Arteries." *Academic Radiology* 3(11): 898-911.

Soares, J. S. and P. Zunino (2010). "A Mixture Model for Water Uptake, Degradation, Erosion and Drug Release from Polydisperse Polymeric Networks." *Biomaterials* 31(11): 3032-3042.

Solberg, L. A. and D. A. Eggen (1971). "Localization and Sequences of Development of Atherosclerotic Lesions In Carotid and Vertebral Arteries." *Circulation* 43(5): 711-&.

Soulis, J. V., G. D. Giannoglou, et al. (2007). "Flow Parameters in Normal Left Coronary Artery Tree. Implication to Atherogenesis." *Computers in Biology and Medicine* 37(5): 628-636.

Steel, R., K. V. Ramnarine, et al. (2003). "Angle-Independent Estimation of Maximum Velocity Through Stenoses Using Vector Doppler ultrasound." *Ultrasound in Medicine and Biology* 29(4): 575-584.

Steigen, T. K., M. Maeng, et al. (2006). "Randomized Study on Simple Versus Complex Stenting of Coronary Artery Bifurcation Lesions - The Nordic Bifurcation study." *Circulation* 114(18): 1955-1961.

Teirlinck, C., R. A. Bezemer, et al. (1998). "Development of an Example Flow Test Object and Comparison of Five of These Test Objects, Constructed in Various laboratories." *Journal o Ultrasonics* 36(1-5): 653-660.

Thompson, R. S., G. K. Aldis, et al. (1990). "Doppler Ultrasound Spectral Power-Density Distribution - Measurement Artifacts in Steady Flow." *Medical & Biological Engineering & Computing* 28(1): 60-66.

Thorne, M. L., T. L. Poepping, et al. (2008). "Use of an Ultrasound Blood-Mimicking Fluid for Doppler Investigations of Turbulence In-vitro." *Ultrasound in Medicine and Biology* 34(7): 1163-1173.

Thuesen, L., H. Kelbaek, et al. (2006). "Comparison of Sirolimus-Eluting and Bare Metal Stents in Coronary Bifurcation L0esions: Subgroup Analysis of the Stenting Coronary Arteries in Non-Stress/Benestent Disease Trial (Scandstent)." *American Heart Journal* 152(6): 1140-1145.

Topol, E. J. (1998). "Coronary-artery stents - Gauging, Gorging, and Gouging." *New England Journal of Medicine* 339(23): 1702-1704.

Topol, E. J. and P. W. Serruys (1998). "Frontiers in Interventional Cardiology." *Circulation* 98(17): 1802-1820.

Ubbink, S. W. J., P. H. M. Bovendeerd, et al. (2006). "Towards Model-Based Analysis of Cardiac MR Tagging Data: Relation Between Left Ventricular Shear Strain and Myofiber Orientation." *Medical Image Analysis* 10(4): 632-641.

Ursino, M. and E. Magosso (2000). "Acute Cardiovascular Response to Isocapnic Hypoxia. II. Model Validation." *American Journal of Physiology-Heart and Circulatory Physiology* 279(1): H166-H175.

Van Wyk, S., L. P. Wittberg, et al. (2014). "Atherosclerotic Indicators for Blood-like fluids in 90-Degree Arterial-like Bifurcations." *Computers in Biology and Medicine* 50: 56-69.

Voitl, P., Vollkron et al. (2009). "Coronary Hemodynamics and Myocardial Oxygen Consumption During Suppory with Rotary Blood Pumps." *Journal of Artificial Organs* 33(1): 77-80.

Wagenknecht, L. E., R. Dagostino, et al. (1997). "Duration of Diabetes and Carotid wall Thickness - *The Insulin Resistance Atherosclerosis Study (IRAS)." Stroke* 28(5): 999-1005.

Wessely, R. (2010). "New Drug-Eluting Stent Concepts." *Nature Reviews Cardiology* 7(4): 194-203.

White, C. R., M. Haidekker, et al. (2001). "Temporal Gradients in Shear, But Not Spatial Gradients, *Stimulate Endothelial Cell Proliferation.*" Circulation 103(20): 2508-2513.

X. Zhu, R. B. (2014). "Modeling and Analysis of Drug-Eluting Stents with Biodegradable PLGA Coating: Consequences on Intravascular Drug Delivery." *ASME Journal of Biomechanical Engineering* 136(11): 1-10.

Xiang, J., A. H. Siddiqui, et al. (2014). "The Effect of Inlet Waveforms on Computational Hemodynamics of Patient-Specific Intracranial Aneurysms." *Journal of Biomechanics* 47(16): 3882-3890.

Xiang, J., V. M. Tutino, et al. (2014). "CFD: Computational Fluid Dynamics or Confounding Factor Dissemination? The Role of Hemodynamics in Intracranial Aneurysm Rupture Risk Assessment." *American Journal of Neuroradiology* 35(10): 1849-1857.

Yamashita, T., T. Nishida, et al. (2000). "Bifurcation Lesions: Two Stents Versus One Stent - Immediate and Follow-up Results." *Journal of the American College of Cardiology* 35(5): 1145-1151.

Yang, C. M. and H. A. Burt (2006). "Drug-Eluting Stents: Factors Governing Local Pharmacokinetics." *Advanced Drug Delivery Reviews* 58(3): 402-411.

Young, A. A. and J. L. Prince (2013). "Cardiovascular Magnetic Resonance: Deeper Insights Through Bioengineering." *Annual Review of Biomedical Engineering*, Vol 15 15: 433-461.

Zacek, M. a. K., E. (1996). ""Numerical Simulation of the Blood flow in the Human Cardiovascular System." *Journal of Biomechanics* 32: 13-20.

Zarins, C. K., D. P. Giddens, et al. (1983). "Carotid Bifurcation Atherosclerosis Quantitative Correlation of Plaque Localization with Flow Velocity Profiles and Wall Shear-Stress." *Circulation Research* 53(4): 502-514.

Zervides, C., A. J. Narracott, et al. (2008). "The Role of Venous Valves in Pressure Shielding." *Biomedical Engineering Online* 7: 10.

Zhang, Y., D. Agnoletti, et al. (2014). "Carotid-Femoral Pulse Wave Velocity in the Elderly." *Journal of Hypertension* 32(8): 1572-1576.

Zhao, S. Z., B. Ariff, et al. (2002). "Inter-individual Variations in Wall Shear Stress and Mechanical Stress Distributions at the Carotid Artery Bifurcation of Healthy Humans." *Journal of Biomechanics* 35(10): 1367-1377.

Zhu, X. X., D. W. Pack, et al. (2014). "Modeling Intravascular Delivery from Drug-Eluting Stents with Biodurable Coating: Investigation of Anisotropic Vascular Drug Diffusivity and Arterial Drug Distribution." *Computer Methods in Biomechanics and Biomedical Engineering* 17(3): 187-198.